Motion of Particles in Complex Flows

Thesis

Motion of particles in complex flows

Vladyslav Bezuglyy

Department of Mathematics and Statistics

The Open University

A Thesis submitted for the degree of Doctor of Philosophy

at the Open University

Discipline: Mathematics

September, 2009

Submission date: 25 August 2009

Date of award: 23 October 2009

ProQuest LLC.
789 East Eisenhower Parkway
P.O. Box 1346
Ann Arbor, MI 48106 – 1346

MOTION OF PARTICLES IN COMPLEX FLOWS

Vladyslav Bezuglyy
Department of Mathematics and Statistics
The Open University

A Thesis submitted for the degree of Doctor of Philosophy

September, 2009

ABSTRACT

This thesis covers various aspects of motion of small rigid particles in complex flows. It is in two parts.

Part I is concerned with motion of small spherical particles.

We study extensions of two classical models for diffusion of a particle driven by random forces, namely the Ornstein-Uhlenbeck process and Chandrasekhar-Rosenbluth model. We show that both models exhibit similar scaling of the diffusion matrix, leading to the same short-time asymptotic dynamics characterized by anomalous diffusion of the momentum and ballistic diffusion of the displacement.

We discuss a generalization of the Kramers model describing an overdamped particle in an external potential driven by random forces. We analyze the stationary probability density of the position in the limit when the external forcing is strong and show that the density yields a non-zero probability flux for the motion in a periodic potential with a broken reflection symmetry.

We explain quantitatively an abrupt increase of the collision rate of inertial particles suspended in a flow, as the intensity of turbulence $\mathcal{I}$ passes a threshold. We argue that the collision rate exhibits an activated behaviour containing a factor $\exp(-\text{const}/\mathcal{I})$ due to the formation of fold caustics in their velocity field.

Part II is concerned with patterns formed by small non-spherical, axisymmetric particles advected in a flow. Numerical simulations suggest that the direction field of the particles exhibits topological singularities of the same type as those seen in fingerprints. An exact solution of the equation of motion indicates that the direction field is non-singular, but we give a theoretical explanation arguing that the singularities are approached in an asymptotic sense.

We introduce the order parameter vector characterizing the alignment of particles. We show that the order parameter field also exhibits singularities and describe their normal forms. The order parameter is related to the reflection of light by a rheoscopic fluid illuminated by three coloured light sources. We report on the results of a simple experiment supporting our theoretical findings.

Acknowledgements

I would like to thank my supervisor, Prof. M. Wilkinson, for his advice, support, and patience throughout my studies. I would also like to thank Prof. B. Mehlig from University of Gothenburg for his contribution to our joint projects and inviting me to Sweden on a number of occasions.

I am very grateful to my family and friends for their support and understanding.

The financial support from the Open University is gratefully acknowledged.

Contents

List of Figures

Chapter 1

Introduction

In this thesis we address a number of problems which concern motion of small objects suspended in fluid flows. The number of possible realizations of such systems in nature is truly enormous. Some of them are shown in Fig. 1.1, including clouds consisting of tiny water droplets floating in the air [1], plankton organisms, which are incapable of resisting oceanic flows [2], interstellar dust in a gas around a growing star [3], and solid dust produced during volcanic eruptions [4]. These few examples indicate that there is a significant interest in analyzing such systems both qualitatively and quantitatively. In all these examples, suspended objects (henceforth, particles) have a variety of properties such as size, shape, density, etc. It is rather difficult to take into account all possible characteristics of particles of complex shape and structure, and in this thesis we study simplified models of small rigid particles which are either spherical or else non-spherical but axisymmetric. It is equally hard to study both analytically and numerically motion of particles suspended in viscous flows satisfying the Navier-Stokes equation, especially if the flow is in a turbulent state, which is the typical case for cumulus clouds [1] and interstellar gas in the accretion disk around a growing stars [5]. Turbulent flows appear chaotic and random, so that instead of trying to solve the Navier-Stokes equation, we study motion of particles in 'synthetic' velocity fields, which are, in fact, smooth random fields varying in time and space with prescribed statistical properties. In this sense, we term them 'complex', as opposed to 'simple' flows, such as those which are steady or uniform. Although such synthetic flow

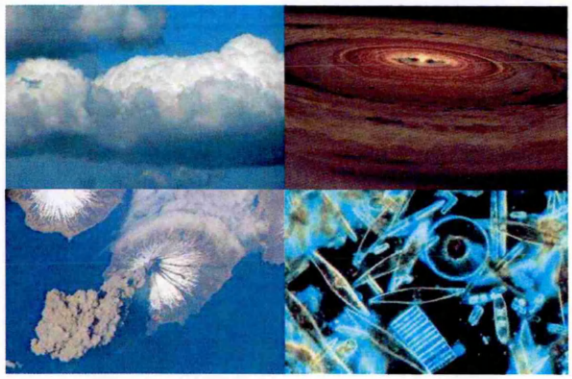

Figure 1.1: Particles in complex flows are ubiquitous in nature. From left to right, top to bottom: in cumulus clouds, droplets of moisture collide and aggregate to form rain droplets (image by the author of the thesis); an artist's representation of the accretion disk around a young star, where the grain dust particles are suspended in a turbulent gas (image credit to NASA/JPL-Caltech); eruption of Cleveland Volcano (Aleutian Islands, Alaska) producing a large amount of solid dust and ash (image credit to NASA); marine diatoms (major group of phytoplankton) under microscope (image credit to National Oceanic and Atmospheric Administration).

fields are not actual solutions of the Navier-Stokers equation, they can still provide a sufficient insight into many physical problems discussed in this thesis.

Motion of particles in complex flows has many different aspects and features. Even without specifying necessary equations, some of them can be understood intuitively using simple examples. If the particles are very light, we expect that their velocity is approximately equal to the velocity of the carrier flow at a given point in space. In this case the particles are said to be advected by the flow. As the particles become heavier, they gain inertia and start to detach from the flow. Naively, it is expected that in an incompressible fluid, with no sinks and sources, the particles should be mixed by the flow, so that their spatial distribution tends to be uniform. This is indeed what happens when the particles are simply advected. In the case when the inertia of the particles is significant, it has been noted that the particles may cluster. In Fig. 1.2 we show a snapshot from the numerical simulation of inertial particles suspended in a smooth random flow. Surprisingly, the spatial density of particles, which was initially uniform, becomes significantly non-uniform at later times. Deutsch [6] was apparently first to study 'coalescence' of the particles trajectories using a simple one-dimensional model. Later, it was suggested by Maxey [7] that inertial particles cluster because they are centrifuged away from vortices into the regions of low vorticity and high strain.

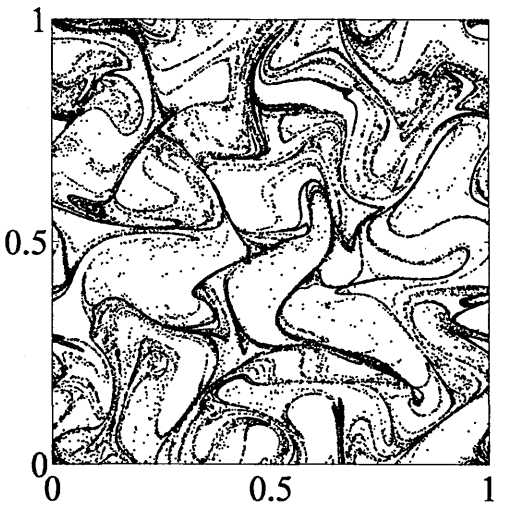

Figure 1.2: A snapshot from the numerical simulation showing 10^5 particles with inertia in an incompressible complex flow in a plane (equations of motion are specified in chapter 2) showing visibly non-uniform patterns. The patterns may appear as fractals with the dimension smaller than that of space. The particles were initially uniformly distributed.

Alternatively, Sommerer and Ott [8] studied patterns formed by particles floating on a surface of a randomly stirred fluid as fractals. They discussed how the fractal dimension of these patterns may be obtained in terms of the Lyapunov exponents of the particle trajectories. Analytical calculations of these Lyapunov exponents and the fractal dimension were done by Wilkinson, Mehlig and co-workers in the series of works with results reviewed in [9]. These analytical results are in a good agreement with those obtained by Bec *et al.* [10] from direct numerical simulations of particles suspended in a flow satisfying the Navier-Stokes equation.

Another consequence of the detachment of the particles from the flow due to their inertia is the fact that the velocity field of the particles can become multivalued, i.e. two particles that are very close to each other can have significantly different velocities. This is not possible when the particles are advected, because the carrier flow is itself single-valued. Such a multivalued velocity field of the particles is linked with the formation of 'caustics' - singular structures, where the density of particles diverges [11, 12]. Fig. 1.3 illustrates schematically how the caustics are formed in the one-dimensional model. Initially, at time $t = t_0$, the particles are assumed to move with the velocity of the flow, so that the function $v(x)$ describing the dependence

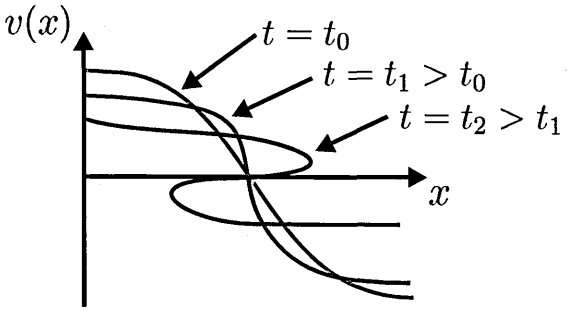

Figure 1.3: Schematic illustration showing formation of caustics. The velocity of inertial particles as a function of their position, $v(x)$, is assumed to be single-valued at $t = t_0$. Faster particles overtake slower-moving particles, and at $t = t_1 > t_0$ the projection of $v(x)$ is almost perpendicular to x-axis. As the particles keep moving, at time $t = t_2 > t_1$ two folds are formed, where $v(x)$ is multivalued.

of the velocity of the particles on their position is single-valued. The particles with larger velocities will overtake slower-moving particles, and at some instant of time $t = t_1 > t_0$, the projection of $v(x)$ on x-axis will become almost perpendicular to this axis. If the density of the particles is smooth along the x-axis, it is proportional to the derivative dv/dx, which diverges when the projection of $v(x)$ becomes perpendicular. As the particles move further, two folds are formed where $v(x)$ is multivalued. The term 'caustics' is used due to the apparent similarity of patterns of the suspended particles (shown in Fig. 1.4) with patterns of optical caustics seen, for instance, on the bottom of a swimming pool on a sunny day [13].

Clustering and caustics are just a few of many different aspects of motion of particles which has been studied intensively recently. There are many other important questions one could ask regarding particles suspended in complex flows. What is the frequency at which the particles collide and how does it depend on their properties and the properties of the flow? What does an orientation field of anisotropic particles suspended in a fluid look like, are there any particular structures there? What is the characteristic behaviour of an ensemble of particles suspended in complex flows? Is it diffusive? And if so, what is the law of diffusion? Some of these questions are answered in this thesis.

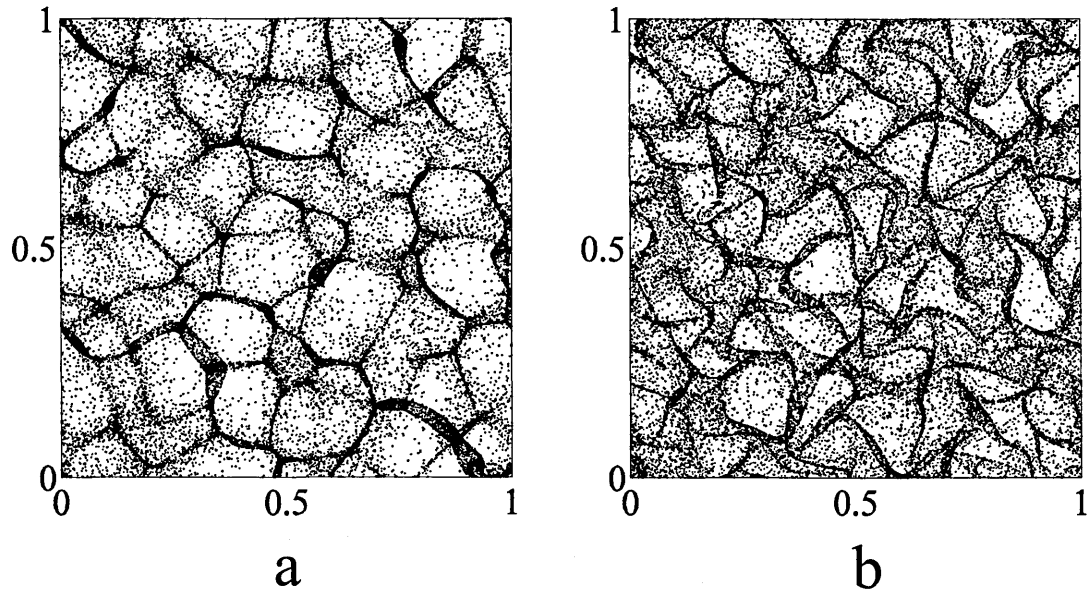

Figure 1.4: Two snapshots from the numerical simulation showing 10^5 inertial particles in compressible (**a**) and incompressible (**b**) complex flows in a plane (equations of motion are specified in chapter 2) illustrating the network of caustics. The caustics are less pronounced but still visible in the case of motion in the incompressible flow.

1.1 Outline of the thesis

The thesis is organized as follows. After this introductory chapter we review basic principles, methods, and models used in analyzing motion of particles in complex flows. We first present basic equations of fluid mechanics and then briefly discuss properties of turbulent flows based on the Richardson's idea of the energy cascade [14] and Kolmogorov's theory of turbulence [15]. Next, we discuss a number of existing numerical models which can be employed for generating complex flow fields. We introduce equations of motion for both spherical and non-spherical particles based on the so-called Stokes approximation, in which the motion of particles is dominated by viscous forces (this is a justifiable assumption for sufficiently small particles). We also relate motion of particles in fluids to models of diffusion. Turbulent flows appear random, so that their action on suspended particles can be seen as a sequence of random impulses, suggesting a close relation to the model of random walks and Brownian motion. We briefly discuss methods which can be employed for analyzing diffusion of particles driven by random forces. After reviewing basic principles, we consider

the problems in two parts dedicated separately to the study of motion of spherical and non-spherical, axisymmetric particles. These two parts consist of several chapters which consider different individual aspects of motion of particles. In the last chapter we summarize our work and propose a number of questions for further research.

Below, we briefly discuss the content of the chapters in separate sections, describing the problems and reporting our main original results.

1.1.1 Universal anomalous diffusion of weakly damped particles

The third chapter addresses the problem of diffusion of a heavy particle driven by random forces. We consider two diffusion processes. First, we study the so-called generalized Ornstein-Uhlenbeck process [16, 17] in two and three spatial dimensions. The problem is an extension of a classical diffusion process [18], in which the particle is weakly damped and driven by a time-dependent force. Our generalization includes the force $\boldsymbol{f}(\boldsymbol{r}, t)$ which depends on the position of the particle $\boldsymbol{r}$, as well as time t. The dynamics of the momentum of the particle $\boldsymbol{p}$ is given by the following equation of motion:

$$\dot{\boldsymbol{p}} = -\gamma \boldsymbol{p} + \boldsymbol{f}(\boldsymbol{r}, t), \tag{1.1}$$

where γ is the damping rate (dots denote derivatives with respect to time). The generalized process is characterized by weak damping, as well as strong forcing, so that the particle can accelerate to very large velocities (compared to some characteristic velocity scale). In this case, during one correlation time of the force the particle may travel over many correlation lengths. This regime, apparently, cannot be realized in fluids. It may, however, be realized in other physical problems, such as motion of charged particles in a random electro-magnetic field [19, 20]. In [16, 17] the problem was analyzed in details for the motion in one spatial dimension, but here we concentrate on the motion in two and three spatial dimensions. We show that the model exhibits a number of interesting features, such as a non-Maxwellian momentum distribution in the steady state and anomalous diffusion of the momentum. We obtain precise

asymptotic formulae for the growth of the second moment of the magnitude of the momentum p and displacement x of the particle. We show that the second moment of p at short times grows anomalously as $\langle p^2 \rangle \sim t^{2/5}$, and the displacement grows ballistically, i.e. $\langle x^2 \rangle \sim t^2$ (angular brackets denote average over many realizations of the stochastic process). We discuss how the generalized Ornstein-Uhlenbeck process can be related to another model of diffusion, the Chandrasekhar-Rosenbluth model [21, 22], in which a test particle interacts with a gas of point masses via a pair potential. This model was originally studied by Chandrasekhar in the context of motion of stars in a galaxy, where the interaction is gravitational. Chandrasekhar showed that the test particle experiences 'dynamical friction' - a gradual decrease of the velocity in the direction of motion. Later, Rosenbluth obtained the diffusion coefficients and the Fokker-Planck equation for this model. In the thesis we extend this model by replacing the gravitational interaction with a non-singular short-range interaction of some rather arbitrary form. We derive diffusion coefficients for this model precisely in terms of the macroscopic parameters of the model. Surprisingly, the diffusion matrix has the same form as in the generalized Ornstein-Uhlenbeck process. This leads to the same short-time asymptotic dynamics characterized by anomalous diffusion with the same universal exponent in both models.

1.1.2 Generalized Kramers model

In the fourth chapter we continue discussing diffusion of particles driven by random forces. In this case we study overdamped dynamics of a particle subjected to an additional deterministic potential force (in one spatial dimension). This model is an extension of the so-called Kramers model [23], in which random fluctuations are usually modelled as a rapidly fluctuating time-dependent force. We generalize this model by considering the random force which depends upon the position of the particle, as well as time. The equation of motion describing the dynamics of the position of the

particle $x(t)$ in one spatial dimension reads

$$\kappa\dot{x} = -\frac{dU(x)}{dx} + f(x,t), \tag{1.2}$$

where $f(x,t)$ is the random force, $U(x)$ is the potential, and κ is the friction coefficient. The original Kramers model has a number of particularly useful and important applications. The first example concerns modelling the state of a chemical reaction, where the position of the particle plays a role of the reaction coordinate, the random force describes thermal fluctuations, and the external potential represents the potential energy associated with the reaction. The other model is the well-known ratchet-and-pawl mechanism in a thermal bath first described by Feynman [24] to illustrate laws of thermodynamics. In both examples, the potential energy profile can consist of a number of potential minima, where the particle spends most of the time. At some instant of time random fluctuations transport the particle over the potential barrier, which corresponds to an advance of the reaction or a switch to another tooth of the ratchet. The primary task in such problems is to calculate the rate at which the particle escapes the potential minimum. It is also important to understand whether the particles on average tend to escape minima in a certain direction. This information may be extracted from the probability density function (PDF) of the position. The main result of chapter 4 is the steady-state PDF of the position of the particle in the generalized Kramers model in the limit of the short correlation time of the force. We discuss two asymptotic limits that correspond to large and small absolute values of the external forcing. It was shown by Monnai *et al.* [25] that in the weak external forcing limit the drift velocity is reduced. They concluded that in this limit the probability density is equivalent to a reduction of the potential compared with the classical Kramers model. The results of our numerical simulations cast doubt on this conclusion, and we present brief arguments suggesting that the correct result is, on the contrary, an increase of the potential. We also show that the probability density in the strong external forcing limit yields a non-zero probability flux of the particles for the motion in a periodic potential with a broken reflection symmetry.

1.1.3 Collision rate of inertial particles

In the fifth chapter we study the problem of the collision rate of inertial spherical particles. The collision rate is an important quantity, which can provide an insight into such processes as rain formation and planet formation. It is believed that small droplets of moisture in a cloud grow to form rain droplets due to collisions and subsequent aggregations [1]. Similarly, rocky planets are believed to be formed by aggregation of grain dust moving in the accretion disk around a star [3]. In this chapter we draw a particular attention to the dramatic increase of the collision rate occurring as the inertia of the particles passes a certain threshold. We argue that this increase is attributed to the formation of caustics discussed above. This is in contrast to the generally accepted view that the spatial clustering of particles is mainly due to ejection from vortices [1, 7, 26, 27]. This theory suggests that the clustering is strongest for moderate values of the inertia (in some dimensionless units), because for very small inertia the motion is overdamped, so that the droplets cannot escape vortices, whereas for very large inertia they are ejected too rapidly. We show that the collision rate remains high even for large inertia, where the clustering mechanism is not relevant. We argue that the collision rate R is of the form of an activated process, containing a factor similar to the Arrhenius law of the dependence of the chemical reaction rate on the temperature:

$$R = R_a + \exp(-S/\mathcal{I})R_g. \tag{1.3}$$

Here, R_a is the collision rate of particles advected by the flow, R_g is the collision rate of very heavy particles with the dynamics given by a gas-kinetic model, $\mathcal{I}$ is the dimensionless parameter measuring the intensity of turbulence (which also depends on the inertia of the particles), and S is a constant. Typically, $R_a \sim a^d$ and $R_g \sim a^{d-1}$, where a is the radius of the particle and d is the dimensionality of the space. The radius of the droplets which take part in aggregation processes in clouds is of order 10 μm, so that $R_a \ll R_g$. The exponential factor in Eq. (1.3) is the fraction of the coordinate space where the velocity field becomes multivalued due to the formation of caustics. The parameter $\mathcal{I}$ is then analogous to the temperature in a chemical

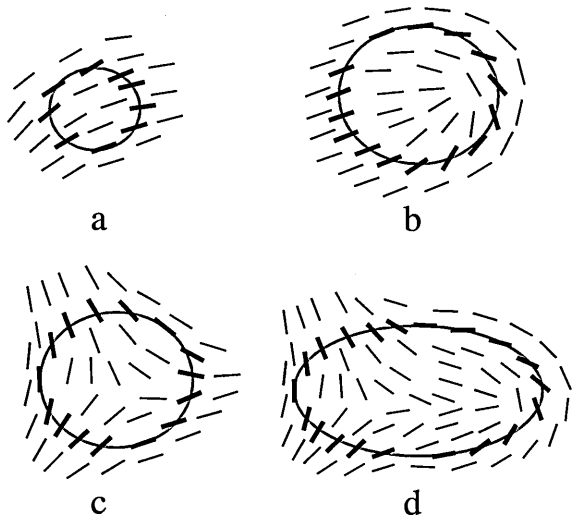

Figure 1.5: Illustrates the notion of the Poincaré index. For a vector field in the plane, the Poincaré index of a closed curve is the number of 2π clockwise rotations of the vector field as the curve is traversed, also clockwise. In non-oriented vector fields, singularities with a half-integer Poincaré index are possible: (**a**) index 0 for a non-singular field, (**b**) index $+\frac{1}{2}$ and (**c**) index $-\frac{1}{2}$. If the curve encloses two singularities, their indices are added: for example the Poincaré index of the curve in **d** is $\frac{1}{2} - \frac{1}{2} = 0$.

reaction, in the sense that when it exceeds S, the collision rate increases significantly.

1.1.4 Advection of small axisymmetric particles: textures and apparent singularities

The second part of the thesis is devoted to the study of some aspects of motion of advected non-spherical particles. We study motion of axisymmetric particles, for which their orientation can be specified by a single unit vector. We concentrate mostly on the two-dimensional case, where the orientation of the particle is given by one angle. The direction field of such particles in a plane form a non-oriented vector field, i.e. such that vectors with directions differing by π are considered to be equivalent. In such a field it is possible to observe topological singularities such as those seen in fingerprint patterns [28]. Several authors have discussed the dynamics of rod-like objects in different types of flows. Szeri [29] considered the tumbling motion of ellipsoidal particles in recirculating flows. Szeri and Leal [30] discussed motion of axisymmetric particles in more complex flows. Other authors have considered chaotic aspects of the motion of ellipsoids in complex flows [31, 32, 33, 34], but the topology

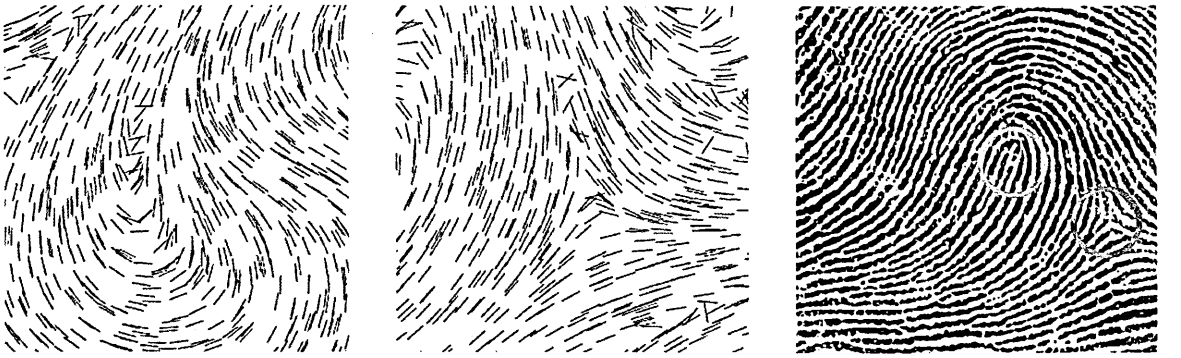

Figure 1.6: Shows textures of axisymmetric particles in an incompressible complex flow from the numerical simulation (**a** and **b**). The textures resemble fingerprint patterns (**c**) taken from [28]. In fingerprints the elementary singular points are known as the 'core' (with the Poincaré index $+\frac{1}{2}$) and the 'delta' (with the Poincaré index $-\frac{1}{2}$) and marked by red and green circles, respectively. Details of the numerical simulation are given in chapter 6.

of the orientation fields in this context has not been discussed before.

The topology of the vector field can be characterized by the topological invariant called the Poincaré index (illustrated in Fig. 1.5). The Poincaré index of a closed curve is the number of multiples of 2π by which the direction of the vector rotates in a clockwise direction as the curve is traversed, also clockwise. The index of the curve encircling a singularity is non-zero. The results of our numerical simulations presented in Fig. 1.6 support the idea of existence of singularities with a half-integer Poincaré index in the textures (i.e. patterns of the direction field) of axisymmetric particles advected in an incompressible complex flow. In the sixth chapter we discuss the formation of such structures and argue that it is in fact surprising to observe them. First, we find that the singularities cannot exist in a strict sense based on the solution of the equation of motion describing the dynamics of the orientation of the particles. The solution is given in terms of the product of the matrix describing the history of the flow along the trajectory of the particle (which we term the 'pseudomonodromy matrix') and the vector of the initial orientation of the particle. The pseudomonodromy matrix in an incompressible flow is a smooth function of the position and has the property that its determinant is always unity, so that if the initial direction field is continuous, the solution is non-singular at any time. This statement

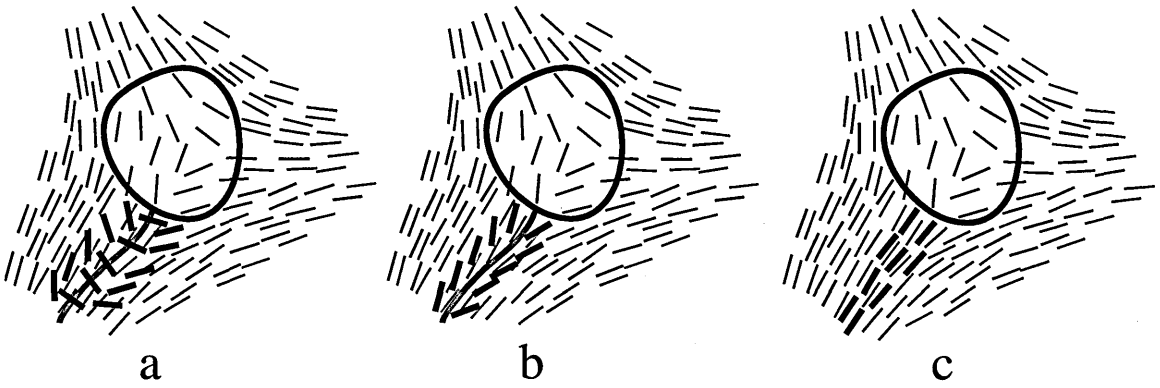

Figure 1.7: Schematic illustration showing how asymptotic singularities appear in textures of axisymmetric particles. The particle direction (black) is a smooth vector field containing a scar line (green). The particle direction field is asymptotic to the field of eigenvectors of the pseudomonodromy matrix (red) everywhere except around the scar line and inside the gyre, where the eigenvectors are complex (**a**). As time increases, the scar line narrows (**b**). When the scar line has narrowed to the extent that it does not include the actual position of any particle, it disappears (**c**). This leaves a point singularity at the end of the scar line: in this case a delta. In practice, the picture is more complex, because both the positions of the gyre and the scar line change with time.

apparently contradicts the results of numerical simulations in Fig. 1.6, where one can draw a set of closed curves with a non-zero Poincaré index. We suggest a resolution of this apparent contradiction by arguing that the singularities in the textures are approached in an asymptotic sense. We show that in an incompressible complex flow the orientation of the particle approaches the direction of the eigenvector of the pseudomonodromy matrix corresponding to the largest eigenvalue (which we term the 'dominant eigenvector'), implying that the textures of the particles at long times approach the configuration which is independent of their initial orientations. The field of dominant eigenvectors is non-singular, but can have a non-trivial topology in the following sense. Apart from degenerate cases, the pseudomonodromy matrix with the determinant unity in the two-dimensional case can have either two real reciprocal eigenvalues or two complex eigenvalues on a unit circle. At long times, the matrix has a distinct largest eigenvalue almost everywhere. At short times, however, the eigenvalues can be complex, and thus the field of dominant eigenvectors have regions (termed 'gyres'), where it is not defined. We find that the boundary of gyres can have a non-zero Poincaré index. Furthermore, in the regions where the dominant

Figure 1.8: Suspensions of anisotropic light-reflecting particles are used in education, art, and industry. Top: rheoscopic fluid is used as an educational tool for flow visualization, in this case for illustrating von Karman vortex street formed by the flow of a viscous fluid past a circular body [35] (image by the author of the thesis); left bottom: 'Rectangular Kalliroscope', installation art on display in Saibu Gas Museum, Fukuoka, Japan (reproduced with permission from the copyright owner, Kalliroscope Corporation); right bottom: pearlescent car paint, which may change its appearance depending on the viewing angle (reproduced with permission from House of Kolor).

eigenvectors are defined, the correspondence between two vector fields (particles and eigenvectors) breaks down along certain lines (termed 'scar lines'), which depend on the initial orientation of the particles. In the vicinity of these lines particles misalign with the corresponding eigenvectors, and on crossing the scar line the particles rapidly change direction by π. The region around a scar line, where the misalignment between the particles direction and eigenvectors is significant, shrinks rapidly, so that at later times there is a vanishingly small probability that any particle lies in the vicinity of the scar line. This process illustrated schematically in Fig. 1.7. At early times, the Poincaré index of a loop around a scar line and a gyre with a non-trivial topology is zero. When the scar line narrows, the change of angle associated with crossing the scar line disappears, and the Poincaré index of the loop becomes $\pm\frac{1}{2}$. For all practical purposes the scar line disappears in this case, but its end remains as a point singularity of the same type as those seen in fingerprints.

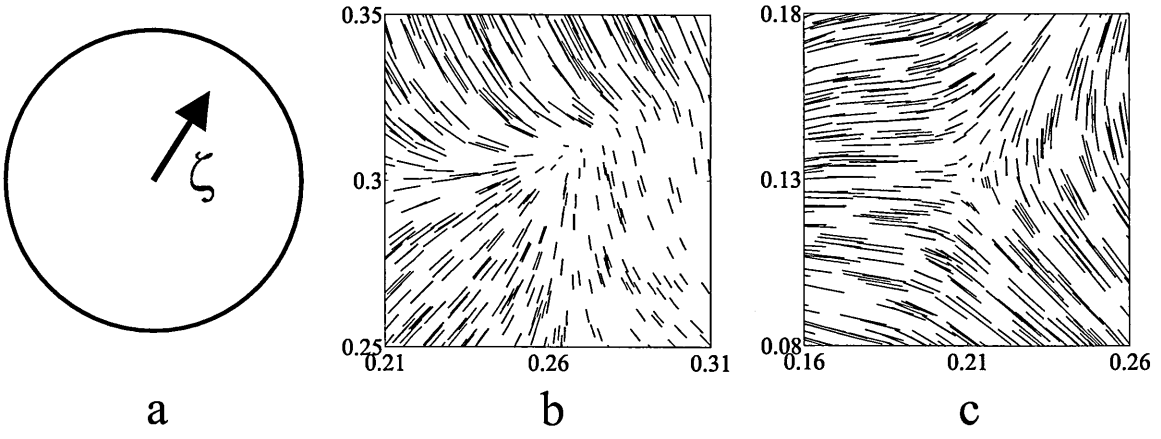

Figure 1.9: The degree of the alignment of axisymmetric particles is described by an order parameter vector $\boldsymbol{\zeta}$ lying within a unit circle (**a**). The vector points in the predominant direction of the alignment, with magnitude $0 \leq |\boldsymbol{\zeta}| \leq 1$ representing the degree of the alignment. The order parameter field exhibits singularities of the same type as those shown in Fig. 1.6. Panel **b** shows a core singularity and panel **c** shows a delta singularity.

1.1.5 Theoretical and experimental studies of rheoscopic visualizations

In the seventh chapter we continue discussing the textures of anisotropic particles and present an experiment on a rheoscopic fluid. A rheoscopic fluid is a suspension of microscopic elongated crystals, which reflect light in a complex way depending on their local alignment and ambient light. As illustrated in Fig. 1.8, suspensions of anisotropic light-reflecting particles are used in many areas of human activity, such as art, industry, education, etc. It is desirable to understand what aspects of the fluid motion are revealed by rheoscopic visualizations. In particular, we discuss how the apparent topological singularities discussed in the sixth chapter can be visualized using a rheoscopic fluid. We have mentioned that in an incompressible complex flow the long-time textures are independent of the initial orientations, but our explanation of the appearance of the topological singularities is specific to the form of the initial conditions, which have been assumed to be smooth. When the rheoscopic fluid is at rest, the crystals are randomly oriented due to the effect of Brownian motion, so that the initial orientation field is no longer smooth, but random and statistically isotropic. The rheoscopic fluid in this case appears uniform because the light is simply

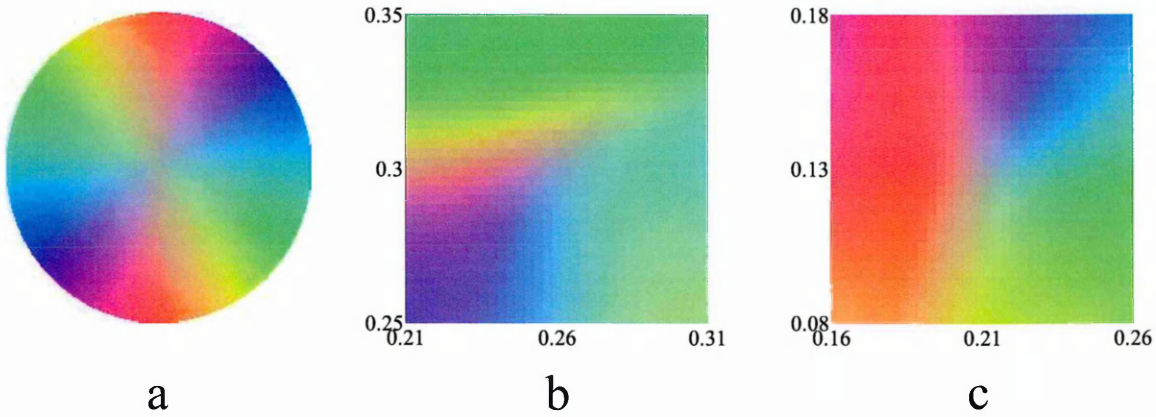

Figure 1.10: The order parameter field can be visualized using the colour map (**a**), which can be related to scattering of red, green and blue lights by a rheoscopic fluid. Because the orientation of the order parameter is irrelevant, this colour map is symmetric under reflection. The mapping between the order parameter field in Fig. 1.9 and the colour is shown in panels **b** and **c** for the core and delta singularities, respectively.

scattered by many crystals pointing in different directions. When the fluid is stirred, the particles start to align, and the intensity of the reflected light changes depending on their preferable orientation and the degree of their alignment. In chapter 7, we show how the solution of the equation of motion discussed in chapter 6 can be used to obtain the probability density of the orientation, which determines how an initially isotropic distribution of the particles evolves in time. We use this probability density to quantify the alignment of the particles by introducing the order parameter, which is a vector aligning with the predominant orientation of the particles at a given point in space, with its length representing the degree of the alignment, so that a zero length corresponds to an isotropic configuration, and a unit length corresponds to a perfect alignment. The order parameter field exhibits singularities with a half-integer Poincaré index, as illustrated in Fig. 1.9. Unlike the case in chapter 6, where the singularities are asymptotic, here the singularities are true and correspond to zeroes of the order parameter.

The order parameter field can be directly related to the reflection of light by the rheoscopic fluid. The intensity of the reflected light depends on a number of factors such as the ratio of the size of the crystals to the wavelength of light and their surface roughness. When the crystals are aligned, we expect that the light reflection

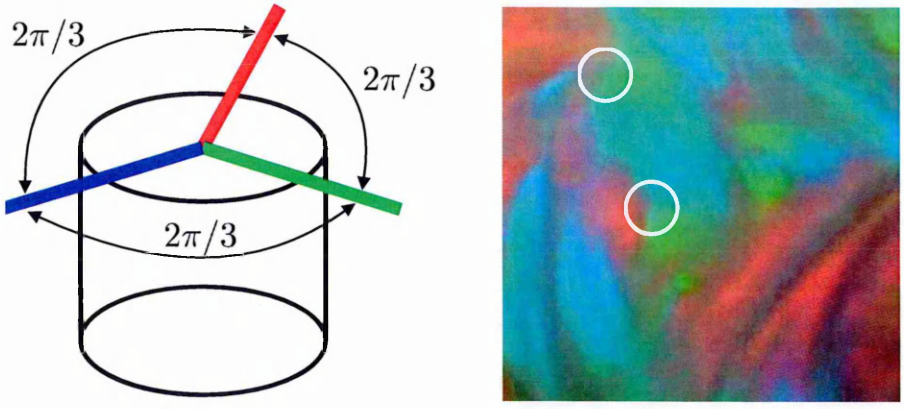

Figure 1.11: (**a**) A rheoscopic fluid is illuminated by three primary light sources (red, green and blue) arranged around a beaker at directions separated by $2\pi/3$. (**b**) The snapshot of the surface of the randomly stirred fluid. Circles indicate points with the property that on traversing a small circuit around a point in a clock-wise direction, the primary colours are encountered without repetition (in one case $R \to G \to B$, in the other $R \to B \to G$), which corresponds to the Poincaré index of $\pm 1/2$.

is strongest if the light source is perpendicular to the direction of the predominant orientation. If the surface of the rheoscopic fluid is illuminated by three coloured light sources, red (R), green (G), and blue (B), arranged around the sample at directions separated by 120°, the fluid reflects light with a colour C determined by an additive mixture of the primary colours:

$$C = I(0)R + I(2\pi/3)G + I(4\pi/3)B, \tag{1.4}$$

where $I(\theta)$ is a function which measures the intensity of the reflected light from a source oriented at the angle $\theta + \pi/2$ (a similar technique was used in [36] for different purposes). It reaches maximum when the particles at a given point in space are perfectly oriented in the direction θ. This function is specified in terms of the length and direction of the order parameter, and thus Eq. (1.4) maps the order parameter to a colour. The colour map is shown in Fig. 1.10, where we also plot the order parameter fields shown in Fig. 1.9 using Eq. (1.4). The topology of the field is determined by following shades of the primary colours on a closed curve. The Poincaré index is given by a number of full cycles of the primary colours, so that a sequence $R \to G \to B$ adds

$1/2$ to the total index, and a sequence $R \to B \to G$ subtracts $1/2$ from the total index of the curve. We conclude chapter 7 by discussing the results of the experiment which support the idea of existence of singularities with a half-integer Poinacaré index. In the experiment we stirred a thin layer of the rheoscopic fluid illuminated by three coloured light sources, oriented as explained above, to produce an additive colour mixture. We observed the surface of the rheoscopic fluid and determined the regions, where the primary colours make a single cycle, which corresponds to the singularities with a half-integer Poinacaré index. The sketch of the experiment and its outcome with such regions indicated are illustrated in Fig. 1.11.

Chapter 2

Review of basic principles, models, and methods

The purpose of this chapter is to discuss relevant principles, models, and methods which we shall employ further in the thesis. These include the Navier-Stokes equation for an incompressible fluid and models which can be used to mimic complex turbulent flows, equations of motion for both spherical and non-spherical particles based on the Stokes's approximation, and methods for analyzing diffusion of particles driven by random forces.

We shall discuss equations of motion both for fluids and particles. In most of the cases we shall employ a fixed Cartesian coordinate system, in which the points are specified by a radius-vector $\boldsymbol{r}$ relative to the origin. The radius-vector can be specified in terms of its components $r_1..r_d$, where d is the dimensionality of space. We shall also use for that purpose x, y and z and corresponding subscripts (depending on the dimensionality of the space). The list of other commonly used symbols is given in Table. 2.1.

2.1 Governing equations of fluid flows

Let us consider the velocity field of a fluid as a function of the position $\boldsymbol{r}$ and time t. The velocity field $\boldsymbol{u}(\boldsymbol{r}, t)$ of an incompressible viscous fluid satisfies the Navier-Stokes

Symbol	Meaning
t	time (T)
d	dimensionality of space (dimensionless)
$\boldsymbol{r}$, r_i, x, y, z	radius-vector of a point in space, position of a particle and its components (L)
$\mathbf{n}$	unit vector in the direction of the axis of symmetry of an axisymmetric particle
m	mass of the particle (M)
$\boldsymbol{v}$, v_i, v_x, v_y, v_z, v	velocity of a particle and its components (LT^{-1})
$\boldsymbol{p}$, p_i, p_x, p_y, p_z, p	momentum of a particle and its components (MLT^{-1})
ρ_p	density of a particle (ML^{-3})
a	radius of a spherical (circular) particle (L)
γ	damping rate (T^{-1})
$\boldsymbol{u}$, u_i, u_x, u_y, u_z, u	velocity of a fluid and its components (LT^{-1})
$\mathbf{A}$, A_{ij}	matrix of derivatives of the flow, Jacobian matrix (T^{-1})
$\mathbf{M}$, M_{ij}	monodromy matrix, pseudomonodromy matrix (dimensionless)
ρ_f	density of a fluid (ML^{-3})
μ	dynamic viscosity ($\mathrm{ML}^{-1}\mathrm{T}^{-1}$)
ν	kinematic viscosity ($\mathrm{L}^2\mathrm{T}^{-1}$)
η	length scale, Kolmogorov length scale (L)
τ	time scale, Kolmogorov time scale (T)
u_0	velocity scale, Kolmogorov velocity scale (LT^{-1})
ϵ	rate of energy dissipation per unit mass ($\mathrm{L}^2\mathrm{T}^{-3}$)
Re	Reynolds number (dimensionless)
St	Stokes number (dimensionless)
Ku	Kubo number (dimensionless)
D	diffusion coefficient, diffusion constant
v_d	drift velocity

Table 2.1: List of commonly used symbols and their meaning. The dimensionality is indicated in terms of units of mass (M), length (L), and time (T). For the diffusion constant and the drift velocity the dimensionality varies depending on the context of the problem.

equation. In its simplest form it is written as (see, e.g. [35])

$$\frac{\partial \boldsymbol{u}}{\partial t} + (\boldsymbol{u} \cdot \nabla)\boldsymbol{u} = -\frac{1}{\rho_f}\nabla p_f + \nu \nabla^2 \boldsymbol{u}, \tag{2.1}$$

where p_f is the pressure, ρ_f is the density of the fluid and ν is the kinematic viscosity. The velocity field also satisfies the incompressibility condition, $\nabla \cdot \boldsymbol{u} = 0$. The left-hand side of the Navier-Stokes equation is the total acceleration of the fluid element along its trajectory:

$$\frac{D\boldsymbol{u}}{Dt} = \frac{\partial \boldsymbol{u}}{\partial t} + (\boldsymbol{u} \cdot \nabla)\boldsymbol{u}, \tag{2.2}$$

and the right-hand side is the net force on the fluid element per unit mass. The Navier-Stokes equation in the form of (2.1) is then simply the Newton's second law of motion of a small element of the fluid with the assumption that the net force per unit mass on the fluid element is the sum of viscous terms and the gradient of the pressure. We remark that Eq. (2.1) may also be extended to include other forces, such as gravity or electromagnetic forces.

The last term on the right-hand side of Eq. (2.1) is a viscous force per unit mass derived from the stress tensor s_{ij}, which depends linearly on the strain-rate:

$$s_{ij} = 2\rho_f \nu E_{ij}, \tag{2.3}$$

where E_{ij} is a strain-rate tensor given by

$$E_{ij} = \frac{1}{2}\left(\frac{\partial u_i}{\partial r_j} + \frac{\partial u_j}{\partial r_i}\right). \tag{2.4}$$

This is the Newton's law of viscosity, and the fluids with such a dependence of the stress-tensor are called Newtonian, as opposed to non-Newtonian fluids, where the dependence of the stress tensor on the strain-rate tensor is not linear.

It is instructive to consider Eq. (2.1) in the dimensionless units. We set $\boldsymbol{u}' = \boldsymbol{u}/U$, $t' = tU/L$, $\boldsymbol{r}' = \boldsymbol{r}/L$ and $p'_f = p_f/(\rho_f U^2)$ where U, L are some suitable representative velocity and length scales, respectively. The Navier-Stokes equation in the new variables reads

$$\frac{\partial \boldsymbol{u}'}{\partial t'} + (\boldsymbol{u}' \cdot \nabla)\boldsymbol{u}' = -\nabla p'_f + \frac{1}{\mathrm{Re}}\nabla^2 \boldsymbol{u}', \tag{2.5}$$

where $\mathrm{Re} = UL/\nu$ is called the Reynolds number. The Navier-Stokes equation in the form of (2.5) contains only one dimensionless parameter Re, which can be interpreted as a measure of importance of inertial terms compared with viscous ones. If $\mathrm{Re} \ll 1$, then the non-linear term $(\boldsymbol{u}' \cdot \nabla)\boldsymbol{u}'$ in Eq. (2.5) is negligible, and the motion of the fluid is dominated by viscous forces. With the Reynolds number increasing, the non-linear term starts to be significant, and inertial effects become more important. For $\mathrm{Re} \gg 1$ the solution of the Navier-Stokes equation appears very irregular and chaotic

because of its sensitivity to the initial conditions, and the flow is said to be turbulent.

Although the Navier-Stokes equation is perfectly deterministic, the solution for $\mathrm{Re} \gg 1$ appears random and exhibits structures on many length and time scales. For this reason the statistical approach is widely used to describe turbulent flows. The statistical approach implies that the flow is described in terms of averages, probability densities, and structure functions (defined below). This approach is based on the idea of the energy cascade proposed by Richardson [14] and the 'Kolmogorov 1941 theory' [15] (hereafter referred to as 'K41 theory'). Richardson first suggested that a turbulent flow may be regarded as a collection of eddies of many different sizes, where the flux of the energy occurs from eddies of larger sizes to eddies of smaller sizes. According to this idea, structures of the largest scale L are formed by the processes that induce the flow, and all the energy is contained in these structures. They are unstable and break up to structures of smaller sizes distributing the energy among them. The energy cascades to smaller and smaller scales, until a certain length scale is achieved, so that molecular diffusion starts to play a role, and the energy is dissipated by the viscosity.

Richardson's ideas were quantified by Kolmogorov using a number of hypotheses. First, he suggested that for a sufficiently large Reynolds number the flow becomes statistically isotropic. Although large scale structures of the flow can be anisotropic, it is assumed that because of the energy cascade the information about the original geometry of the flow is lost. This implies that the structures on scales much smaller than L should have universal properties regardless of the energy source, which induces the flow.

The second hypothesis follows from the first one. It suggests that properties of the structures on the smallest scale, where the energy is dissipated, should only depend on the viscosity and the rate of energy dissipation per unit mass, ϵ. The smallest length scale η, therefore, can be derived from dimensional arguments:

$$\eta = \left(\frac{\nu^3}{\epsilon}\right)^{1/4}. \tag{2.6}$$

The corresponding time and velocity scales, τ and u_0, are similarly given by

$$\tau = \left(\frac{\nu}{\epsilon}\right)^{1/2},$$
$$u_0 = (\nu\epsilon)^{1/4}. \tag{2.7}$$

The third hypothesis of K41 theory concerns properties of the structures of sizes much larger than η, but still much smaller than the largest scale L. At these scales viscous forces in the fluid are negligible compared to inertial ones, and the properties, therefore, should not depend on ν. The range of such scales is called the inertial range, as opposed to the integral range, with scales comparable to L, and the viscous range, with scales comparable to η. From the first two hypotheses it follows that properties of the flow in the inertial range should only depend on ϵ and the scale r. The relevant function, which can be used to characterize the flow in this range, is the energy spectrum, $S(\boldsymbol{k})$ (for homogenous and isotropic flow it is a function of $|\boldsymbol{k}|$ only). The energy spectrum determines how the kinetic energy is distributed over different wavenumbers $k = |\boldsymbol{k}|$ in the Fourier transform of the velocity field corresponding to different scales $r = 2\pi/k$. The quantity $S(k)dk$ then yields a contribution of the kinetic energy (per unit mass) from the Fourier modes with $k < |\boldsymbol{k}| < k + dk$. From dimensional arguments, if $S(k)$ is the function of ϵ and k only, it follows that

$$S(k) = C_s \epsilon^{2/3} k^{-5/3}, \tag{2.8}$$

where C_s should be some universal constant, according to Kolmogorov. Using dimensional arguments we can also conclude the form of other important quantities. In particular, we can deduce the scaling of 'n-th order longitudinal structure function' [37], which can be used to determine how the flow is correlated at different points in space. The structure function is written in terms of the velocity increment $\delta u(r) = u_x(\boldsymbol{r}_0 + r\hat{\boldsymbol{e}}_x) - u_x(\boldsymbol{r}_0)$, where $\hat{\boldsymbol{e}}_x$ is the unit vector in the direction of x-axis.

From the dimensional arguments we deduce that in the inertial range

$$\langle [\delta u(r)]^n \rangle = C_n \epsilon^{n/3} r^{n/3}, \tag{2.9}$$

where C_n is again a universal constant according to Kolmogorov. For $n = 2$ the second-order structure function gives the well-known 'two-third' law of turbulence, confirmed in many experimental studies. However, it turns out that for $n > 2$ the structure function deviates from Eq. (2.9), and the universality of C_n's can not be confirmed. This phenomenon is called intermittency in turbulence. The problem of intermittency is an important area of research in modern studies of turbulence (see, e.g. [38]), but it is not relevant to the subject of this thesis, and we shall not look into it further.

2.2 Models of the flow

In the previous section we have discussed the equation governing the motion of fluids derived from first principles. We have mentioned that the behaviour of the solution of the Navier-Stokes equation depends on one dimensionless parameter, the Reynolds number. For $\mathrm{Re} \gg 1$ the solution of the Navier-Stokes equation becomes chaotic and exhibits motion on many length and time scales. This suggests that the numerical simulation of the Navier-Stokes equation requires a lot of computational power to resolve all scales, from largest to smallest. At present, the potential of numerical methods for solving the Navier-Stokes equation is limited to moderate values of Re, and it is unlikely that it would be possible to resolve flows with a sufficiently high Reynolds number in the near future. Even those simulations for moderate Re often require expensive parallel computations. Because turbulent flows appear random, it is a common practice to model them by random fields with appropriate statistical properties. In this section we describe some of the methods for generating such 'synthetic' turbulent flows, which we employ in our numerical simulations throughout the thesis.

2.2.1 Random stream functions and potentials

It is convenient to describe random velocity fields in terms of random stream functions and potentials. We start with a two-dimensional incompressible field, which can be written as a solenoidal field using a random stream function $\psi(x, y, t)$:

$$\boldsymbol{u}(\boldsymbol{r}, t) = \left(\frac{\partial \psi}{\partial y}, -\frac{\partial \psi}{\partial x} \right), \tag{2.10}$$

which automatically satisfies $\nabla \cdot \boldsymbol{u} = 0$. This can be also written in a short form as $\boldsymbol{u}(\boldsymbol{r}, t) = \nabla \times \psi \hat{\boldsymbol{e}}_z$, where $\hat{\boldsymbol{e}}_z$ is the unit vector in the z-direction (perpendicular to the plane xy). The random solenoidal field defined in Eq. (2.10) is incompressible but not irrotational. Although in section 2.1 we have discussed the equation of motion only for incompressible fluids, here we discuss compressible flows as well. The pure potential (irrotational) flow is given by $\boldsymbol{u}(\boldsymbol{r}, t) = \nabla \phi$, where $\phi(x, y, t)$ is a random potential. It is sometimes necessary to study a generic flow, which is a combination of incompressible and compressible parts:

$$\boldsymbol{u}(\boldsymbol{r}, t) = \nabla \times \psi \hat{\boldsymbol{e}}_z + c \nabla \phi, \tag{2.11}$$

where c is the number that determines the degree of compressibility.

We now specify properties of ψ and ϕ. We assume that ψ and ϕ are Gaussian random fields with zero mean, i.e. $\langle \psi(\boldsymbol{r}, t) \rangle = \langle \phi(\boldsymbol{r}, t) \rangle = 0$ (angular brackets denote average over many realizations of the random process). If we consider a flow in the form of Eq. (2.11), then ψ and ϕ are assumed to be statistically independent, i.e. $\langle \psi(\boldsymbol{r}, t) \phi(\boldsymbol{r}', t') \rangle = 0$. Furthermore, the random fields, ψ and ϕ, are assumed to be stationary, isotropic, and translationally invariant, with statistics determined by the correlation function

$$\langle \psi(\boldsymbol{r}, t) \psi(\boldsymbol{r}', t') \rangle = \langle \phi(\boldsymbol{r}, t) \phi(\boldsymbol{r}', t') \rangle = C(|\boldsymbol{r} - \boldsymbol{r}'|, |t - t'|). \tag{2.12}$$

We can generalize this approach for the case of three-dimensional flows. An in-

compressible velocity field in three spatial dimensions can be written as a solenoidal field via a three-dimensional vector potential $\boldsymbol{\Psi}(\boldsymbol{r},t)$, so that $\boldsymbol{u}(\boldsymbol{r},t) = \nabla \times \boldsymbol{\Psi}(\boldsymbol{r},t)$. Similarly to the two-dimensional case, we can consider a flow which is a combination of incompressible and compressible parts:

$$\boldsymbol{u}(\boldsymbol{r},t) = \nabla \times \boldsymbol{\Psi} + c\nabla\phi. \tag{2.13}$$

The statistical properties are similar to the two-dimensional case. The only distinction is that $\boldsymbol{\Psi}$ is now a three-dimensional vector, and we assume that its components are mutually statistically independent and also independent from ϕ, i.e.

$$\begin{aligned} \langle \boldsymbol{\Psi}_i(\boldsymbol{r},t)\boldsymbol{\Psi}_j(\boldsymbol{r}',t')\rangle &= \delta_{ij}C(|\boldsymbol{r}-\boldsymbol{r}'|,|t-t'|), \\ \langle \boldsymbol{\Psi}_i(\boldsymbol{r},t)\phi(\boldsymbol{r}',t')\rangle &= 0, \end{aligned} \tag{2.14}$$

where δ_{ij} is the Kronecker delta and $i,j = 1,2,3$.

2.2.2 The Fourier transform of the random field

The straightforward way to obtain a random function $\psi(\boldsymbol{r},t)$ with a given correlation function is by using its Fourier (spectral) transform given by an infinite sum

$$\psi(\boldsymbol{r},t) = \sum_{\boldsymbol{k},\omega} \tilde{\psi}(\boldsymbol{k},\omega)\mathrm{e}^{i(\boldsymbol{k}\cdot\boldsymbol{r}+\omega t)}. \tag{2.15}$$

The stream function is assumed to be spatially periodic in a d-dimensional box with a side of length L and also periodic in time with a period T, so that the corresponding spatial frequencies $\boldsymbol{k}$ are integer multiples of $2\pi/L$ and temporal frequency ω is an integer multiple of $2\pi/T$. The Fourier modes $\tilde{\psi}(\boldsymbol{k},\omega)$ are complex random variables with zero mean and variance given by the Fourier transform of the correlation function,

which determines the energy spectrum $S(\boldsymbol{k},\omega)$ of the random function,

$$S(\boldsymbol{k},\omega) = \langle\tilde{\psi}(\boldsymbol{k},\omega)\tilde{\psi}^*(\boldsymbol{k}',\omega')\rangle = \delta_{\boldsymbol{k}\boldsymbol{k}'}\delta_{\omega\omega'}L^{-d}T^{-1}\int_{-\infty}^{\infty}dr_1\ldots\int_{-\infty}^{\infty}dr_d\int_{-\infty}^{\infty}d\omega \times C(\boldsymbol{r},t)\mathrm{e}^{i(\boldsymbol{k}\cdot\boldsymbol{r}+\omega t)}, \tag{2.16}$$

where the asterisk denotes complex conjugation. Since ψ is real, we also have $\tilde{\psi}(\boldsymbol{k},\omega) = \tilde{\psi}^*(-\boldsymbol{k},-\omega)$.

In principle, if the correlation function is specified, and the integral in Eq. (2.16) can be evaluated, it is possible to generate the velocity field by calculating the derivatives of the stream function in Eq. (2.15). As far as the numerical summation in Eq. (2.15) is concerned, a number of important remarks should be made. In order to approximate the infinite sum, we introduce a cut-off number in the numerical simulations. The cut-off number is chosen according to the form of the correlation function and the corresponding energy spectrum. For example, the energy spectrum may decay rapidly with a mode number, and the cut-off number could be chosen such that $S(\boldsymbol{k},\omega)$ is sufficiently small. The numerical calculation of the sum itself requires care, as it is a triple sum for two-dimensional flows and a quadruple sum for three-dimensional flows, so that the time it takes to evaluate this sum grows rapidly with the number of terms. In many cases it is not advisable to calculate such sums using 'brute force' approach. The Fourier transform of the form (2.15) in general requires calculating the sum of order of N^{d+1} terms, where N is the typical cut-off number. However, numerical simulations are usually performed by discretizing the time variable, and we only need to know the velocity field at times $m\Delta t$, where m is an integer and Δt the time step (if the first-order Euler method for integration is used). Given that the time is discrete, we can use fast Fourier transform (FFT) [39] to evaluate sums in Eq. (2.15) as

$$\psi(\boldsymbol{r},m\Delta t) = \sum_{\boldsymbol{k}}\tilde{\psi}_m(\boldsymbol{k})\mathrm{e}^{i\boldsymbol{k}\cdot\boldsymbol{r}}. \tag{2.17}$$

Here, $\tilde{\psi}_m(\boldsymbol{k})$ are evaluated for all $\boldsymbol{k}$ and m using FFT at the beginning of the simula-

tion. The algorithm then reduces a triple sum to a double sum and a quadruple sum to a triple sum. The time it takes to evaluate $\tilde{\psi}_m(\boldsymbol{k})$ can sometimes be significant, but it only needs to be calculated once for a given simulation.

2.2.3 The Ornstein-Uhlenbeck method

The other way to generate a random function is to use the Fourier decomposition only for spatial variables [40]:

$$\psi(\boldsymbol{r},t) = \sum_{\boldsymbol{k}} \tilde{\psi}(\boldsymbol{k},t)\mathrm{e}^{i\boldsymbol{k}\cdot\boldsymbol{r}}, \tag{2.18}$$

where $\tilde{\psi}(\boldsymbol{k},t)$ are random processes in time. We set $\tilde{\psi}(\boldsymbol{k},t)$ to be Ornstein-Uhlenbeck processes [18]:

$$d\tilde{\psi}(\boldsymbol{k}) = -a_1(\boldsymbol{k})\tilde{\psi}(\boldsymbol{k})dt + \sqrt{2a_2(\boldsymbol{k})}dw_{\boldsymbol{k}}(t), \tag{2.19}$$

where $dw_{\boldsymbol{k}}$ is a sequence of random variables with statistics

$$\begin{aligned} \langle dw_{\boldsymbol{k}} \rangle &= 0, \\ \langle dw_{\boldsymbol{k}}(t) dw^*_{\boldsymbol{k}'}(t') \rangle &= \delta_{\boldsymbol{k}\boldsymbol{k}'}\delta(t-t')dt, \end{aligned} \tag{2.20}$$

where $\delta(x)$ is the Dirac delta function. The choice of the coefficients $a_1(\boldsymbol{k})$ and $a_2(\boldsymbol{k})$ determines the statistical properties of ψ. The statistics of $\tilde{\psi}(\boldsymbol{k},t)$ can be deduced from the solution of Eq. (2.19). We have

$$\tilde{\psi}(\boldsymbol{k},t) = N\mathrm{e}^{-a_1(\boldsymbol{k})t} + \sqrt{2a_2(\boldsymbol{k})}\int_0^t dw_{\boldsymbol{k}}(t')\ \mathrm{e}^{-a_1(t-t')}. \tag{2.21}$$

The correlation function of the Fourier components in the steady state is then given by

$$\langle \tilde{\psi}(\boldsymbol{k},t)\tilde{\psi}(\boldsymbol{k}',t+\Delta t)\rangle = \delta_{\boldsymbol{k}\boldsymbol{k}'}\frac{a_2(\boldsymbol{k})}{a_1(\boldsymbol{k})}\mathrm{e}^{-a_1(\boldsymbol{k})|\Delta t|}. \tag{2.22}$$

We only consider statistically stationary flows, so that $\tilde{\psi}(\boldsymbol{k}',t)$ must be stationary as well. This is achieved by choosing $\tilde{\psi}(\boldsymbol{k},0)$ from a normal distribution with zero

mean and variance $a_2(\boldsymbol{k})/a_1(\boldsymbol{k})$, which is a stationary distribution of Eq. (2.19). The correlation function of $\psi(\boldsymbol{r},t)$ in Eq. (2.18) can be calculated using Eq. (2.22). We have

$$\begin{aligned}\langle\psi(0,0)\psi(\boldsymbol{r},t)\rangle &= \sum_{\boldsymbol{k}_1}\sum_{\boldsymbol{k}_2}\langle\tilde{\psi}(\boldsymbol{k}_1,0)\tilde{\psi}(\boldsymbol{k}_2,t)\rangle \mathrm{e}^{i\boldsymbol{k}\cdot\boldsymbol{r}} \\ &= \sum_{\boldsymbol{k}} \frac{a_2(\boldsymbol{k})}{a_1(\boldsymbol{k})}\mathrm{e}^{-a_1(\boldsymbol{k})|t|+i\boldsymbol{k}\cdot\boldsymbol{r}}. \end{aligned} \tag{2.23}$$

If $a_1(\boldsymbol{k})$ is independent from $\boldsymbol{k}$, this is simplified to

$$\langle\psi(0,0)\psi(\boldsymbol{r},t)\rangle = \frac{\mathrm{e}^{-a_1|t|}}{a_1}\sum_{\boldsymbol{k}} a_2(\boldsymbol{k})\mathrm{e}^{i\boldsymbol{k}\cdot\boldsymbol{r}} = C(\boldsymbol{r})\frac{\mathrm{e}^{-a_1|t|}}{a_1}, \tag{2.24}$$

where

$$C(\boldsymbol{r}) = \sum_{\boldsymbol{k}} a_2(\boldsymbol{k})\mathrm{e}^{i\boldsymbol{k}\cdot\boldsymbol{r}}, \tag{2.25}$$

so that the correlation function $C(\boldsymbol{r})$ is determined by the Fourier transform of $a_2(\boldsymbol{k})$.

We remark that in our simulations we obtain the velocity field explicitly for a given point in space and time using either Eqs. (2.17) or (2.18). Alternatively, the flow may be obtained for a grid of points and the velocity field is then calculated using interpolation.

2.2.4 Correlation function

It remains to discuss the choice of the correlation function in Eq. (2.12). Numerical simulations in most of the problems in this thesis were done using the correlation function

$$C(r,t) = u_0^2\eta^2\mathrm{e}^{-\frac{r^2}{2\eta^2}-\frac{t^2}{2\tau^2}}. \tag{2.26}$$

The choice of this Gaussian correlation function is determined by a number of reasons. The corresponding spectrum in Eq. (2.16) is also Gaussian, and the function is smooth and differentiable for all values of its arguments. Because the energy spectrum is Gaussian, it decays rapidly with the mode number, so that the number of terms

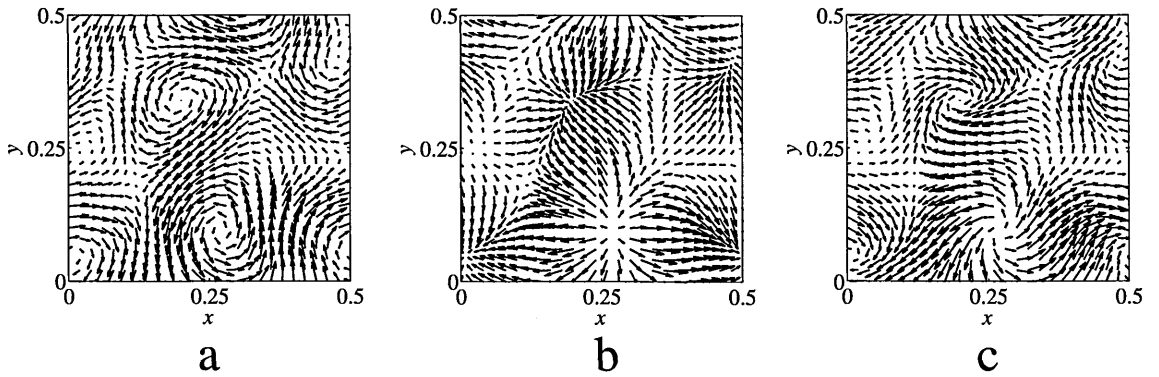

Figure 2.1: Three snapshots illustrating single-scale flows with the Gaussian correlation function (2.26). Panel **a** is an incompressible flow given by Eq. (2.10), panel **b** is a compressible flow given by $\boldsymbol{u}(\boldsymbol{r},t) = \nabla\phi$, and panel **c** is a combination of the incompressible and compressible fields given by Eq. (2.11) with $c = 0.75$. The parameters of the flow are $\eta = 0.1$, $\tau = 0.1$, $u_0 = 1$.

in the sum (2.15) required for an accurate approximation is typically quite small. The spatial structure of the flow is of a rather generic form. In Fig. 2.1**a** we present a typical snapshot of an incompressible two-dimensional velocity field with the Gaussian correlation function at a fixed time. The pattern consists of a set of stagnation points corresponding to regions of rotation (vortices) and hyperbolic saddle points. The flow is single-scale both spatially and temporally. The typical size of eddies is η with the typical time-scale τ and the typical speed u_0. The flow of this type can be seen as a turbulent flow on the smallest scale, where corresponding scales η, τ and u_0 are those given by the dimensional arguments of K41 theory. This is a useful approximation in problems where the motion on larger scales is not relevant. For completeness, in Fig. 2.1 we illustrate a compressible field derived using the same stream function and a combination of the solenoidal and potential fields.

In the Ornstein-Uhlenbeck method with a constant a_1, the spatial correlation function is determined by the choice of $a_2(\boldsymbol{k})$, whereas the temporal correlation function is single-scale with the time scale a_1^{-1}. We therefore set $a_1 = \tau^{-1}$ and $a_2(\boldsymbol{k}) = S(\boldsymbol{k})/\tau$, where $S(\boldsymbol{k})$ is the energy spectrum defined in this case as

$$S(\boldsymbol{k}) = L^{-d}\int_{-\infty}^{\infty} dr_1 \ldots \int_{-\infty}^{\infty} dr_d \int_{-\infty}^{\infty} C(\boldsymbol{r})\mathrm{e}^{i(\boldsymbol{k}\cdot\boldsymbol{r})}. \tag{2.27}$$

Thus, if this spectrum is Gaussian and depends only on $k = |\boldsymbol{k}|$, then C in Eq. (2.24)

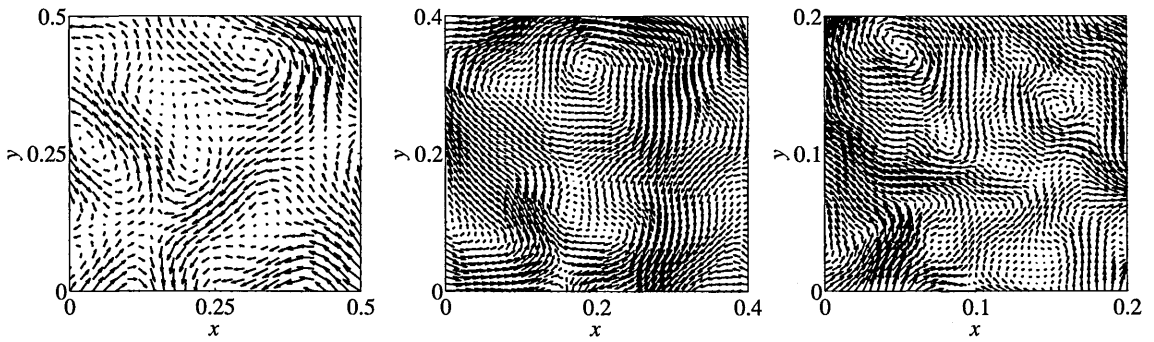

Figure 2.2: Three snapshot of an incompressible flow with the power-law energy spectrum derived from (2.18) and (2.19) with the parameters given by (2.29) for a different number of terms N in the sum: N=5 (**a**), $N = 10$ (**b**), N=20 (**c**). The parameters of the flow are $L = 1$, $\epsilon = 35$.

is also Gaussian and a function of $r = |\boldsymbol{r}|$ only. The velocity field in this case is very similar to the one described above with different, but still single-scale temporal behaviour. The drawback of using this method is that the correlation function (2.24) is not differentiable at $t = 0$. The method has an advantage that it is simpler to implement compared to the method based on the FFT, as it does not require an additional calculation of the Fourier modes at the beginning of the simulation, which can be cumbersome and may require a lot of physical memory to store the modes, especially in the three-dimensional case.

Another choice of $a_1(\boldsymbol{k})$ and $a_2(\boldsymbol{k})$, which is worth mentioning, makes it possible to mimic a power-law behaviour of turbulent flows in the inertial range. We write the longitudinal second-order structure function in two spatial dimensions as

$$\langle [u_x(x,0,t) - u_x(0,0,0)]^2 \rangle = (\epsilon x)^{2/3} f\left(\frac{t\epsilon^{1/3}}{x^{2/3}}\right), \tag{2.28}$$

where $f(z)$ is an arbitrary function. It can be shown that in this case we must set (see, e.g. [41])

$$\begin{aligned} a_1(k) &= \epsilon^{1/3} k^{2/3}, \\ a_2(k) &= \epsilon L^{-2} k^{-4}. \end{aligned} \tag{2.29}$$

Because the power-law spectrum decays slower then the Gaussian function, the number of terms in Eq. (2.18) is an important issue in this case. Fig. 2.2 illustrates the velocity field with the power-law spectrum for a different number of terms in the sum (2.18). We see that the flow exhibits structures on different scales, becoming more and more complex with a wider range of scales as the number of terms grows.

2.3 Equations of motion of particles

In this section we discuss equations describing the dynamics of a particle in a complex flow. The particle is assumed to be very small and can be treated as a point mass or a system of point masses connected by stiff rods (for the case of a non-spherical particle). The equation of motion of the particle is simply the Newton's law of motion:

$$\ddot{\boldsymbol{r}}(t) = \frac{\boldsymbol{F}}{m}. \tag{2.30}$$

Here, m is the mass of the particle, $\boldsymbol{r}(t)$ its position, and $\boldsymbol{F}$ is the net force exerted on the particle by the fluid. In the case of motion of a non-spherical, axisymmetric particle we are also interested in the dynamics of the orientation of the axis of symmetry of the particle given by

$$\dot{\boldsymbol{\omega}} = \frac{\boldsymbol{M}}{I}, \tag{2.31}$$

where $\boldsymbol{\omega}$ is the angular velocity, $\boldsymbol{M}$ is the net torque applied to the particle, and I is the moment of inertia. The torque on a particle can be written in terms of the forces acting on the particle as $\boldsymbol{M} = \boldsymbol{r}' \times \boldsymbol{F}$, where $\boldsymbol{r}'$ is the radius-vector of the particle relative to the point about which the particle rotates. It is therefore required to calculate forces acting on the particle in the fluid.

Below, we consider separately dynamics of spherical and non-spherical, axisymmetric particles, but few a general remarks for both cases can be made at this stage. If the particle is swept with a steady uniform flow, we expect that the net force on the particle vanishes. Thus, the force on the particle is associated with its relative motion to the fluid. When the particle with a typical linear dimension a is immersed

in a steady uniform flow with velocity u, it induces the disturbance of a flow, which depends on the Reynolds number based on the particle dimension, $\mathrm{Re}_a = ua/\nu$. If $\mathrm{Re}_a \ll 1$, then the flow around the particle is mainly due to viscosity, and it is the viscous drag which is the dominant force on the particle, because inertial effects are negligible. The drag force is calculated via the corresponding stress tensor s_{ij} defined in Eq. (2.3) with the velocity field satisfying the Navier-Stokes equation, which is simplified to

$$\nabla p = \mu \nabla^2 \boldsymbol{u}, \tag{2.32}$$

where $\mu = \nu \rho_f$ is the dynamic viscosity. Here, it is assumed that the flow around the particle remains steady. The equation should be supplemented with the incompressibility condition $\nabla \cdot \boldsymbol{u} = 0$ and the appropriate boundary and initial conditions. This equation can be solved explicitly in both cases of the flow past spherical and ellipsoidal (axisymmetric) particles.

2.3.1 Spherical particles

We consider a spherical particle of radius a in the steady translational motion with speed u in a fluid at rest (the discussion is valid if u is a relative speed of the particle in the frame of reference moving with a fluid in the steady translational motion). We can estimate the order of magnitude of the force acting on a sphere. The drag force on the particle is induced by the shear stress satisfying the Newton's law of viscosity (2.3). We can estimate the gradient of the velocity of the fluid around the sphere by u/a, so that the typical stress is given by

$$s \sim \frac{\mu u}{a}. \tag{2.33}$$

The magnitude of the force is simply the stress times the area:

$$F_d \sim \mu a u. \tag{2.34}$$

This rather crude estimate suggests that the magnitude of the force on a sphere is proportional to the (relative) speed of the particle. It was shown by Stokes [42] that the force acting on a sphere is the drag force with the magnitude

$$F_d = 6\pi\mu a u. \tag{2.35}$$

We now infer that a very similar law should hold for a particle in a non-uniform and unsteady (i.e. complex) flow $\boldsymbol{u}(\boldsymbol{r}, t)$. If the flow is complex, we assume that the direction of the drag force is given by the direction of the relative velocity, and the magnitude is given by the Stokes's law:

$$\boldsymbol{F}_d = 6\pi\mu a[\boldsymbol{u}(\boldsymbol{r}, t) - \dot{\boldsymbol{r}}(t)]. \tag{2.36}$$

We therefore can write the Newton's second law of motion as

$$m\ddot{\boldsymbol{r}} = 6\pi\mu a[\boldsymbol{u}(\boldsymbol{r}, t) - \dot{\boldsymbol{r}}(t)] \tag{2.37}$$

or

$$\ddot{\boldsymbol{r}} = \gamma[\boldsymbol{u}(\boldsymbol{r}, t) - \dot{\boldsymbol{r}}] \tag{2.38}$$

with the damping rate $\gamma = 6\pi\mu a/m$. In particular, in the three-dimensional case the mass of a spherical particle is given by $m = 4\pi a^3\rho_p/3$, where ρ_p is the density of the particle, so that the damping rate is given by $\gamma = 9\nu\rho_f/(2\rho_p a^2)$. The question remains whether the Stokes's formula for a steady uniform flow is accurate in this case. Maxey and Riley [43] analyzed the motion of rigid spherical particles in detail and introduced a number of different correction terms taking into account the complexity of the flow. They showed that for sufficiently small particles these correction terms can be safely neglected, so that Eq. (2.38) remains valid.

The dynamics described by Eq. (2.38) can be analyzed using a number of dimensionless parameters. The inertia of particles is measured using the Stokes number, $\mathrm{St} = (\gamma\tau)^{-1}$, where τ is a relevant time scale of the flow (in a turbulent flow it is the

Kolmogorov time scale). The Stokes number determines the degree to which motion of a particle is damped in the flow. For heavy particles with $\mathrm{St} \gg 1$ motion is underdamped, and for light particles with $\mathrm{St} \ll 1$ motion is overdamped. When $\mathrm{St} = 0$ particles are advected according to the equation

$$\dot{\boldsymbol{r}}(t) = \boldsymbol{u}(\boldsymbol{r}, t). \tag{2.39}$$

The velocity field is characterized by the Kubo number, Ku. In terms of the Kolmogorov scales, it is defined as $\mathrm{Ku} = u_0\tau/\eta$ and determines how rapidly the flow fluctuates. In a turbulent flow Ku cannot be large [9], but in some cases it can be small (for instance, in a randomly stirred fluid). Other relevant dimensionless parameters include the packing fraction, $n_0 = n\eta^d$, where n is the number density of particles and d is the dimensionality of space, and the relative size of particles $a_0 = a/\eta$ (if the system is monodisperse). In all problems considered in the thesis we assume that $n_0 \ll 1$ and $a_0 \ll 1$, so that effects of interaction between the particles and their influence on the flow are neglected.

Eq. (2.38) is a second-order differential equation, which can be written in a convenient form of two first-order equations. If we denote the momentum $\boldsymbol{p} = m\dot{\boldsymbol{r}}$, we obtain

$$\begin{aligned} \dot{\boldsymbol{r}} &= \frac{\boldsymbol{p}}{m}, \\ \dot{\boldsymbol{p}} &= -\gamma\boldsymbol{p} + \boldsymbol{f}(\boldsymbol{r}, t), \end{aligned} \tag{2.40}$$

where $\boldsymbol{f} = \gamma m\boldsymbol{u}$ is an effective force field. In this form Eq. (2.40) is similar to the Ornstein-Uhlenbeck process describing Brownian motion [18] (see also section 2.4.3).

It is possible to consider other forces acting on a particle in a flow. An obvious example is gravity, which makes rain droplets fall from the sky. A conservative force $\boldsymbol{g}(\boldsymbol{r}, t)$ can be written in the form $\boldsymbol{g}(\boldsymbol{r}, t) = -\nabla G(\boldsymbol{r}, t)$, where $G(\boldsymbol{r}, t)$ is the

corresponding potential, so that the equation of motion reads

$$\ddot{\boldsymbol{r}} = \gamma[\boldsymbol{u}(\boldsymbol{r},t) - \dot{\boldsymbol{r}}] - \frac{1}{m}\nabla G. \tag{2.41}$$

We remark that the Stokes formula and consequently the expression for γ is only valid if the mean free path of the fluid is much smaller compared to the size of the particles. In many astrophysical applications dust particles move in a gas, where this condition is not satisfied. In such cases Eq. (2.38) is still valid, but the damping rate is given by the Epstein formula [44], $\gamma = c_s\rho_f/\rho_p a$, where c_s is the speed of sound in the gas.

2.3.2 Non-spherical particles

We now turn to considering the case of non-spherical particles. We only consider axisymmetric particles advected by the flow. For an axisymmetric particle its orientation can be specified by a single unit vector $\mathbf{n}(t)$, and its position is given by the coordinate of the centre of mass $\boldsymbol{r}(t)$. If the particle is very small, it is expected that the dynamics of the centre of mass is advective and given by Eq. (2.39). The particle rotates and tumbles in response to the action of the strain rate of the flow $\mathbf{E} = \frac{1}{2}(\mathbf{A} + \mathbf{A}^T)$ (here, $\mathbf{A} = \partial u_i/\partial r_j$ and $\mathbf{A}^T$ is the transpose of $\mathbf{A}$) and vorticity $\boldsymbol{\omega} = \nabla \times \boldsymbol{u}$. The equation describing the dynamics of $\mathbf{n}(t)$ was first obtained by Jeffery [45] for the motion of an ellipsoid of revolution in a low Reynolds number flow. It was derived similarly to the Stokes law by solving the Navier-Stokes equation (2.32) for the flow past an ellipsoid of revolution with a given aspect ratio. The derivation of the equation of motion is rather subtle, and the result is less known than that of Stokes. Below, we describe an alternative way to derive the equation of motion that leads to the same result as the one obtained by Jeffery.

For simplicity we only derive the equation of motion in the two-dimensional case. Strictly speaking, we consider two rigidly connected dumbbells i.e. 4 spherical particles connected crosswise by stiff rods (see Fig. 2.3). The dumbbells are advected by the flow $\boldsymbol{u}(\boldsymbol{r},t)$, so that each particle experiences the drag force according to Eq. (2.36),

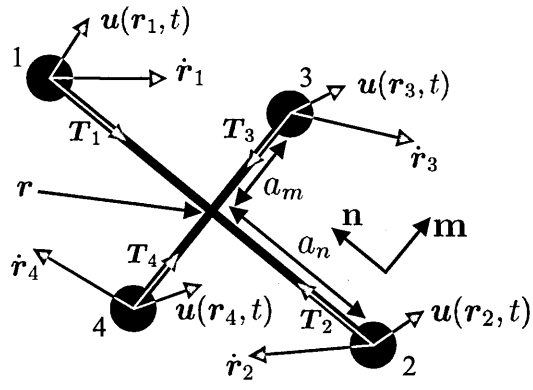

Figure 2.3: Two intersecting dumbbells advected by the flow $\boldsymbol{u}(\boldsymbol{r},t)$. The particles labelled 1,2,3 and 4 experience the drag force according to the Stokes's law, while the rods are not affected by the flow. The equations of motion are determined by the conditions that the net force and the net torque on four particles vanish.

while the rods are not affected by the flow. The position of the point of intersection of the dumbbells is denoted by $\boldsymbol{r}$, and directions of the dumbbells are given by two orthogonal unit vectors, $\mathbf{n}$ and $\mathbf{m}$. The lengths of the dumbbells are $2a_n$ and $2a_m$ corresponding to the directions specified by $\mathbf{n}$ and $\mathbf{m}$, respectively. This gives the aspect ratio $\alpha = a_n/a_m$. The positions of the particles labelled 1,2,3 and 4 in Fig. 2.3 are given by $\boldsymbol{r}_1 = \boldsymbol{r} + a_n\mathbf{n}$, $\boldsymbol{r}_2 = \boldsymbol{r} - a_n\mathbf{n}$, $\boldsymbol{r}_3 = \boldsymbol{r} + a_m\mathbf{m}$ and $\boldsymbol{r}_4 = \boldsymbol{r} - a_m\mathbf{m}$, respectively. The velocity of the flow at $\boldsymbol{r}_1$ (say) is then given by

$$\boldsymbol{u}(\boldsymbol{r}_1,t) = \boldsymbol{u}(\boldsymbol{r},t) + a_n\mathbf{A}(\boldsymbol{r},t)\mathbf{n} + O(a^2). \tag{2.42}$$

We assume that the typical length scale of the flow is much larger than a_n and a_m, so that the terms of order higher than $O(a_n)$ in Eq. (2.42) are negligible. This gives the linear approximation for the velocity difference:

$$\boldsymbol{u}(\boldsymbol{r}_1,t) - \boldsymbol{u}(\boldsymbol{r},t) \approx \mathbf{A}(\boldsymbol{r},t)\delta\boldsymbol{r}, \tag{2.43}$$

where $\delta\boldsymbol{r} = a_n\mathbf{n}$ is the separation vector. Since the particles are advected by the flow, their masses and moments of inertia are negligible, so that both the net force and the net torque sum to zero. The total force on four particles consists of the drag forces given by Eq. (2.36) and the forces of tension, which keep the separation between the particles fixed. Writing the sum of these forces acting on each particle and using the

linear approximation for the velocity difference we obtain

$$\begin{aligned}
&\gamma[\boldsymbol{u}(\boldsymbol{r},t)+a_n\mathbf{An}-\dot{\boldsymbol{r}}-a_n\dot{\mathbf{n}}]+\gamma[\boldsymbol{u}(\boldsymbol{r},t)-a_n\mathbf{An}-\dot{\boldsymbol{r}}+a_n\dot{\mathbf{n}}]\\
&+\gamma[\boldsymbol{u}(\boldsymbol{r},t)+a_m\mathbf{Am}-\dot{\boldsymbol{r}}-a_m\dot{\mathbf{m}}]+\gamma[\boldsymbol{u}(\boldsymbol{r},t)-a_m\mathbf{Am}-\dot{\boldsymbol{r}}+a_m\dot{\mathbf{m}}]\\
&+\boldsymbol{T}_1+\boldsymbol{T}_2+\boldsymbol{T}_3+\boldsymbol{T}_4=0,
\end{aligned}\tag{2.44}$$

where $\boldsymbol{T}_i$ is the force of tension associated with the i-th particle. We have $\boldsymbol{T}_1=-\boldsymbol{T}_2$ and $\boldsymbol{T}_3=-\boldsymbol{T}_4$, so that Eq. (2.44) is simplified to

$$\dot{\boldsymbol{r}}=\boldsymbol{u}(\boldsymbol{r},t).\tag{2.45}$$

The point of intersection of the dumbbells is therefore advected by the flow, as expected.

The torque on a particle is given by the cross product of the force acting on the particle and a radius-vector of the particle relative to the mid-point $\boldsymbol{r}$. We write the net torque:

$$\begin{aligned}
&a_n\mathbf{n}\times[\boldsymbol{u}(\boldsymbol{r},t)+a_n\mathbf{An}-\dot{\boldsymbol{r}}-a_n\dot{\mathbf{n}}+\boldsymbol{T}_1]\\
&-a_n\mathbf{n}\times[\boldsymbol{u}(\boldsymbol{r},t)-a_n\mathbf{An}-\dot{\boldsymbol{r}}+a_n\dot{\mathbf{n}}-\boldsymbol{T}_1]\\
&+a_m\mathbf{m}\times[\boldsymbol{u}(\boldsymbol{r},t)+a_m\mathbf{Am}-\dot{\boldsymbol{r}}-a_m\dot{\mathbf{m}}+\boldsymbol{T}_2]\\
&-a_m\mathbf{m}\times[\boldsymbol{u}(\boldsymbol{r},t)-a_m\mathbf{Am}-\dot{\boldsymbol{r}}+a_m\dot{\mathbf{m}}-\boldsymbol{T}_2]=0.
\end{aligned}\tag{2.46}$$

This can be simplified to

$$a_n^2\mathbf{n}\times\mathbf{An}-a_n^2\mathbf{n}\times\dot{\mathbf{n}}+a_m^2\mathbf{m}\times\mathbf{Am}-a_m^2\mathbf{m}\times\dot{\mathbf{m}}=0.\tag{2.47}$$

For any three vectors $\mathbf{a}$, $\mathbf{b}$ and $\mathbf{c}$ we have the following identities:

$$\begin{aligned}
\mathbf{a}\times\mathbf{b}&=-\mathbf{b}\times\mathbf{a},\\
\mathbf{a}\times(\mathbf{b}\times\mathbf{c})&=\mathbf{b}(\mathbf{a}\cdot\mathbf{c})-\mathbf{c}(\mathbf{a}\cdot\mathbf{b}).
\end{aligned}\tag{2.48}$$

Furthermore, for two orthogonal unit vectors $\mathbf{n}$ and $\mathbf{m}$ we have

$$\begin{aligned}\mathbf{n}\cdot\mathbf{n} &= \mathbf{m}\cdot\mathbf{m} = 1,\\ \mathbf{n}\cdot\dot{\mathbf{n}} &= \mathbf{m}\cdot\dot{\mathbf{m}} = \mathbf{n}\cdot\mathbf{m} = 0.\end{aligned} \tag{2.49}$$

Using these relations we take the cross product of (2.47) with $\mathbf{n}$ and obtain

$$-a_n^2[\mathbf{n}(\mathbf{n}\cdot\mathbf{An}) - \mathbf{An}] - a_n^2\dot{\mathbf{n}} - a_m^2\mathbf{m}(\mathbf{n}\cdot\mathbf{Am}) + a_m^2\mathbf{m}(\mathbf{n}\cdot\dot{\mathbf{m}}) = 0. \tag{2.50}$$

It can be shown that the following relations hold:

$$\begin{aligned}\mathbf{m}(\mathbf{n}\cdot\dot{\mathbf{m}}) &= -\dot{\mathbf{n}},\\ \mathbf{m}(\mathbf{n}\cdot\mathbf{Am}) &= \mathbf{A}^T\mathbf{n} - \mathbf{n}(\mathbf{n}\cdot\mathbf{A}^T\mathbf{n}).\end{aligned} \tag{2.51}$$

Thus, Eq. (2.50) is simplified to

$$\dot{\mathbf{n}} = \frac{a_n^2}{a_n^2+a_m^2}[\mathbf{An} - \mathbf{n}(\mathbf{n}\cdot\mathbf{An})] - \frac{a_m^2}{a_n^2+a_m^2}[\mathbf{A}^T\mathbf{n} - \mathbf{n}(\mathbf{n}\cdot\mathbf{A}^T\mathbf{n})]. \tag{2.52}$$

We introduce the weighted strain matrix $\mathbf{B}$:

$$\mathbf{B} = \frac{D_\alpha+1}{2}\mathbf{A} + \frac{D_\alpha-1}{2}\mathbf{A}^T, \qquad D_\alpha = \frac{\alpha^2-1}{\alpha^2+1}. \tag{2.53}$$

The equation of motion (2.52) is therefore

$$\dot{\mathbf{n}} = \mathbf{Bn} - \mathbf{n}(\mathbf{n}\cdot\mathbf{Bn}). \tag{2.54}$$

We have obtained the equation of motion which is independent of the lengths a_n and a_m (as $a_n \to 0$ and $a_m \to 0$) and only depends on their ratio α. We can imagine an ellipsoidal particle being formed by overlaying intersecting pairs of dumbbells of different lengths with the same aspect ratio, so that the equation describes a short

symmetric particle with a general distribution of the viscous drag along its length. In the three-dimensional case the model consists of 3 mutually perpendicular dumbbells described by a triplet of orthonormal vectors. The orientation of the axisymmetric particle is still given by a single unit vector and the equation of motion is the same as in the two-dimensional case. We note that in the three-dimensional case D_α ranges from -1 to 1, where $D_\alpha = -1$ corresponds to an infinitely thin disk, $D_\alpha = 0$ to a sphere, and $D_\alpha = 1$ to an infinitely thin rod. In the latter case the weighted matrix $\mathbf{B}$ is equal to the Jacobian matrix $\mathbf{A}$. In the two dimensional case, putting D_α to a negative value gives the dynamics of the shorter axis of an ellipsoid.

An equivalent equation of motion of an ellipsoid in terms of $\mathbf{E}$ and $\boldsymbol{\omega}$ is often used in other source (see, e.g. [31, 32, 34]):

$$\dot{\mathbf{n}} = \frac{1}{2}\boldsymbol{\omega} \times \mathbf{n} + D_\alpha \mathbf{n} \times (\mathbf{E} \cdot \mathbf{n}) \times \mathbf{n}. \tag{2.55}$$

We also remark that Bretherton [46] showed that the same equation is valid for an axisymmetric body of a more general shape than that of an ellipsoid of revolution. The definition of D_α may be different in such a case.

2.4 Diffusion of particles

We have mentioned earlier that the velocity field of a turbulent fluid appears random. Consequently, the dynamics of a particle in such a field can be seen as a sequence of apparently random displacements induced by the flow. This suggests that it is appropriate to describe such motion of the particle by a diffusion process of some type. In this section we describe a number of concepts and methods which are used in analyzing diffusion processes in application to chaotic motion of particles driven by random forces.

Diffusion can be defined as a transport of the matter by means of random motion. Quantitatively, diffusion can be described by the diffusion equation (in one spatial

dimension):

$$\frac{\partial P(x,t)}{\partial t} = \frac{\partial}{\partial x}\left[D(x,t)\frac{\partial P(x,t)}{\partial x}\right]. \tag{2.56}$$

Here $P(x,t)$ stands for some function of the position x and time t. The exact meaning of this function depends on the context of the problem. This could be a concentration of a given substance in the solution which undergoes mixing processes, distribution of heat in a solid body, etc. Here we are concerned with motion of particles, and throughout the thesis this function primarily stands for the probability density function (PDF) of the particle position and/or velocity. We remark that other quantities related to motion of the particles may also undergo diffusion. For example, when considering the problem of formation of caustics, we shall study diffusion of the ratio of the small change of the particle momentum and position, $X = \delta p/\delta x$.

The diffusion equation is derived from the continuity equation and the Fick's law of diffusion stating that the flux of the matter is proportional to the gradient of the density, so that the matter flows from regions of higher density to regions of lower density. The diffusion coefficient $D(x,t)$ in general depends on x and t, but in many important cases it can be taken as being a constant. An example of the diffusion equation with a constant diffusion coefficient (called simply a diffusion constant in this case) is the heat equation describing the variation of temperature in a system, where the diffusion constant can be related to the thermal conductivity.

The diffusion equation has an important consequence in application to motion of particles. Let us assume that the particles exhibit random motion, and the PDF of the position x at time t satisfies the diffusion equation with the diffusion constant D. If the particles start at $x(0) = 0$, the initial condition is written as $P(x,0) = \delta(x)$. The solution of the diffusion equation in this case is known to be Gaussian:

$$P(x,t) = \frac{1}{2\sqrt{\pi D t}}\exp\left(-\frac{x^2}{4Dt}\right). \tag{2.57}$$

Using this result we obtain

$$\langle x^2(t)\rangle = \int_{-\infty}^{\infty} dx\; x^2 P(x,t) = 2Dt, \tag{2.58}$$

i.e. the variance of $x(t)$ grows linearly with time. This is a characteristic property of a system which undergoes diffusion.

2.4.1 Random walks

The simplest microscopic model for diffusion is the model of random walks. The one-dimensional discrete model of random walks describes a particle making random jumps on a lattice. We assume for illustrative purposes that the particle jumps one site to the left or one site to the right with probability 1/2. Each jump can be described by a random variable X_i, which takes values +1 or -1 with an equal probability, so that $\langle X_i\rangle = 0$ and $\langle X_i X_j\rangle = \delta_{ij}$ assuming that the jumps are independent (the average is taken over many realizations of the random process). The equation of motion describing the position of the particle Y_N after N jumps reads

$$Y_N = X_0 + \sum_{i=1}^{N} X_i, \tag{2.59}$$

where X_0 is the initial position. We now calculate the statistical properties of Y_N. We assume for simplicity that the particle starts at $X_0 = 0$, so that the average of Y_N vanishes:

$$\langle Y_N\rangle = \sum_{i=1}^{N} \langle X_i\rangle = 0. \tag{2.60}$$

For the variance of Y_N we consider

$$\langle Y_N^2\rangle = \sum_{i=1}^{N}\sum_{j=1}^{N} \langle X_i X_j\rangle. \tag{2.61}$$

Since X_i and X_j are statistically independent for $i \neq j$, the double sum is reduced to the single sum:

$$\langle Y_N^2 \rangle = \sum_{i=1}^{N} \langle X_i^2 \rangle = N. \tag{2.62}$$

We obtain that the variance of the displacement is proportional to the number of jumps made, which is equivalent to the linear growth of $x(t)$ with time in Eq. (2.58). Thus, the particle in the model of random walks exhibits diffusive behaviour.

2.4.2 The Fokker-Planck equation

The Fokker-Planck equation is the main tool for studying diffusion processes which consist of many small independent random disturbances of the dynamical variable, similarly to the motion of a particle in the model of random walks. The equation describes a time evolution of the probability density function of a continuous stochastic variable $x(t)$ [47]:

$$\frac{\partial P(x,t)}{\partial t} = -\frac{\partial}{\partial x}[v_d(x)P(x,t)] + \frac{\partial^2}{\partial x^2}[D(x)P(x,t)]. \tag{2.63}$$

Here $D(x)$ is the diffusion coefficient and $v_d(x)$ is the drift velocity. The drift in a diffusion process may arise due to some systematic driving. It may also be a consequence of the random noise which depends on the dynamical variable, as we shall see in chapters 3 and 4. We remark that the diffusion equation (2.56) is not simply the Fokker-Planck equation without a drift, as the order of differentiation is different in both cases. The drift term and the diffusion coefficient in the Fokker-Planck equation are determined via the small increment of the dynamical variable δx in the time interval δt. The time δt is assumed to be large compared to the correlation time of the driving random noise in the model, but small compared to the correlation time of fluctuations of the stochastic variable. The drift velocity and the diffusion coefficient

are defined as follows:

$$v_d(x) = \frac{\langle \delta x \rangle}{\delta t},$$
$$D(x) = \frac{\langle \delta x^2 \rangle}{2\delta t}. \tag{2.64}$$

For diffusion processes, which can be described by the Fokker-Planck equation, it is assumed that the higher moments of δx are smaller than $O(\delta t)$.

The Fokker-Planck equation is a partial differential equation and should be supplemented with the boundary and initial conditions, as well as the normalization condition for the PDF. The Fokker-Planck equation is also the continuity equation for the probability density:

$$\frac{\partial P(x,t)}{\partial t} = -\frac{\partial J(x,t)}{\partial x}, \tag{2.65}$$

where $J(x,t)$ is the probability 'flux' given by

$$J(x,t) = v_d(x)P(x,t) - \frac{\partial}{\partial x}[D(x)P(x,t)]. \tag{2.66}$$

The Fokker-Planck equation can be solved explicitly only in a limited number of cases, in particular when $v_d(x)$ is linear and $D(x)$ is constant. In some case it suffices to determine the probability density in the steady state given by the condition

$$\frac{\partial P(x,t)}{\partial t} = 0. \tag{2.67}$$

In this case the Fokker-Planck for the stationary probability density $P_0(x)$ reads

$$v_d(x)P_0(x) - \frac{d}{dx}[D(x)P_0(x)] = J_0, \tag{2.68}$$

where J_0 is the probability flux in the steady state.

If a diffusion process is described by m dynamical variables, specified by a vector

$\boldsymbol{r} = (r_1, r_2 \ldots r_m)$, the multivariate Fokker-Planck equation reads

$$\frac{\partial P(\boldsymbol{r},t)}{\partial t} = -\sum_{i=1}^{m} \frac{\partial}{\partial r_i}[v_{di}(\boldsymbol{r})P(\boldsymbol{r},t)] + \sum_{i=1}^{m}\sum_{j=1}^{m} \frac{\partial^2}{\partial r_i \partial r_j}[D_{ij}(\boldsymbol{r})P(\boldsymbol{r},t)], \tag{2.69}$$

where $v_{di}(\boldsymbol{r})$ and $D_{ij}(\boldsymbol{r})$ are now elements of the drift velocity vector and the diffusion matrix, respectively, defined similarly to Eq. (2.64):

$$\begin{aligned} v_{di}(\boldsymbol{r}) &= \frac{\langle \delta r_i \rangle}{\delta t}, \\ D_{ij}(\boldsymbol{r}) &= \frac{\langle \delta r_i \delta r_j \rangle}{2\delta t}. \end{aligned} \tag{2.70}$$

In the remainder of the section we discuss two classical diffusion processes related to chaotic motion of particles and show how the Fokker-Planck equation can be employed to analyze them.

2.4.3 Brownian motion

The best studied diffusion process in nature is Brownian motion of small particles suspended in a fluid [48]. Although the particles are small in an everyday sense (these could be dust particles, pollen particles, etc.), they are large and heavy compared with the size of molecules of the fluid. The motion of heavy Brownian particles is induced by many collisions with these molecules, which themselves exhibit chaotic thermal motion. Individual collisions with the molecules happen on a very short time scale, and the displacement of the Brownian particle due to a single collision is extremely small. Individual collisions, therefore, remain undetected when the Brownian particle is observed. It is the net displacement after many collisions with the molecules which is observed, suggesting a relation of Brownian motion to the model of random walks, which we have discussed in section 2.4.1.

For the Brownian particle, there exists a time scale δt, which is much larger than the typical collision time, but at the same time much smaller than the correlation time of fluctuations of the displacement of the particle. At this time scale the particle experiences many collisions with the molecules of the fluid, but the growth of

the displacement is still small compared to the average value of the displacement. Although the position of the particle $x(t)$ is always continuous (for simplicity we only consider the one-dimensional case), the Brownian particle is observed to make independent random steps δx. The steps are statistically independent because the number of collisions in δt is very large. The statistics of the steps is given by

$$\begin{aligned} \langle \delta x \rangle &= 0, \\ \langle \delta x^2 \rangle &= 2D\delta t, \end{aligned} \tag{2.71}$$

where D is the diffusion constant which depends on the temperature T and the viscosity of the fluid, μ. It was shown by Einstein [49] that for the Brownian particle the diffusion constant is given by

$$D = \frac{k_B T}{6\pi\mu a}, \tag{2.72}$$

where k_B is the Boltzmann constant and a is the radius of the Brownian particle.

From the statistics of the steps we determine that the drift velocity vanishes, and the diffusion coefficient is D, so that the Fokker-Planck equation becomes the diffusion equation:

$$\frac{\partial P(x,t)}{\partial t} = D\frac{\partial^2 P(x,t)}{\partial x^2}. \tag{2.73}$$

The solution of this equation has already been given in Eq. (2.57) for the particular choice of the initial conditions, and we obtain that the variance of the displacement of the particle grows linearly with time, i.e.

$$\langle x^2(t) \rangle = 2Dt. \tag{2.74}$$

2.4.4 The Ornstein-Uhlenbeck process

In the previous section we have discussed motion of the Brownian particle on such a time scale, that the dynamics of the displacement of the particle consists of small independent random steps. In this description we have neglected fluctuations of the

velocity of the particle, which may grow and decay many times at this time scale. It is instructive to consider Brownian motion on a finer scale describing the dynamics of the velocity (or momentum). The equation of motion of the Brownian particle can be derived from first principles by considering forces acting on the particle and writing the Newton's equation of motion. The effect of collisions with the molecules can be split up into two parts. First, as the Brownian particle accelerates, it experiences more collisions with the molecules ahead of it than behind. This suggests that the velocity of the Brownian particle is damped due to the collisions. For the sake of simplicity, we assume that this damping is linear with the damping rate γ. In order to incorporate chaotic thermal motion of the molecules, we assume that the Brownian particle also experiences a rapidly fluctuating random force. The dynamics of the Brownian particle of mass m at position $x(t)$ with momentum $p(t)$ is therefore described by the following equation of motion:

$$\begin{aligned} \dot{x} &= \frac{p}{m}, \\ \dot{p} &= -\gamma p + f(t), \end{aligned} \tag{2.75}$$

where $f(t)$ is the random force. We assume that $\langle f(t) \rangle = 0$, so that the stationary particle is equally likely to be hit by the molecules from left and right. We also assume that the correlation between two values of $f(t)$ at different times t_1 and t_2 is significant only if $|t_1 - t_2|$ is very small, implying that the collisions time is very small compared to the time scale of fluctuations of the momentum given by γ^{-1}. The force $f(t)$ with such properties is called the Langevin force, and Eq. (2.75) is then the Langevin equation for the Brownian particle. The stochastic process defined by Eq. (2.75) with the Langevin force $f(t)$ is also called the Ornstein-Uhlenbeck process [18]. Other forces may also be introduced in Eq. (2.75) depending on the context of the problem. In particular, if the particle is subject to gravity or any other potential force, the dynamics of momentum is described by the equation

$$\dot{p} = -\gamma p + f(t) - U'(x), \tag{2.76}$$

where $U(x)$ is the potential. Similarly to the discussion of Brownian motion in the previous section, in the model given by (2.75), we can define the time interval δt, which is large compared to the correlation time of the random force τ, but small compared to the time scale at which the momentum relaxes, γ^{-1}. The dynamics of the momentum in this case is equivalent to a sequence of small independent increments δp in the time interval δt. The small increment of the momentum and the position is obtained by integrating Eq. (2.75) over the time interval δt:

$$\begin{aligned} \delta x &\equiv x(t_0+\delta t) - x(t_0) = \frac{p(t_0)}{m}\delta t, \\ \delta p &\equiv p(t_0+\delta t) - p(t_0) = -\gamma p(t_0)\delta t + \delta w, \end{aligned} \tag{2.77}$$

where

$$\delta w = \int_{t_0}^{t_0+\delta t} dt\ f(t). \tag{2.78}$$

We remark that by definition δt is small, so that the momentum does not change appreciably and is kept fixed in this case, but the force in Eq. (2.78) fluctuates significantly over this time interval, because $\delta t \gg \tau$. The dependence of $f(t)$ on t is smooth, so that differential and integral calculus are used here in the conventional sense, as opposed to the case when the random noise is a sequence of delta functions, for which Itô or Stratonovich interpretations for stochastic functions should be used [47]. We now calculate the statistical properties of δp in order to construct the Fokker-Planck equation. We have

$$\begin{aligned} \langle \delta p \rangle &= -\gamma p \delta t + \langle \delta w \rangle = -\gamma p, \\ \langle \delta p^2 \rangle &= \langle \delta w^2 \rangle + O(\delta t^2). \end{aligned} \tag{2.79}$$

We now calculate $\langle \delta w^2 \rangle$. If $f(t)$ is statistically stationary, we may set $t_0 = 0$ in Eq. (2.78) for calculating the statistical properties of δw. We therefore have

$$\langle \delta w^2 \rangle = \int_0^{\delta t} dt_1 \int_0^{\delta t} dt_2\ \langle f(t_1) f(t_2) \rangle. \tag{2.80}$$

If we denote $T = t_1 - t_2$ and use the fact that the noise is stationary, we obtain

$$\langle \delta w^2 \rangle = \delta t \int_{-\delta t}^{\delta t} dT \, \langle f(0) f(T) \rangle. \tag{2.81}$$

We note that $\langle f(0) f(T) \rangle$ is significant only when $|T| = O(\tau)$. We therefore can approximate

$$\langle \delta w^2 \rangle = \delta t \int_{-\infty}^{\infty} dT \, \langle f(0) f(T) \rangle \tag{2.82}$$

for $\delta t \gg \tau$. We conclude that

$$\langle \delta p^2 \rangle = 2D\delta t, \tag{2.83}$$

where

$$D = \frac{1}{2} \int_{-\infty}^{\infty} dT \, \langle f(0) f(T) \rangle \tag{2.84}$$

is the diffusion constant. The Fokker-Planck equation for the density of the momentum $P(p,t)$ therefore reads

$$\frac{\partial P(p,t)}{\partial t} = \gamma \frac{\partial}{\partial p}[pP(p,t)] + D\frac{\partial^2 P(p,t)}{\partial p^2}. \tag{2.85}$$

We remark that in this case it is not necessary to study the joint probability density $P(p,x,t)$ since the dynamics of p is independent of x, which is simply defined as

$$x(t) = x(0) + \frac{1}{m} \int_0^t dt_1 \, p(t_1). \tag{2.86}$$

The Fokker-Planck equation in this case can be solved exactly for the particular choice of the initial conditions. If the particle is initially at rest, the solution reads [47]

$$P(p,t) = \left[\frac{\gamma}{2\pi D(1 - \mathrm{e}^{-2\gamma t})} \right]^{1/2} \exp\left[-\frac{\gamma p^2}{2D(1 - \mathrm{e}^{-2\gamma t})} \right]. \tag{2.87}$$

We therefore obtain the second moment of the momentum:

$$\langle p^2(t) \rangle = \int_{-\infty}^{\infty} dp \, p^2 P(p,t) = \frac{D}{\gamma} \left(1 - \mathrm{e}^{-2\gamma t} \right). \tag{2.88}$$

We obtain that at short times the momentum grows linearly as $\langle p^2(t)\rangle \sim 2Dt$. At long times the system reaches a steady state due to the damping mechanism, and the distribution of the momentum is Maxwellian:

$$P_0(p) = \left(\frac{\gamma}{2\pi D}\right)^{1/2} \exp\left(-\frac{\gamma p^2}{2D}\right). \tag{2.89}$$

2.4.5 Anomalous diffusion

We have discussed two examples of the diffusion processes in which a particle is driven by a rapidly fluctuating random force. We infer that such type of processes might be relevant to the motion of particles in a turbulent flow, where particles experience apparently random impulses from the flow. The cases we have considered are characterized by the linear growth of the second moment of the dynamical variable (position or momentum). If the growth of a dynamical variable is not linear, the process is said to be anomalous diffusion. It is not easy to find natural physical models which exhibit anomalous diffusion. It is typical when anomalous diffusion is a consequence of some rather artificial properties built into the model. For instance, it may be a consequence of a power-law behaviour built into the dynamical process, such as Lévy flights, which is the model of random walks where the PDF of lengths of individual steps obeys power law. The cases when anomalous behaviour is an 'emergent' property are more interesting physically, but there are relatively few models where 'emergent' anomalous diffusion can be analyzed exactly. In chapter 3, we discuss a model of diffusion of heavy particles driven by random forces which exhibits anomalous diffusion.

Part I

Motion of spherical particles

Chapter 3

Universal anomalous diffusion of weakly damped particles

This chapter contains material from the paper of the same title by Wilkinson, Mehlig and Bezuglyy (unpublished, in preparation). The theory has been developed in collaboration, numerical experiments has been performed by the author of the thesis. Section 3.2 contains material published in [17], with some parts submitted by the author of the thesis for the degree of Master of Science.

3.1 Introduction

In this chapter we study diffusion of heavy particles driven by random forces. In section 2.4 we have discussed how motion of particles in turbulent flows can be related to models of diffusion, in particular, to the model of random walks and the Ornstein-Uhlenbeck process. We have also mentioned the notion of anomalous diffusion, when the growth of the dynamical variable X with time t satisfies $\langle X^2 \rangle \sim Ct^\alpha$ with $\alpha \neq 1$, as opposed to the ordinary diffusive behaviour with $\alpha = 1$. In this chapter we describe two physically natural models for diffusion of a particle accelerated by random forces which exhibit anomalous diffusion with universal exponents. Anomalous behaviour in these models is an 'emergent' property and is not a consequence of particular 'artificial' assumption built into microscopic equations of motion.

The models we study in this chapter are generalizations of two classical models for diffusion. The first is an extension of the Ornstein-Uhlenbeck process [18] described in section 2.4. Unlike the classical model (2.75), where the random force is only time-dependent, in the generalized one, the random force depends upon the position of the particle, as well as time. Earlier works [16, 17] analyzed this model in detail for one spatial dimension. This model exhibits anomalous diffusion, but here we discuss higher spatial dimensions, where the mechanism for anomalous diffusion is significantly different, as was suggested (for a closely related model) in [50, 51]. In section 3.2 we briefly summarize main concepts and results of the one-dimensional generalized Ornstein-Uhlenbeck process. We then consider this diffusion process in two and three spatial dimensions (for the case when the force is derived from the gradient of the random potential) and obtain the corresponding Fokker-Planck equation for the probability density of the momentum (section 3.3). In section 3.4 we discuss a transformation of the coordinates to the system where the diffusion matrix has a simple diagonal form due to rotational symmetry of the problem. In section 3.5 we discuss an extension of another classical diffusion process, the Chandrasekhar-Rosenbluth model for diffusion [21, 22], in which a test particle interacts with a gas of point masses via a pair potential. The interaction causes small changes of the momentum of the test particle, so that the dynamics of the momentum can be modelled as a diffusion process. Usually the interaction is gravitational, and the application is to the motion of stars in galaxies, but here we study the problem for the case of a non-singular weak interaction potential. We derive diffusion coefficients for this model precisely in terms of the macroscopic parameters of the model. Surprisingly, the diffusion matrix in this problem has the same form as in the generalized Ornstein-Uhlenbeck process. This leads to the same short-time asymptotic dynamics characterized by anomalous diffusion of the momentum with the same universal exponent. In section 3.6 we return to the Fokker-Planck equation and obtain the exact formulae for the PDF of the momentum of the particle in two and three dimensions for a particular choice of the initial conditions. We use these to obtain precise asymptotic formulae for moments of the momentum. In particular, we show that at short times the second moment

of the momentum grows as $t^{2/5}$, that is anomalously. In section 3.7, we show that the variance of the displacement of the particle at short times grows as t^2, that is ballistically. We also show that the long-time behaviour of the displacement is simply diffusive.

3.2 Generalized Ornstein-Uhlenbeck process in one spatial dimension

In order to make the analysis of the multidimensional model more transparent, we start by discussing the one-dimensional generalized Ornstein-Uhlenbeck process (analyzed in details in [16, 17]). The model describes a particle of mass m at position $x(t)$ with momentum $p(t)$ moving according to the equation of motion:

$$\begin{aligned} \dot{x} &= \frac{p}{m}, \\ \dot{p} &= -\gamma p + f(x,t). \end{aligned} \tag{3.1}$$

Unlike the classical diffusion process, here the random force is a function of the position, as well as time. The random force $f(x,t)$ is a stationary and translationally invariant Gaussian random process with the following statistics:

$$\begin{aligned} \langle f(x,t) \rangle &= 0, \\ \langle f(x,t) f(x',t') \rangle &= C(x-x', t-t'). \end{aligned} \tag{3.2}$$

The noise is characterized by its temporal and spatial scales, τ and η, respectively, and its typical magnitude σ. If we integrate Eq. (3.1) over a short time interval δt, such that $\tau \ll \delta t \ll \gamma^{-1}$, we obtain

$$\begin{aligned} \delta x &\equiv x(t_0+\delta t) - x(t_0) = \frac{p(t_0)}{m}\delta t, \\ \delta p &\equiv p(t_0+\delta t) - p(t_0) = -\gamma p(t_0)\delta t + \delta w, \end{aligned} \tag{3.3}$$

where

$$\delta w = \int_{t_0}^{t_0+\delta t} dt\ f[x(t), t]. \tag{3.4}$$

Because $\delta t \ll \gamma^{-1}$, the change of the momentum in this time interval is small. The random force, however, in the same time interval fluctuates appreciably because $\delta t \gg \tau$. The time interval δt can be defined if $\gamma\tau \ll 1$. In this case the diffusion process describing the dynamics of the momentum consists of many small independent disturbances implying that it can be analyzed using the Fokker-Planck equation for the probability density of the momentum $P(p,t)$:

$$\frac{\partial P(p,t)}{\partial t} = -\frac{\partial}{\partial p}[v_d(p)P(p,t)] + \frac{\partial^2}{\partial p^2}[D(p)P(p,t)]. \tag{3.5}$$

For the drift velocity $v_d(p)$ and the diffusion coefficient $D(p)$ we need to calculate the statistical properties of the random impulse δw. We have

$$\delta w = \int_{t_0}^{t_0+\delta t} dt\ f[x(t_0) + p(t-t_0)/m, t] + O(\delta t^2). \tag{3.6}$$

Without loss of generality, due to translational invariance and stationarity of the random force, we set $t_0 = 0$ and $x(t_0) = 0$ to obtain

$$\begin{aligned}\langle \delta w^2 \rangle &= \int_0^{\delta t} dt_1 \int_0^{\delta t} dt_2\ \langle f(pt_1/m, t_1) f(pt_2/m, t_2)\rangle \\ &= \int_0^{\delta t} dt_1 \int_0^{\delta t} dt_2\ C[p(t_1-t_2)/m, t_1-t_2].\end{aligned} \tag{3.7}$$

Denoting $T = t_1 - t_2$ we obtain

$$\langle \delta w^2 \rangle = \delta t \int_{-\delta t}^{\delta t} dT\ C(pT/m, T). \tag{3.8}$$

The integrand in this expression is significant in a small region along the line $T = 0$ because $\delta t \gg \tau$. In this case we may write

$$\langle \delta w^2 \rangle = \delta t \int_{-\infty}^{\infty} dt\ C(pt/m, t). \tag{3.9}$$

To the leading order in δt we have $\langle \delta p^2 \rangle = \langle \delta w^2 \rangle$, so that the diffusion coefficient for the fluctuations of the momentum is given by

$$D(p) = \frac{\langle \delta p^2 \rangle}{2\delta t} = \frac{1}{2} \int_{-\infty}^{\infty} dt \; C(pt/m, t). \tag{3.10}$$

Using the parameters of the model we may define a characteristic scale for the momentum, $p_0 = m\eta/\tau$. For $p \ll p_0$ the diffusion coefficient may be obtained by expanding the correlation function in series around $x = 0$:

$$D(p) = \frac{1}{2} \int_{-\infty}^{\infty} dt \; C(0, t) + O(p/p_0). \tag{3.11}$$

Thus, the diffusion constant for the classical Ornstein-Uhlenbeck process is recovered, when the momentum of the particle is small compared to p_0 [see Eq. (2.84)]. In this case the distance travelled by the particle in time of order τ is much smaller than η. Alternatively, when $p \gg p_0$, the particle in time interval τ travels the distance much larger than η, so that the diffusion coefficient characterizing fluctuations of the momentum will be smaller than that of the classical Ornstein-Uhlenbeck process. This happens because spatial fluctuations of the force effectively decrease the correlation time of the force experienced by the moving particle. The particle can gain high momentum if the damping is weak and the forcing is sufficiently strong. In this case we can write the diffusion coefficient (3.10) by changing the variables as $t = xm/p$ and expanding in series around $t = 0$:

$$D(p) = \frac{m}{2|p|} \int_{-\infty}^{\infty} dx \; C(x, xm/p) = \frac{m}{2|p|} \int_{-\infty}^{\infty} dx \; C(x, 0) + O(p_0/p)^2. \tag{3.12}$$

The results is therefore

$$D(p) = \frac{D_1 p_0}{|p|}, \tag{3.13}$$

where

$$D_1 = \frac{m}{2p_0} \int_{-\infty}^{\infty} dx \; C(x, 0). \tag{3.14}$$

The result for the diffusion coefficient given by Eq. (3.13) holds for a generic random noise $f(x,t)$ with a smooth and differentiable correlation function, provided that $D_1 \neq 0$. If the noise is derived from the random potential $V(x,t)$, so that $f(x,t) = -\partial_x V(x,t)$, we find that $D_1 = 0$. The diffusion coefficient in this case is obtained using Eq. (3.9)

$$D(p) = \frac{1}{2}\int_{-\infty}^{\infty} dt \left\langle \frac{\partial V}{\partial x}(0,0)\frac{\partial V}{\partial x}(pt/m,t)\right\rangle = -\frac{m}{2|p|}\int_{-\infty}^{\infty} dx \frac{\partial^2 C}{\partial x^2}(x, xm/p), \quad (3.15)$$

where $C(x,t)$ is the correlation function of the potential. Similarly to the generic case, when $p \gg p_0$, the diffusion coefficient can be obtained from series expansion, but here we expand to the order p^{-3}:

$$\begin{aligned} D(p) = &-\frac{m}{2|p|}\int_{-\infty}^{\infty} dx \frac{\partial^2 C}{\partial x^2}(x,0) - \frac{m}{2p^2}\int_{-\infty}^{\infty} dx\, x\frac{\partial^2 C}{\partial x^2 \partial t}(x,0) \\ &+ \frac{m^2}{4|p|^3}\int_{-\infty}^{\infty} dx\, x^2 \frac{\partial^2 C}{\partial x^2 \partial t^2}(x,0) + O(p/p_0)^4. \end{aligned} \quad (3.16)$$

It can be shown that in this case the coefficients for terms of order p^{-1} and p^{-2} vanish, and the leading non-vanishing term in the expansion is indeed of order p^{-3}, provided that the correlation function of $V(x,t)$ is sufficiently differentiable. We obtain

$$D(p) = \frac{D_3 p_0^3}{|p|^3}, \quad (3.17)$$

where

$$D_3 = -\frac{m^3}{2p_0^3}\int_{-\infty}^{\infty} dx \frac{\partial^2 C}{\partial t^2}(x,0). \quad (3.18)$$

When the noise is itself derived from the classical Ornstein-Uhlenbeck process (such as in the Ornstein-Uhlenbeck method for generating the random process described in section 2.2.3), the leading term is of order p^{-2}. It is therefore instructive to study the case where the diffusion coefficient scales as $D(p) \sim p^{-\zeta}$ for $\zeta > 0$ (this case is also discussed in [17]).

We now calculate the drift velocity using Eq. (3.3):

$$\frac{\langle \delta p \rangle}{\delta t} = -\gamma p + \langle \delta w \rangle. \tag{3.19}$$

Unlike the classical process, here $\langle \delta w \rangle$ does not simply vanish, because the average is calculated along the particle trajectory. We have

$$\langle \delta w \rangle = \int_0^{\delta t} dt \ \langle f[x(t), t] \rangle \tag{3.20}$$

We first expand $f(x,t)$ in series around a reference point $x_0 = pt/m$:

$$f(x,t) = f(pt/m, t) + \frac{\partial f(pt/m, t)}{\partial x}[x(t) - pt/m] + O(x^2), \tag{3.21}$$

where $x(t)$ is a solution of (3.1):

$$\begin{aligned} x(t) &= \frac{1}{m}\int_0^t dt_1 \int_0^{t_1} dt_2 \ \exp[-\gamma(t_1 - t_2)] \\ &\times \ f(pt_2/m, t_2) + O(t^2). \end{aligned} \tag{3.22}$$

The random impulse δw to the leading order in δt is therefore given by

$$\begin{aligned} \delta w \approx & \int_0^{\delta t} dt_1 \ f(pt_1/m, t_1) + \frac{1}{m}\int_0^{\delta t} dt_1 \ \frac{\partial f(pt_1/m, t_1)}{\partial x} \\ & \times \int_0^{t_1} dt_2 \int_0^{t_2} dt_3 \ \exp[-\gamma(t_2 - t_3)] f(pt_3/m, t_3) \\ & - \frac{p}{m}\int_0^{\delta t} dt_1 \ t_1 \frac{\partial f(pt_1/m, t_1)}{\partial x}. \end{aligned} \tag{3.23}$$

We note that $\langle f(pt/m, t) \rangle = \langle \partial_x f(pt/m, t) \rangle = 0$ for a fixed p and obtain

$$\begin{aligned} \langle \delta w \rangle &= \frac{1}{m}\int_0^{\delta t} dt_1 \int_0^{t_1} dt_2 \int_0^{t_2} dt_3 \ \exp[-\gamma(t_2 - t_3)] \\ &\times \left\langle \frac{\partial f(pt_1/m, t_1)}{\partial x} f(pt_3/m, t_3) \right\rangle. \end{aligned} \tag{3.24}$$

The integrand in this expression is dominant only for $t_1 - t_3 < \tau$. We have $t_3 \leq t_2 \leq t_1$

and can therefore approximate $\exp[-\gamma(t_2 - t_3)]$ by unity for $\gamma\tau \ll 1$ and $\delta t \ll \gamma^{-1}$. The integral over t_2 is then simply $t_1 - t_3$. By changing variables $t = t_1 - t_3$ we obtain

$$\langle \delta w \rangle = \frac{\delta t}{2m} \int_{-\delta t}^{\delta t} dt\, t \left\langle \frac{\partial f(pt/m, t)}{\partial x} f(0,0) \right\rangle \approx \frac{\delta t}{2} \int_{-\infty}^{\infty} dt\, \frac{\partial C}{\partial p}(pt/m, t). \tag{3.25}$$

In view of Eq. (3.10) we obtain $\langle \delta w \rangle$ in terms of the diffusion coefficient:

$$\langle \delta w \rangle = \delta t \frac{dD(p)}{dp}. \tag{3.26}$$

Then the drift velocity is given by

$$v_d(p) = -\gamma p + \frac{dD(p)}{dp}. \tag{3.27}$$

The Fokker-Planck equation for the probability density $P(p,t)$ therefore reads

$$\frac{\partial P(p,t)}{\partial t} = \frac{\partial}{\partial p}\left[\gamma p + D(p)\frac{\partial}{\partial p}\right] P(p,t) \tag{3.28}$$

The solution of this equation can be obtained for a particular choice of the initial conditions when the particles are initially at rest. In this case, for the diffusion coefficient given by Eq. (3.13), the normalized solution is

$$P(p,t) = \frac{\gamma^{1/3}}{2\Gamma(4/3)[3p_0 D_1(1 - \mathrm{e}^{-3\gamma t})]^{1/3}} \exp\left[-\frac{\gamma |p|^3}{3p_0 D_1(1 - \mathrm{e}^{-3\gamma t})}\right], \tag{3.29}$$

which is non-Maxwellian at large times (here $\Gamma(x)$ is the gamma function [52]). The growth of the momentum is given by

$$\langle p^2(t) \rangle = \int_{-\infty}^{\infty} dp\, P(p,t) p^2 = \frac{1}{\Gamma(1/3)} \left(\frac{3D_1 p_0}{\gamma}\right)^{2/3} (1 - \mathrm{e}^{-3\gamma t})^{2/3}. \tag{3.30}$$

Thus, when $t \ll \gamma^{-1}$, the momentum diffuses anomalously as $\langle p^2(t) \rangle \sim t^{2/3}$. For the case when the force is the derivative of the random potential, and the diffusion

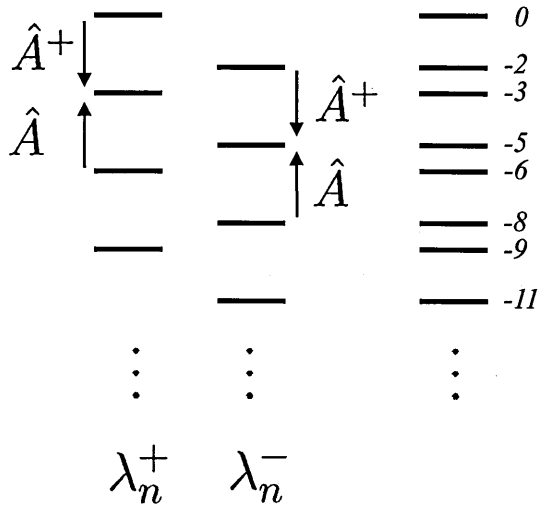

Figure 3.1: The spectrum of the Fokker-Planck operator in the one-dimensional generalized Ornstein-Uhlenbeck process consists of two equally spaced spectra, λ_n^+ and λ_n^-, which are shifted with respect to each other ('staggered'). Raising and lowering operators $\hat{A}$ and $\hat{A}^+$ are used to map eigenfunctions corresponding to different eigenvalues.

coefficient is given by Eq. (3.17) the corresponding solution reads

$$P(p,t) = \frac{\gamma^{1/5}}{2\Gamma(6/5)[5p_0^3 D_3(1-\mathrm{e}^{-5\gamma t})]^{1/5}} \exp\left[-\frac{\gamma|p|^5}{5p_0^3 D_3(1-\mathrm{e}^{-5\gamma t})}\right], \tag{3.31}$$

so that the momentum at short times grows as $\langle p^2(t)\rangle \sim t^{2/5}$.

In order to obtain other important quantities, the solution for a particular choice of the initial conditions is not sufficient. It is necessary to find the propagator of the Fokker-Planck equation $K_p(p, p_0, t)$, which is the probability density for the momentum to reach p after time t starting from p_0. Although the Fokker-Planck equation (3.28) is non-linear, in the sense that the diffusion coefficient is not a constant, it is possible to solve it explicitly, as explained in [16, 17]. The Fokker-Planck equation can be mapped to an operator acting on the probability density. It turns out that the spectrum of this operator is of a very peculiar form. It consists of two equally spaced ladders of levels which are shifted with respect to each other. Such a spectrum is termed 'staggered ladder spectrum' and illustrated in Fig. 3.1. The propagator can be written in terms of eigenfunctions of the Fokker-Planck operator, which can be found using creation and annihilation (or raising and lowering) operators of quantum mechanics. Using the propagator, the law of spatial diffusion can be found. For the

process with the diffusion coefficient given by Eq. (3.13) the variance of the displacement of the particles grows as $\langle x^2(t)\rangle \sim t^{8/3}$ at short times (if the particles are initially at rest). For the diffusion process with the diffusion coefficient given by Eq. (3.17) the variance of the displacement at short times grows as $\langle x^2(t)\rangle \sim t^{12/5}$. In both cases the long-time behaviour is diffusive, i.e. $\langle x^2(t)\rangle \sim 2D_x t$ with the diffusion constant D_x which can be written in terms of the macroscopic parameters of the model.

3.3 Generalized Ornstein-Uhlenbeck process in two and three spatial dimensions

In this section we discuss the generalized Ornstein-Uhlenbeck process in $d = 2, 3$ spatial dimensions. The equation of motion of the particle of mass m at position $\boldsymbol{r}(t)$ with momentum $\boldsymbol{p}(t)$ reads

$$\begin{aligned} \dot{\boldsymbol{r}} &= \frac{\boldsymbol{p}}{m}, \\ \dot{\boldsymbol{p}} &= -\gamma \boldsymbol{p} + \boldsymbol{f}(\boldsymbol{r}, t), \end{aligned} \tag{3.32}$$

We study the case when the force is generated by a random potential varying in time and space, so that

$$\boldsymbol{f}(\boldsymbol{r}, t) = -\nabla \psi(\boldsymbol{r}, t). \tag{3.33}$$

The potential ψ is assumed to have isotropic, translationally invariant, and stationary statistics determined by Eq. (2.12). We assume that the correlation function of the potential $C(x, t)$ has temporal and spatial correlation scales, τ and η, respectively, and a typical magnitude σ. We also assume that $C(x, t)$ is sufficiently smooth and differentiable. We remark that in section 3.7 we shall also briefly comment on the motion in a solenoidal (incompressible) force field.

Similarly to the one-dimensional model, when the damping is weak and the forcing is strong enough, the particle can gain the momentum which is much larger than the typical momentum p_0. The diffusion coefficient describing fluctuations of the mo-

mentum is therefore expected to decrease. If the random force fluctuates sufficiently rapidly, so that $\gamma\tau \ll 1$, the dynamics of the particle can be written in terms of small increments of the position and momentum, $\delta\boldsymbol{r}$ and $\delta\boldsymbol{p}$. In terms of components of $\delta\boldsymbol{r}$ and $\delta\boldsymbol{p}$ we obtain

$$\begin{aligned} \delta r_i &= \frac{p_i}{m}\delta t, \\ \delta p_i &= -\gamma p_i \delta t + \delta w_i, \end{aligned} \tag{3.34}$$

where δt is a small time interval satisfying $\tau \ll \delta t \ll \gamma^{-1}$ and $i = 1 \ldots d$. The increment δw_i is a random impulse exerted by the i-th component of the force on the particle in time δt:

$$\begin{aligned} \delta w_i &= \int_{t_0}^{t_0+\delta t} dt_1 \; f_i[\boldsymbol{r}(t_1), t_1] \\ &= \int_{t_0}^{t_0+\delta t} dt_1 \; f_i(\boldsymbol{r}_0 + \boldsymbol{p}t_1/m, t_1) + O(\delta t^2), \end{aligned} \tag{3.35}$$

where $\boldsymbol{r}_0 = \boldsymbol{r}(t_0)$. We use Eq. (3.34) to derive the drift velocity vector with components $v_{di}(\boldsymbol{p}) = \langle \delta p_i \rangle / \delta t$ and the elements of the diffusion matrix $D_{ij}(\boldsymbol{p}) = \langle \delta p_i \delta p_j \rangle / (2\delta t)$. The calculations are done similarly to the one-dimensional model. Using the properties of the potential we can set $t_0 = 0$ and $r_i(0) = 0$ for calculating the statistical properties of δw_i and δp_i. The drift velocity is given by

$$v_{di}(\boldsymbol{p}) = -\gamma p_i + \frac{\langle \delta w_i \rangle}{\delta t}. \tag{3.36}$$

We expand $f_i(\boldsymbol{r}, t)$ in series:

$$f_i(\boldsymbol{r}, t) = f_i(\boldsymbol{p}t/m, t) + \sum_{j=1}^{d} \frac{\partial f_i(\boldsymbol{p}t/m, t)}{\partial r_j} [r_j(t) - p_j t/m] + O(|\boldsymbol{r}|)^2, \tag{3.37}$$

and write $r_j(t)$ as a formal solution of (3.32):

$$\begin{aligned} r_j(t) &= \frac{1}{m}\int_0^t dt_1 \int_0^{t_1} dt_2 \, \exp[-\gamma(t_1 - t_2)] \\ &\times \; f_j(\boldsymbol{p}t_2/m, t_2). \end{aligned} \tag{3.38}$$

The random increment in Eq. (3.35) is therefore given by

$$\begin{aligned} \delta w_i \approx & \int_0^{\delta t} dt_1 \; f_i(\boldsymbol{p}t_1/m, t_1) + \frac{1}{m}\int_0^{\delta t} dt_1 \sum_{j=1}^{d} \frac{\partial f_i(\boldsymbol{p}t_1/m, t_1)}{\partial r_j} \\ & \times \int_0^{t_1} dt_2 \int_0^{t_2} dt_3 \exp[-\gamma(t_2 - t_3)] f_j(\boldsymbol{p}t_3/m, t_3) \\ & - \int_0^{\delta t} dt_1 \sum_{j=1}^{d} \frac{\partial f_i(\boldsymbol{p}t_1/m, t_1)}{\partial r_j} \frac{p_j t}{m}. \end{aligned} \tag{3.39}$$

The force is assumed to have zero mean, so we obtain

$$\begin{aligned} \langle \delta w_i \rangle &= \frac{1}{m}\sum_{j=1}^{d} \int_0^{\delta t} dt_1 \int_0^{t_1} dt_2 \int_0^{t_2} dt_3 \, \exp[-\gamma(t_2 - t_3)] \\ &\times \left\langle \frac{\partial f_i(\boldsymbol{p}t_1/m, t_1)}{\partial x_j} f_j(\boldsymbol{p}t_3/m, t_3) \right\rangle. \end{aligned} \tag{3.40}$$

Similarly to the one-dimensional case, the integrand is dominant around the line $t_1 = t_3$ and we obtain [c.f. Eq. (3.25)]:

$$\langle \delta w_i \rangle = \frac{\delta t}{2m} \sum_{j=1}^{d} \int_{-\infty}^{\infty} dt \; t \left\langle \frac{\partial f_i(\boldsymbol{p}t/m, t)}{\partial r_j} f_j(\boldsymbol{0}, 0) \right\rangle. \tag{3.41}$$

In terms of the correlation function of the potential we have

$$\begin{aligned} \langle \delta w_i \rangle &= \frac{\delta t}{2m} \sum_{j=1}^{d} \int_{-\infty}^{\infty} dt \; t \left\langle \frac{\partial^2 \psi}{\partial r_i \partial r_j}(\boldsymbol{p}t/m, t) \frac{\partial \psi}{\partial r_j}(\boldsymbol{0}, 0) \right\rangle \\ &= -\frac{\delta t}{2m} \sum_{j=1}^{d} \int_{-\infty}^{\infty} dt \; t \; \frac{\partial^3}{\partial r_i \partial r_j^2} C(|\boldsymbol{p}|t/m, t). \end{aligned} \tag{3.42}$$

By changing variables $r_i = p_i t/m$ we obtain:

$$\frac{\langle \delta w_i \rangle}{\delta t} = -\frac{m^2}{2} \sum_{j=1}^{d} \int_{-\infty}^{\infty} dt\ t^{-2} \frac{\partial^3 C}{\partial p_i \partial p_j^2}(|\boldsymbol{p}|t/m, t). \tag{3.43}$$

For the diffusion coefficient, $\langle \delta p_i \delta p_j \rangle$ can be replaced by $\langle \delta w_i \delta w_j \rangle$ to the leading order in δt. We have

$$\begin{aligned} \langle \delta p_i \delta p_j \rangle &= \int_0^{\delta t} dt_1 \int_0^{\delta t} dt_2\ \langle f_i(\boldsymbol{p}t_1/m, t) f_j(\boldsymbol{p}t_2/m, t_2) \rangle + O(\delta t^2) \\ &\approx \delta t \int_{-\infty}^{\infty} dt\ \langle f_i(\mathbf{0}, 0) f_j(\boldsymbol{p}t/m, t) \rangle. \end{aligned} \tag{3.44}$$

In terms of the correlation function of the potential we obtain the diffusion coefficients

$$\begin{aligned} \frac{\langle \delta p_i \delta p_j \rangle}{2\delta t} &= \frac{1}{2} \int_{-\infty}^{\infty} dt\ \left\langle \frac{\partial \psi}{\partial r_i}(\mathbf{0}, 0) \frac{\partial \psi}{\partial r_j}(\boldsymbol{p}t/m, t) \right\rangle \\ &= -\frac{1}{2} \int_{-\infty}^{\infty} dt\ \frac{\partial^2}{\partial r_i \partial r_j} C(|\boldsymbol{p}|t/m, t). \end{aligned} \tag{3.45}$$

By changing variables $r_i = p_i t/m$ we obtain

$$D_{ij}(\boldsymbol{p}) = -\frac{m^2}{2} \int_{-\infty}^{\infty} dt\ t^{-2} \frac{\partial^2}{\partial p_i \partial p_j} C(|\boldsymbol{p}|t/m, t). \tag{3.46}$$

We note that combining together Eqs. (3.43) and (3.46) gives

$$\frac{\langle \delta w_i \rangle}{\delta t} = \sum_{j=1}^{d} \frac{\partial}{\partial p_j} D_{ij}(\boldsymbol{p}). \tag{3.47}$$

Thus, the Fokker-Planck equation for the probability density $P(\boldsymbol{p}, t)$ for the multidimensional model is very similar to the one-dimensional case. We obtain

$$\frac{\partial P(\boldsymbol{p}, t)}{\partial t} = \frac{\partial}{\partial \boldsymbol{p}} \cdot \left(\gamma \boldsymbol{p} + \mathbf{D}(\boldsymbol{p}) \frac{\partial}{\partial \boldsymbol{p}} \right) P(\boldsymbol{p}, t), \tag{3.48}$$

where $\mathbf{D}(\boldsymbol{p})$ is the diffusion matrix which consists of the elements $D_{ij}(\boldsymbol{p})$ given by Eq. (3.46). In section 4.6 we solve this equation for a particular choice of the initial conditions. The analysis can be greatly simplified by introducing a transformation of

the coordinates which we discuss in the next section.

3.4 Transformation of coordinates

Because the statistics of the random potential is isotropic and translationally invariant, it is natural to employ the polar coordinate system for the two-dimensional case and the spherical coordinate system for the three-dimensional case. We then expect that in the new coordinate system the off-diagonal elements of the diffusion matrix vanish and the diagonal elements of the matrix depend only on the magnitude of the momentum. In the two-dimensional case we introduce a rectangular coordinate system in which one axis $\hat{e}_p$ coincides with the direction of the momentum and the other axis $\hat{e}_\theta$ is perpendicular to it. The dynamics is therefore described by a set of new variables: p, which is the magnitude of the momentum, and θ, which is the polar angle. The relation between the new and old coordinates is given by

$$\begin{aligned} p_1 &= p\cos\theta, \\ p_2 &= p\sin\theta. \end{aligned} \tag{3.49}$$

We now consider the form of the Fokker-Planck equation (3.48) in the new coordinate system. First, we consider the form of the diffusion matrix which can be obtained using the transformation matrix

$$\mathbf{T} = \begin{pmatrix} \cos\theta & \sin\theta \\ -\sin\theta & \cos\theta \end{pmatrix}, \tag{3.50}$$

so that the diffusion matrix $\mathbf{D}'$ in the new coordinates is $\mathbf{D}' = \mathbf{T}\mathbf{D}\mathbf{T}^T$. This means that the diffusion coefficient $D_p = D'_{11}$ along $\hat{e}_p$ is given by

$$D_p = D_{11}\cos^2\theta + 2D_{12}\sin\theta\cos\theta + D_{22}\sin^2\theta, \tag{3.51}$$

whereas the diffusion coefficient $D_\theta = D'_{22}$ along $\hat{\boldsymbol{e}}_\theta$ is

$$D_\theta = D_{11}\sin^2\theta - 2D_{12}\sin\theta\cos\theta + D_{22}\cos^2\theta. \tag{3.52}$$

The diffusion coefficients in the new coordinate system are obtained by expressing the derivatives of the correlation function in Eq. (3.46). First, we consider a particular case when $\theta = 0$, and therefore $p_1 = p$ and $p_2 = 0$. We have in this case

$$\begin{aligned} D_p &= D_{11}, \\ D_\theta &= D_{22}. \end{aligned} \tag{3.53}$$

The second derivatives of the correlation function can be written in this case as

$$\begin{aligned} \frac{\partial^2}{\partial p_1^2}C(|\boldsymbol{p}|t/m,t) &= \frac{\partial^2}{\partial p^2}C(pt/m,t), \\ \frac{\partial^2}{\partial p_2^2}C(|\boldsymbol{p}|t/m,t) &= \frac{1}{p}\frac{\partial}{\partial p}C(pt/m,t) + \frac{1}{p^2}\frac{\partial^2}{\partial\theta^2}C(pt/m,t). \end{aligned} \tag{3.54}$$

The derivative of the correlation function with respect to θ vanishes, and we obtain

$$\frac{\partial^2}{\partial p_2^2}C(|\boldsymbol{p}|t/m,t) = \frac{1}{p}\frac{\partial}{\partial p}C(pt/m,t). \tag{3.55}$$

From Eqs. (3.46), (3.53) and (3.54) we obtain

$$D_p = -\frac{m^2}{2}\int_{-\infty}^{\infty} dt\; t^{-2}\frac{\partial^2 C}{\partial p^2}(pt/m,t), \tag{3.56}$$

when $\theta = 0$. Due to rotational symmetry of the problem, the same result is obtained for any θ after performing lengthy but elementary calculations. The coefficient D_p is equal to the diffusion coefficient for the one-dimensional problem when the force is the gradient of the potential [see Eq. (3.15)], if the change of variable from t and p to x is performed. If $p \gg p_0$ the leading term is of order p^{-3} and the result is given by

Eq. (3.17). The diffusion coefficient along $\hat{e}_\theta$ is obtained similarly and given by

$$D_\theta = -\frac{m^2}{2p}\int_{-\infty}^{\infty} dt\; t^{-2}\frac{\partial C}{\partial p}(pt/m, t). \tag{3.57}$$

It is equal to the diffusion coefficient for the one-dimensional problem for the generic case of the random force given by Eq. (3.12) with the correlation function $-x^{-1}\partial_x C(x,t)$ (if the change of variable from t and p to x is performed). The leading term in this case is of order p^{-1} and the result is

$$D_\theta = \frac{D_1 p_0}{p}, \quad D_1 = -\frac{m}{2p_0}\int_{-\infty}^{\infty} dx\; x^{-1}\frac{\partial C}{\partial x}(x,0). \tag{3.58}$$

Using Eqs. (3.48), (3.17), (3.58), and standard formulae for expressing divergence and gradient in polar coordinates, the Fokker-Planck equation in the two-dimensional case reads

$$\frac{\partial P}{\partial t} = \frac{1}{p}\frac{\partial}{\partial p}\left(\gamma p^2 + \frac{D_3 p_0^3}{p^2}\frac{\partial}{\partial p}\right)P + \frac{D_1 p_0}{p^3}\frac{\partial^2 P}{\partial \theta^2}. \tag{3.59}$$

We note that the normalization condition should be modified to take into account the transformation of variables. We have

$$\int_0^\infty dp\; pP(p,\theta,t) = 1. \tag{3.60}$$

In the three-dimensional case we similarly use the rectangular coordinate system with the new variables p, θ and ϕ related to the old variables by

$$\begin{aligned} p_1 &= p\sin\theta\cos\phi, \\ p_2 &= p\sin\theta\sin\phi, \\ p_3 &= p\cos\theta, \end{aligned} \tag{3.61}$$

where ϕ is an azimuthal angle in the spherical coordinate system varying from 0 to 2π (θ in this case ranges from 0 to π by convention). In this case there is an additional

diffusion coefficient D_ϕ along the axis $\hat{\boldsymbol{e}}_\phi$. The symmetry of the problem implies that $D_\phi = D_\theta$. The Fokker-Planck equation in the three-dimensional case therefore reads

$$\begin{aligned}\frac{\partial P}{\partial t} &= \frac{1}{p^2}\frac{\partial}{\partial p}\left(\gamma p^3 + \frac{D_3 p_0^3}{p}\frac{\partial}{\partial p}\right)P \\ &+ \frac{D_1 p_0}{p^3}\left[\frac{1}{\sin\theta}\frac{\partial}{\partial\theta}\left(\sin\theta\frac{\partial P}{\partial\theta}\right) + \frac{1}{\sin^2\theta}\frac{\partial^2 P}{\partial\phi^2}\right].\end{aligned} \tag{3.62}$$

The normalization condition for the three-dimensional case is

$$\int_0^\infty dp \int_0^\pi d\theta\; p^2 \sin\theta P(p,\theta,\phi,t) = 1. \tag{3.63}$$

This concludes the derivation of the Fokker-Planck equation, and we shall discuss its solution in section 3.6, but first we consider another model of diffusion, which exhibits similar behaviour of the diffusion coefficients.

3.5 Generalized Chandrasekhar-Rosenbluth model

In this section we consider motion of a particle travelling through an infinite homogeneous population of background particles. We assume that the test particle propagates due to an interaction with the background particles, and the background particles do not interact with each other. As the test particle moves, its interaction with each of the background particles causes small changes of its velocity. When the number of the background particles is very large, the velocity of the test particle changes rapidly and in an unpredictable way, so that its motion can be described by a diffusion process of some type. The test particle could be a star moving in a galaxy interacting with the background stars (the interaction between the background stars is not considered), so that the force of interaction is gravitational and thus proportional to the inverse square of the distance r between stars. In this case, it is found that the test particle experiences a gradual decrease of the velocity in the direction of motion. This phenomenon is called 'dynamical friction' due to Chandrasekhar [21], who studied this problem in the context of motion of stars in galaxies. The formula for the dynamical

friction suggests that for the 'slow' particle (with velocities much smaller than some representative velocity scale) this deceleration is proportional to the velocity of the particle v (analogous to the Stokes's law for a drag force discussed in section 2.3), and for the sufficiently 'fast' particle the deceleration is proportional to v^{-2}. Subsequently, Rosenbluth *et al.* [22] found that the diffusion coefficient in the direction parallel to the direction of motion is proportional to v^{-3}, while the diffusion coefficients in the plane perpendicular to the direction of motion is proportional to v^{-1}. The exact expressions for these coefficients and the drift velocity contain logarithmic terms which are not precisely defined due to the long-range nature of the gravitational interaction. In this section we consider the Chandrasekhar-Rosenbluth model for the case when the interaction is described by a short-range potential $U(r)$ of some rather arbitrary form. We derive the diffusion coefficients for these models precisely in terms of the macroscopic parameters and show that the results for the scaling of the diffusion coefficients are the same as in the generalized Ornstein-Uhlenbeck process. This leads to the same short-time asymptotic behaviour in both models.

We shall only discuss the two-dimensional case for simplicity and proceed as follows. We first calculate the change of the velocity of a test particle due to the encounter with a stationary background particle. We denote components of this change by $\Delta v'_{\parallel}$ and $\Delta v'_{\perp}$, in the directions parallel and perpendicular to the initial velocity of the test particle. Next, we consider the change of the velocity of the test particle for the case when the background particle propagates with velocity $\boldsymbol{v}_b$. We denote components of this change by $\Delta v_{\parallel}$ and $\Delta v_{\perp}$. Using geometrical arguments, we then express $\Delta v_{\perp}$ and $\Delta v_{\parallel}$ in terms of $\Delta v'_{\perp}$ and $\Delta v'_{\parallel}$.

Let us consider a test particle of mass m moving in the horizontal direction with the initial velocity $\boldsymbol{V}_0 = (V_0, 0)$. The test particle interacts with a background particle of mass M, which is initially at rest. After an encounter the test particle propagates with velocity $\boldsymbol{V}_1$ described by its magnitude V_1 and the polar angle ξ_1, and the background particle moves with velocity $\boldsymbol{V}_2$ described by its magnitude V_2 and the polar angle ξ_2 (see Fig. 3.2).

The changes of the velocity of the test particle in the direction parallel and per-

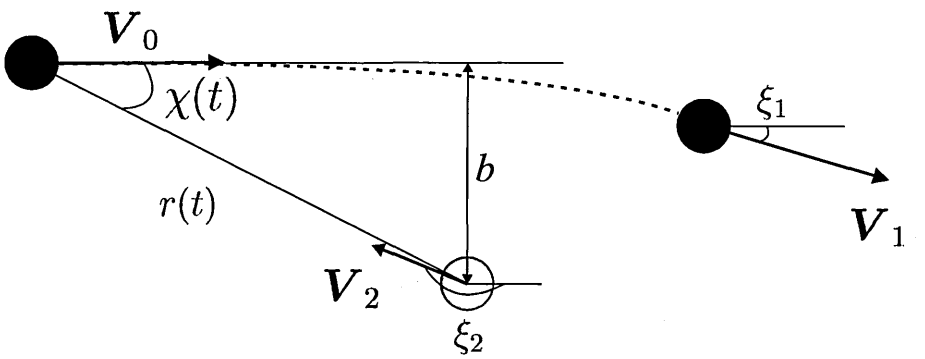

Figure 3.2: The encounter between a test particle (black) and a background particle (red). The interaction causes a small change of the velocity of both particles.

pendicular to $\boldsymbol{V}_0$ are

$$\Delta v'_{\parallel} = V_1 \cos\xi_1 - V_0,$$
$$\Delta v'_{\perp} = V_1 \sin\xi_1. \tag{3.64}$$

The conservation of momentum before and after the encounter yields

$$mV_0 = mV_1 \cos\xi_1 + MV_2 \cos\xi_2,$$
$$0 = mV_1 \sin\xi_1 + MV_2 \sin\xi_2, \tag{3.65}$$

and from the conservation of energy we obtain

$$mV_0^2 = mV_1^2 + MV_2^2. \tag{3.66}$$

This enables us to write the equation for V_1:

$$V_1^2(m+M) - 2mV_0V_1 \cos\xi_1 + V_0^2(m-M) = 0. \tag{3.67}$$

We assume that the encounter induces only a small change of the direction of motion of the test particle, so that ξ_1 can be taken as being small. In this approximation the solution of Eq. (3.67) is

$$V_1 = V_0(1 - \alpha\xi_1^2) + O(\xi_1^4), \tag{3.68}$$

where $\alpha = m/(2M)$. We substitute V_1 from (3.68) into Eq. (3.64) and obtain

$$\Delta v'_{\parallel} \approx -V_0 \beta \xi_1^2,$$
$$\Delta v'_{\perp} \approx V_0 \xi_1, \tag{3.69}$$

where $\beta = \alpha + 1/2 = (m+M)/2M$. In the small-angle approximation ξ_1 is defined by the change of the momentum in the perpendicular direction, so that $\xi_1 \sim \Delta p_{\perp}/(mV_0)$. The change of the momentum $\Delta p_{\perp}$ is determined by the force of interaction between particles separated by distance r with magnitude $f(r) = -dU(r)/dr$, so that $\Delta p_{\perp}$ can be written as

$$\Delta p_{\perp} = -\int_{-\infty}^{\infty} dt \frac{dU}{dr}[r(t)] \sin\chi(t), \tag{3.70}$$

where $r(t)$ is a distance between the particles and $\chi(t)$ is an angle between $\boldsymbol{V}_0$ and the vector connecting the particles. We define an impact b to be the initial distance between the test and background particles along the axis perpendicular to $\boldsymbol{V}_0$. From Fig. 3.2 we find that $r(t) = \sqrt{x(t)^2 + b^2}$ and $\sin\chi(t) = b/\sqrt{x(t)^2 + b^2}$, where $x(t)$ is a coordinate of the test particle along the direction parallel to $\boldsymbol{V}_0$. Changing the variable $x(t) = V_0 t$ we obtain

$$\Delta p_{\perp} \approx -\frac{1}{V_0}\int_{-\infty}^{\infty} dx \, \frac{dU}{dr}(\sqrt{x^2+b^2})\frac{b}{\sqrt{x^2+b^2}}. \tag{3.71}$$

If we denote an integral

$$I(b) = -\int_{-\infty}^{\infty} dx \, \frac{dU}{dr}(\sqrt{x^2+b^2})\frac{b}{\sqrt{b^2+x^2}}, \tag{3.72}$$

we obtain

$$\xi_1(b, V_0) \approx \frac{I(b)}{mV_0^2}. \tag{3.73}$$

Using this relation we find

$$\Delta v'_{\parallel} = -\frac{\beta I^2(b)}{m^2 V_0^3},$$
$$\Delta v'_{\perp} = \frac{I(b)}{m V_0}. \tag{3.74}$$

Thus, the contribution to the change of the velocity of the test particle due to a single encounter is proportional to V_0^{-3} and V_0^{-1} in the directions parallel and perpendicular to $\boldsymbol{V}_0$, respectively. The averaging over collisions with many particles is expected to add another factor of V_0, as the particle propagates with this velocity (see also the derivation below). This suggests that the second moments of the change of the velocity scales as V_0^{-5} and V_0^{-1} in the directions parallel and perpendicular to $\boldsymbol{V}_0$, respectively. While the latter result is consistent with the behaviour of the diffusion coefficient in the generalized Ornstein-Uhlenbeck process, the former result is different, as in the previous model the result is $\langle \Delta v_{\parallel}^2 \rangle \sim v^{-3}$. However, if the background particles are not stationary, the correction of the diffusion coefficients should be considered.

We assume that the background particle moves with velocity $\boldsymbol{v}_b$, in which case the discussion above is valid if $\boldsymbol{V}_0$ is a relative velocity of the test particle in the frame of reference moving with the background particle. The velocity of the test particle in a fixed frame of reference is therefore $\boldsymbol{v}_0 = \boldsymbol{V}_0 + \boldsymbol{v}_b$. We are interested in the changes of the velocity of the test particle in the directions parallel and perpendicular to $\boldsymbol{v}_0$. We denote these $\Delta v_{\parallel}$ and $\Delta v_{\perp}$ and deduce from Fig. 3.3:

$$\begin{aligned} \Delta v_{\parallel} &= \Delta v'_{\parallel} \cos\Omega + \Delta v'_{\perp} \sin\Omega, \\ \Delta v_{\perp} &= \Delta v'_{\perp} \cos\Omega - \Delta v'_{\parallel} \sin\Omega, \end{aligned} \tag{3.75}$$

where Ω is an angle between $\boldsymbol{V}_0$ and $\boldsymbol{v}_0$. These relations are equivalent to the rotation of the coordinate system by angle Ω. Assuming that $v_0 \gg v_b$, where $v_b = |\boldsymbol{v}_b|$ and $v_0 = |\boldsymbol{v}_0|$, we obtain $\Omega \sim v_b/V_0$ and $v_0 \sim V_0$. In this approximation, to the leading

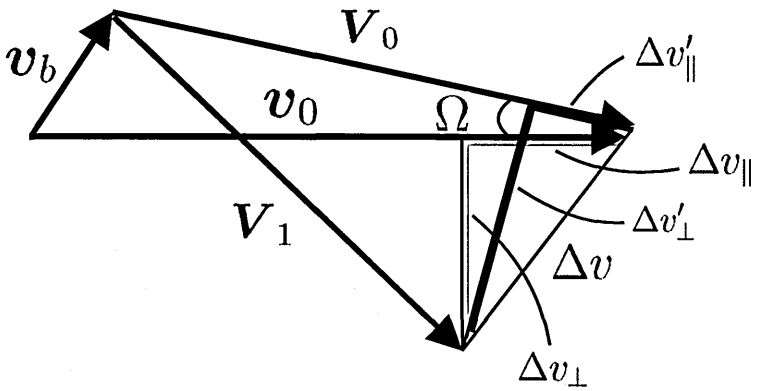

Figure 3.3: Geometrical construction illustrating the changes of the velocity of the test particle Δv parallel and perpendicular to the relative velocity $\boldsymbol{V}_0$ ($\Delta v'_{\parallel}$ and $\Delta v'_{\perp}$, blue solid lines) and the velocity of the test particle $\boldsymbol{v}_0$ ($\Delta v_{\parallel}$ and $\Delta v_{\perp}$, red solid lines).

order in v_0, we have

$$\begin{aligned} \Delta v_{\parallel} &\approx \frac{I(b) v_b}{m v_0^2}, \\ \Delta v_{\perp} &\approx \frac{I(b)}{m v_0}. \end{aligned} \tag{3.76}$$

We now imagine that the test particle is travelling through an infinite homogenous population of the background particles with the spatial density number n (measuring a number of particles per unit area) and the PDF of the velocity $f(\boldsymbol{v}_b)$. The number ΔN of the background particles it encounters with velocities in a range from $\boldsymbol{v}_b$ to $\boldsymbol{v}_b + d^2\boldsymbol{v}_b$ and the impact parameter between b and $b + db$ in time Δt is the number of particles in two thin stripes, each of width db and length equal to the distance travelled by the particle in Δt, and times the probability $f(\boldsymbol{v}_b) d^2\boldsymbol{v}_b$. We have

$$\Delta N \sim 2 n db V_0 \Delta t f(\boldsymbol{v}_b) d^2\boldsymbol{v}_b \tag{3.77}$$

In order to obtain the total contribution of many background particles with different impact parameters and velocities, we integrate over b and $\boldsymbol{v}_b$,

$$\begin{aligned} \frac{\langle \Delta v_{\parallel}^2 \rangle}{2\Delta t} &= \frac{n}{m^2 v_0^3} \int db\, I^2(b) \int d^2\boldsymbol{v}_b f(\boldsymbol{v}_b) |\boldsymbol{v}_b|^2\,, \\ \frac{\langle \Delta v_{\perp}^2 \rangle}{2\Delta t} &= \frac{n}{m^2 v_0} \int db\, I^2(b). \end{aligned} \tag{3.78}$$

The limits of integration over b could be chosen depending on the form of the potential. In the case of the original Chandrasekhar-Rosenbluth model, the maximum impact parameter should be introduced because of the long-range interaction between the particles. If $U(r)$ is a short-range potential, the integral over b should approach a well-defined constant value.

We obtain that the diffusion matrix of the generalized Chandrasekhar-Rosenbluth model has the same scaling as in the original Chandrasekhar-Rosenbluth model. Furthermore, it has the same scaling as in the generalized Ornstein-Uhlenbeck process leading to the same short-time dynamics, which we discuss in the next two sections.

3.6 Probability density function and moments of the momentum

We return to the generalized Ornstein-Uhlenbeck process and obtain the closed-form solution of the Fokker-Planck equation for a particular choice of the initial conditions. We use this solution to obtain an exact expression for the growth of the moments of the momentum.

We first consider the two-dimensional case. We seek the solution of Eq. (3.59) in the form $P(p,\theta,t) = \rho(p,t)\Theta(\theta,t)$. The equation for $\rho(p,t)$ reads

$$\frac{\partial \rho}{\partial t} = \frac{D_3 p_0^3}{p^3}\frac{\partial^2 \rho}{\partial p^2} + \left(\gamma p - \frac{2D_3 p_0^3}{p^4}\right)\frac{\partial \rho}{\partial p} + 2\gamma\rho, \tag{3.79}$$

whereas $\Theta(\theta,t)$ obeys the diffusion equation:

$$\frac{\partial \Theta}{\partial t} = \frac{D_1 p_0}{p^3}\frac{\partial^2 \Theta}{\partial \theta^2}. \tag{3.80}$$

We consider the case when the particle is initially at rest, so that the initial conditions is $P(p,\theta,0) = \delta(p)$. The diffusion coefficient for the growth of the momentum is the same as in the one-dimensional model given by Eq. (3.15), and we expect the same scaling of the momentum as in the one-dimensional model with this diffusion

coefficient. The closed-form solution of Eq. (3.79) can be found using the solution of the one-dimensional model, Eq. (3.31). We find the solution of Eq. (3.79) in the form $\rho(p,t) = P(p,t)F(t)$, where $P(p,t)$ is given by Eq. (3.31) and $F(t)$ is an unknown function. Introducing this into Eq. (3.79) we obtain

$$\frac{\partial P}{\partial t}F + PF' = F\frac{D_3 p_0^3}{p^3}\frac{\partial^2 P}{\partial p^2} + F\left(\gamma p - \frac{2D_3 p_0^3}{p^4}\right)\frac{\partial P}{\partial p} + 2\gamma PF. \tag{3.81}$$

The density $P(p,t)$ satisfies the Fokker-Planck equation for the one-dimensional model which reads

$$\frac{\partial P}{\partial t} = \frac{D_3 p_0^3}{p^3}\frac{\partial^2 P}{\partial p^2} + \left(\gamma p - \frac{3D_3 p_0^3}{p^4}\right)\frac{\partial P}{\partial p} + \gamma P. \tag{3.82}$$

Using this we obtain

$$\frac{PF'}{F} = \gamma P + \frac{D_3 p_0^3}{p^4}\frac{\partial P}{\partial p}. \tag{3.83}$$

In view of Eq. (3.31) we obtain the equation for $F(t)$:

$$\frac{F'}{F} = \frac{\gamma \mathrm{e}^{-5\gamma t}}{\mathrm{e}^{-5\gamma t} - 1}, \tag{3.84}$$

which has a solution $F(t) = (1 - \mathrm{e}^{-5\gamma t})^{-1/5}$. We therefore find the following normalized closed-form solution of (3.79):

$$\begin{aligned}\rho(p,t) &= \frac{5}{\Gamma(2/5)}\frac{\gamma^{2/5}}{[5D_3 p_0^3(1-\mathrm{e}^{-5\gamma t})]^{2/5}} \\ &\times \exp\left[-\frac{\gamma p^5}{5D_3 p_0^3(1-\mathrm{e}^{-5\gamma t})}\right].\end{aligned} \tag{3.85}$$

In the long-time limit the density is non-Maxwellian given by

$$\rho_0(p) = \frac{5\gamma^{2/5}}{\Gamma(2/5)(5D_3 p_0^3)^{2/5}}\exp\left[-\frac{\gamma p^5}{5D_3 p_0^3}\right]. \tag{3.86}$$

Using the probability density (3.85) we determine the l-th moment of p,

$$\begin{aligned}\langle p^l(t)\rangle = \int_0^\infty dp\, p^{l+1}\rho(p,t) &= \left(\frac{5D_3 p_0^3}{\gamma}\right)^{l/5}\frac{\Gamma[(2+l)/5]}{\Gamma(2/5)} \\ &\times (1-\mathrm{e}^{-5\gamma t})^{l/5}.\end{aligned} \tag{3.87}$$

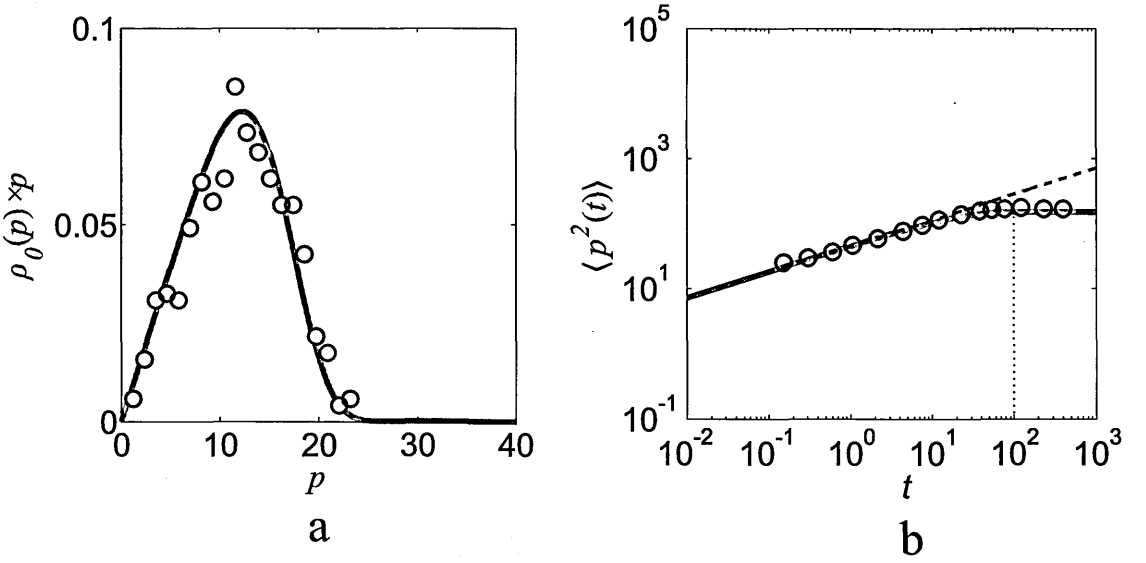

Figure 3.4: Shows results of the numerical simulation of Eq. (3.32) for the motion in the two-dimensional potential force field. Panel **a** shows stationary non-Maxwellian PDF (3.86) (solid line) and data from the numerical simulation (circles). Panel **b** shows the second moment of the momentum (3.87) with $l = 2$ (solid line) and data from the numerical simulation (circles). Dashed line shows the slope $t^{2/5}$ and dotted line indicates time γ^{-1} at which the density becomes stationary. The results are for the Gaussian correlation function of the potential $C(x,t) = \sigma^2 \exp[-x^2/(2\eta^2) - t^2/(2\tau^2)]$ with $\sigma = 15$, $\tau = 0.1$ and $\eta = 0.1$. The other parameters were $m = 1$ and $\gamma = 0.01$.

We remark that an additional factor of p in the expression above appears as a weight of the transformation defined in Eq. (3.49).

In the three-dimensional case we solve Eq. (3.62) by separating variables, so that $P(p,\theta,\phi) = \rho(p,t)\Psi(\theta,\phi,t)$. The solution of the corresponding equation for $\rho(p,t)$ is obtained similarly to the two-dimensional case and we have

$$\begin{aligned} \rho(p,t) &= \frac{5}{\Gamma(3/5)} \frac{\gamma^{3/5}}{[5D_3 p_0^3 (1 - \mathrm{e}^{-5\gamma t})]^{3/5}} \\ &\times \exp\left[-\frac{\gamma p^5}{5D_3 p_0^3 (1 - \mathrm{e}^{-5\gamma t})} \right]. \end{aligned} \tag{3.88}$$

This determines moments of the momentum

$$\begin{aligned} \langle p^l(t) \rangle &= \left(\frac{5D_3 p_0^3}{\gamma} \right)^{l/5} \frac{\Gamma[(3+l)/5]}{\Gamma(3/5)} \\ &\times (1 - \mathrm{e}^{-5\gamma t})^{l/5}. \end{aligned} \tag{3.89}$$

For both two- and three-dimensional cases we obtain that at short times the variance

of the momentum grows as

$$\langle p^2(t)\rangle \sim t^{2/5} \tag{3.90}$$

Thus, at short times the momentum diffuses anomalously with the same exponent as in the one-dimensional model with the diffusion coefficient Eq. (3.17). The results for the stationary probability density and diffusion of the momentum in the two-dimensional case are illustrated in Fig. 3.4.

3.7 Spatial diffusion

In this section we find the mean square value of the displacement of the particle which starts at the origin:

$$\langle |\boldsymbol{x}(t)|^2\rangle = \frac{1}{m^2}\int_0^t dt_1 \int_0^t dt_2\ \langle \boldsymbol{p}(t_1)\cdot\boldsymbol{p}(t_2)\rangle. \tag{3.91}$$

This can be written as

$$\langle |\boldsymbol{x}(t)|^2\rangle = \frac{1}{m^2}\int_0^t dt_1 \int_0^t dt_2\ \langle p(t_1)p(t_2)\cos\theta\rangle, \tag{3.92}$$

where θ is an angle between $\boldsymbol{p}(t_1)$ and $\boldsymbol{p}(t_2)$. We recall that when the force is the gradient of the potential, we have $D_p \ll D_\theta$ for $p \gg p_0$ implying that the correlation of the angle vanishes much more rapidly than the correlation of the magnitude of the momentum. This makes it possible to write the correlation function in (3.92) with a fixed value of the momentum and then average over all possible values using the PDF given by Eqs. (3.85) or (3.88). We have

$$\begin{aligned}\langle p(t_1)p(t_2)\cos\theta\rangle \ &\approx \ \int_0^\infty dp\ J(p,\theta)\rho(p,t_1)p^2(t_1)\\ &\times\ \langle\cos\theta(|t_2-t_1|)\rangle,\end{aligned} \tag{3.93}$$

where $J(p,\theta)$ is the weight of transformation. For comparison we consider the motion of the particles in a two-dimensional solenoidal (incompressible) field

$$\boldsymbol{f} = \left(\frac{\partial\psi}{\partial y}, -\frac{\partial\psi}{\partial x}\right). \tag{3.94}$$

In this case the diffusion matrix $\mathbf{D_s}$ can be written in terms of the elements of the matrix $\mathbf{D}$ for the potential case. Using Eq. (3.44) we obtain:

$$\mathbf{D}_s = \begin{pmatrix} D_{22} & -D_{12} \\ -D_{12} & D_{11} \end{pmatrix}. \tag{3.95}$$

Consequently, in the transformed matrix $\mathbf{D}'_s = \mathbf{T}\mathbf{D}_s\mathbf{T}^T$, the off-diagonal elements vanish, whereas the diagonal elements switches over compared to the potential case, so that the diffusion coefficient corresponding to the magnitude of the momentum scales as p^{-1}, while the diffusion coefficient corresponding to the polar angle scales as p^{-3}. The difference in the dynamics between the potential and solenoidal cases is illustrated in Fig. 3.5. In the potential case the angle of the momentum changes rapidly for $p \gg p_0$, so that the points in a phase-space (p_1, p_2) fill a circle. In the solenoidal case the magnitude of the momentum grows rapidly, so that these points form narrow 'rays'. In the following, we shall only discuss the case of the potential force field.

In the two-dimensional case the probability density of $\theta(|t_2 - t_1|)$ satisfies the diffusion equation (3.80) with the initial condition $\Theta(\theta, 0) = \delta(\theta)$. The solution is Gaussian:

$$\begin{aligned} \Theta(\theta, |t_2 - t_1|) &= \frac{1}{2\sqrt{\pi\mathcal{D}|t_2 - t_1|}} \\ &\times \exp\left(-\frac{\theta^2}{4\mathcal{D}|t_2 - t_1|}\right), \end{aligned} \tag{3.96}$$

where $\mathcal{D} = D_1 p_0 / p^3(t_1)$. Using this probability density we calculate the average

$$\langle \cos\theta(|t_2 - t_1|)\rangle = \exp\left(-\mathcal{D}|t_2 - t_1|\right). \tag{3.97}$$

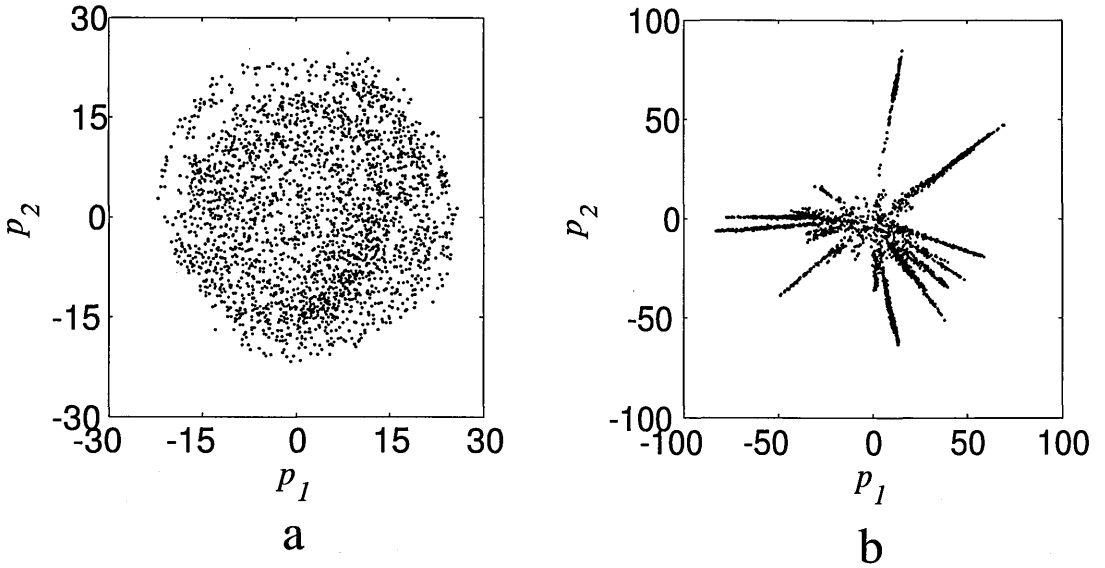

Figure 3.5: Shows the momentum of a single particle at different times from the numerical simulation. Two panels illustrate the difference in the dynamics of the momentum for the motion in the potential (**a**) and solenoidal (**b**) force-fields. In the former case the angle changes rapidly, so that the momentum diffuses on a circle, and in the latter case the magnitude of the momentum grows faster, thus forming narrow 'rays' in the phase-space (p_1, p_2). The parameters of the simulation are the same as in Fig. 3.4.

We thus obtain from Eqs. (3.92) and (3.93)

$$\begin{aligned}\langle|\boldsymbol{x}(t)|^2\rangle &\approx \frac{1}{m^2}\int_0^t dt_1 \int_0^t dt_2 \int_0^\infty dp\ \rho(p,t_1)p^3(t_1) \\ &\times \exp\left(-\mathcal{D}|t_2-t_1|\right). \end{aligned} \tag{3.98}$$

Introducing a new variable $T = t_1 - t_2$ we have

$$\begin{aligned}\langle|\boldsymbol{x}(t)|^2\rangle &\approx \frac{2}{m^2}\int_0^t dt_1 \int_0^t dT \int_0^\infty dp\ \rho(p,t_1)p^3(t_1)\exp\left(-\frac{D_1 p_0}{p^3(t_1)}T\right) \\ &= \frac{2}{m^2 D_1 p_0}\int_0^t dt_1 \int_0^\infty dp\ \rho(p,t_1)p^6(t_1)\left[1-\exp\left(-\frac{D_1 p_0}{p^3(t_1)}t\right)\right]. \end{aligned} \tag{3.99}$$

When the forcing is strong we have $\frac{D_1 p_0}{p^3}t \gg 1$ for $t \gg \tau$, and therefore

$$\begin{aligned}\langle|\boldsymbol{x}(t)|^2\rangle &= \frac{2}{m^2 D_1 p_0}\int_0^t dt_1 \int_0^\infty dp\ \rho(p,t_1)p^6(t_1) \\ &= \frac{2}{m^2 D_1 p_0}\int_0^t dt_1 \langle p^5(t_1)\rangle. \end{aligned} \tag{3.100}$$

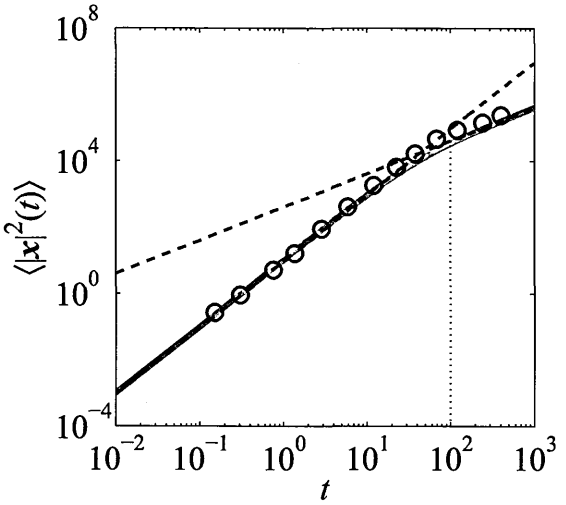

Figure 3.6: Shows results for the spatial diffusion in the two-dimensional potential force-field. The results from the numerical simulation (circles) are compared with Eq. (3.101) (solid line). Dashed lines show the slopes t^2 and t and dotted line indicates the time γ^{-1}. The parameters of the simulation are the same as in Fig. 3.4.

Using Eq. (3.87) we obtain

$$\langle|\boldsymbol{x}(t)|^2\rangle = \frac{4D_3p_0^2}{5D_1m^2\gamma^2}(5\gamma t + \mathrm{e}^{-5\gamma t} - 1). \tag{3.101}$$

In the three-dimensional case the probability density of θ can be found by considering (3.62). The separation of the variables gives the equation

$$\frac{p^3}{D_1p_0}\frac{\partial\Psi}{\partial t} = \frac{1}{\sin\theta}\frac{\partial}{\partial\theta}\left(\sin\theta\frac{\partial\Psi}{\partial\theta}\right) + \frac{1}{\sin^2\theta}\frac{\partial^2\Psi}{\partial\phi^2}. \tag{3.102}$$

with the initial conditions $\Psi(\theta,\phi,0) = \delta(\theta)$ independent from ϕ. This is a form of the Poisson's equation in spherical coordinates. We seek a particular solution in the form of $\Psi(\theta,\phi,t) = \Theta(\theta)\Phi(\phi)T(t)$. We substitute this into Eq. (3.102) and obtain,

$$\frac{\Theta'\cos\theta}{\Theta\sin\theta} + \frac{\Theta''}{\Theta} + \frac{\Phi''}{\Phi\sin^2\theta} = \frac{p^3}{p_0D_1}\frac{T'}{T} = -\lambda, \tag{3.103}$$

where λ is a parameter. This gives the equation for T:

$$T' + \frac{\lambda p_0D_1}{p^3}T = 0, \tag{3.104}$$

with the solution

$$T(t) = C_\lambda \exp\left[-\frac{\lambda p_0 D_1}{p^3} t\right], \tag{3.105}$$

where C_λ is a constant. If we multiply Eq. (3.103) by $\sin^2\theta$ we obtain

$$\frac{\Theta' \sin\theta\cos\theta}{\Theta} + \frac{\Theta'' \sin^2\theta}{\Theta} + \lambda \sin^2\theta = -\frac{\Phi''}{\Phi} = \mu, \tag{3.106}$$

with another parameter μ. The equation for Φ is therefore

$$\Phi'' + \mu\Phi = 0, \tag{3.107}$$

We have the solution which depends on the sign of μ. Below, we shall show that μ is a non-negative integer, so that the solution is $\Phi(\phi) = U_m \cos\sqrt{\mu}\phi + V_m \sin\sqrt{\mu}\phi$, where U_m and V_m are constants. The equation for Θ, in turn, reads

$$\sin^2\theta\Theta'' + \sin\theta\cos\theta\Theta' + \Theta[\lambda \sin^2\theta - \mu] = 0. \tag{3.108}$$

By changing the variable $z = \cos\theta$ we obtain

$$(1 - z^2)\Theta'' - 2z\Theta' + \Theta\left[\lambda - \frac{\mu}{1 - z^2}\right] = 0. \tag{3.109}$$

This is the general Legendre equation with the solution given in terms of associated Legendre polynomials [52]. We seek a continuous solution for $-1 \leq z \leq 1$. This is possible only when $\lambda = l(l+1)$ and $\mu = m^2$, where $l \geq 0$ and m are integers with $|m| \leq l$. The solution is then given by $\Theta_{lm} = A_{lm} P_l^m(z) + B_{lm} Q_l^m(z)$, where $P_l^m(z)$ and $Q_l^m(z)$ are associated Legendre polynomials of first and second kind, respectively, and A_{lm} and B_{lm} are constants. Furthermore, $Q_l^m(z)$ has a singularity at $z = \pm 1$, and we therefore put $B_{lm} = 0$ and write the solution as $\Theta_{lm} = A_{lm} P_l^m(z)$. The solution of (3.103) can be written as a linear combination of the solutions corresponding to

different values of l and m,

$$\Psi(\theta,\phi,t)=\sum_{l=0}^{\infty}\sum_{m=0}^{l}\exp\left[-\frac{l(l+1)p_0D_0}{p^3}t\right]P_l^m(\cos\theta)(U_m\cos m\phi+V_m\sin m\phi). \tag{3.110}$$

The problem has a rotational symmetry, so that the solution is independent of ϕ,

$$\Psi(\theta,\phi,t)=\sum_{l=0}^{\infty}A_l\exp\left[-\frac{l(l+1)p_0D_0}{p^3}t\right]P_l(\cos\theta), \tag{3.111}$$

where $P_l(z)$ is a Legendre polynomial of degree l. In terms of $z=\cos\theta$ this reads

$$\Psi(z,\phi,t)=\sum_{l=0}^{\infty}A_l\exp\left[-\frac{l(l+1)p_0D_0}{p^3}t\right]P_l(z). \tag{3.112}$$

Using the property of orthogonality $\int_{-1}^{1}P_m(z)P_n(z)dz=2\delta_{mn}/(2n+1)$, in view of the initial conditions $\Psi(z,\phi,0)=\delta(z-1)$, we obtain $A_l=(2l+1)/2$ and the solution is then

$$\Psi(\theta,\phi,t)=\sum_{l=0}^{\infty}\frac{2l+1}{2}\exp\left[-l(l+1)\mathcal{D}t\right]P_l(\cos\theta). \tag{3.113}$$

Here $\mathcal{D}=p_0D_0/p^3$ is the same as in the two-dimensional case. Using this density we calculate the average,

$$\langle\cos\theta(|t_2-t_1|)\rangle=\exp\left(-3\mathcal{D}|t_2-t_1|\right), \tag{3.114}$$

and from (3.92) and (3.93) we obtain

$$\begin{aligned}\langle|\boldsymbol{x}(t)|^2\rangle &\sim \frac{1}{m^2}\int_0^t dt_1\int_0^t dt_2\int_0^\infty dp\;\rho(p,t_1)p^3(t_1)\\ &\times\ \exp\left(-3\mathcal{D}|t_2-t_1|\right).\end{aligned} \tag{3.115}$$

The evaluation of the integral using the probability density (3.88) yields

$$\langle|\boldsymbol{x}(t)|^2\rangle=\frac{2D_3p_0^2}{5D_1m^2\gamma^2}(5\gamma t+\mathrm{e}^{-5\gamma t}-1). \tag{3.116}$$

We find that in two- and three-dimensional cases $\langle|\boldsymbol{x}(t)|^2\rangle\sim t^2$ at short times, so

that the particle diffuses ballistically. The results are consistent with a short-time asymptotic behaviour of the undamped particle obtained in [51] for $d > 1$. The long-time behaviour is naturally diffusive, $\langle |\boldsymbol{x}(t)|^2 \rangle \sim t$. In Fig. 3.6 we show the comparison of the analytical and numerical results for $\langle |\boldsymbol{x}(t)|^2 \rangle$ for the case of motion in the two-dimensional potential force field, illustrating the short-time ballistic diffusion.

3.8 Summary

In this chapter we have studied generalizations of two classical models for diffusion of a particle accelerated by random forces. We have discussed a generalization of the classical Ornstein-Uhlenbeck process by considering the force which depends on the position of the particle, as well as time. We have also modified the Chandrasekhar-Rosenbluth model by considering motion due to a short-range interaction potential. Although both models are described by different microscopic equations of motion, surprisingly, they have the same scaling of the diffusion coefficients, leading to the same short-time asymptotic dynamics. We have shown that this dynamics is characterized by anomalous diffusion of the momentum, with the variance which scales as $\langle p^2 \rangle \sim t^{2/5}$. At long time, the distribution of the momentum has been found to be non-Maxwellian. The second moment of the displacement grows ballistically at short times, and at long time a simple diffusive behaviour of the displacement has been recovered.

Chapter 4

Generalized Kramers model

This chapter contains material from the paper of the same title written by the author of the thesis (unpublished, in preparation).

4.1 Introduction

In the previous chapter we have studied the model which extends the classical diffusion process, the Ornstein-Uhlenbeck process, to the case when the driving random force depends upon the position of the particle, as well as time. We have seen that this natural generalization results in a number of peculiar features of the model. In this chapter we discuss a similar extension of another classical diffusion process, the Kramers model [23], which describes an overdamped particle in an external potential subjected to random fluctuations. Similarly to the generalized Ornstein-Uhlenbeck process, we expect that in this case the addition of spatial dependence, as well as temporal dependence of the random force would lead to the modification of the diffusion coefficient compared with the classical Kramers model.

In the classical one-dimensional Kramers model, an overdamped particle at position $x(t)$ is driven by the random time-dependent noise $f(t)$ and the external force generated by a potential $U(x)$. We generalize the Kramers model by considering the random noise which depends not only on time, but also on the position of the particle. The equation of motion is therefore similar to the advective dynamics described by

Eq. (2.39) supplemented with an additional potential force:

$$\kappa\dot{x} = -\frac{dU(x)}{dx} + f(x,t), \tag{4.1}$$

where κ is the friction coefficient. The classical Kramers model has a number of important applications in physics and chemistry, and below we briefly discuss two of them.

First example is a model of chemical reaction processes, where the position of the particle represents the reaction coordinate, which undergoes a noise-activated escape process driven by thermal fluctuations [53]. The reaction coordinate is a rather abstract notion in chemistry characterizing the state of a chemical reaction. Typically, the coordinate wiggles around one of the minima of the potential energy profile, until a sequence of random 'kicks' induced by thermal fluctuations transports it over the potential barrier, so that its dynamics can be accurately described by the motion of the Brownian particle in the external potential. An event when the particle overcomes the barrier and escapes the minimum corresponds to an advance of the chemical reaction. It is usually the primary task to calculate the rate at the reaction proceeds. The famous Arrhenius law states that the dependence of this rate R upon the temperature T is given by

$$R \sim \mathrm{e}^{-\frac{E_a}{k_B T}}, \tag{4.2}$$

where E_a is the activation energy and k_B is the Boltzmann constant.

The other important application of the Kramers model concerns the concept of the Brownian ratchet, which was originally introduced by Feynman [24] to illustrate laws of thermodynamics. In its simplest form, the device consists of a ratchet, which resembles a circular saw with asymmetric teeth, rotating freely in one particular (forward) direction. A pawl is attached to the ratchet, thus preventing it to rotate in the other (backward) direction. The ratchet is connected to a paddle wheel by a massless frictionless rod, and the whole mechanism is immersed in a thermal bath at a given temperature. It is assumed that the mechanism is so small that the paddle wheel can rotate in response to collisions with the molecules of the thermal bath, thus rotating

back and forth. The analogy with the model of the Brownian particle in the potential is evident. If the position of the particle represents the angle of rotation of the rod, then the dynamics is periodic and can be split up into two part: random fluctuations induced by collisions of the paddle wheel with the molecules and motion in the potential representing the interaction between the pawl and teeth of the ratchet. The potential in this case is periodic and asymmetric (the so-called 'sawtooth' potential), so that it is expected that the particle tends to travel in the forward direction.

Because the pawl permits the rotation only in one direction, it is expected that the ratchet slowly spins forward as the molecules hit the paddle-wheel. If a weight is attached to the rod connecting the ratchet and the paddle wheel, it would be lifted by this forward rotation making the device 'perpetuum mobile' of the second kind. The contradiction is resolved by noting that the device must be very small in order to react to individual collisions with the molecules. This means that the pawl itself must be influenced by the collisions, so that every now and then it would be lifted and fail to prevent the backward rotation. Since both the paddle wheel and the ratchet are immersed in the same thermal bath, the probability for the pawl to fail is equal to the probability for the ratchet to rotate forward, so that no net work can be extracted. Correspondingly, no net transport (probability flux) of the Brownian particles moving in a periodic and asymmetric potential is observed. The cases where the transport can be introduced by different mechanisms are of great interest. Feynman considered the case where the ratchet and the paddle-wheel are immersed in separate thermal baths at different temperatures. In this case, the transport is induced by the gradient of the temperature. The transport in the Kramers model may also be induced by an addition of another driving force that can be constant [54] or a function of time [55].

In many case it suffices to know the probability density function (PDF) of the position of the particle in order to understand all important properties of the Kramers model. The main result of this chapter is the PDF of the position of the particle moving according to Eq. (4.1) in the limit of short correlation time of the random force. In the following we shall only discuss the motion in one spatial dimension.

The chapter is organized as follows. First, we briefly discuss the classical Kramers

model in section 4.2. In section 4.3 we consider the generalized model given by Eq. (4.1) and derive the Fokker-Planck equation for the PDF of the position of the particle. The stationary solution of the Fokker-Planck equation can be simplified in two asymptotic limits corresponding to very large and very small values of the external force. These two cases are discussed in section 4.4 and section 4.5, respectively. We show how the PDF is obtained for two different types of the potential: symmetric double-well potential and periodic potential with a broken reflection symmetry. The generalized model in the weak forcing limit was first analyzed in [25], where the PDF was found to be equivalent to a reduction of the potential compared with the classical Kramers model. Here, we use a more transparent analysis, giving rise to many additional results. We perform the numerical simulations suggesting that the correct result in the weak forcing limit is the increase of the potential, rather than the decrease obtained in [25]. We present brief arguments justifying this result. In the strong forcing limit we find the solution that corresponds to a non-zero probability flux in the case of the motion in a periodic potential with a broken reflection symmetry.

4.2 Classical Kramers model

Before we proceed to the discussion of the generalized model, we briefly discuss the original Kramers model. This describes an overdamped particle at position $x(t)$ in the external potential $U(x)$ driven by the random time-dependent force $f(t)$. The equation of motion therefore reads

$$\kappa\dot{x} = -\frac{dU(x)}{dx} + f(t). \tag{4.3}$$

The random force $f(t)$ in Eq. (4.3) is assumed to be a stationary Gaussian process with zero mean and the correlation function

$$\langle f(t)f(t')\rangle = C(t-t'). \tag{4.4}$$

The noise is characterized by its typical magnitude σ and correlation time τ. The correlation time is assumed to be small compared with any other time-scales in the problem. Similarly to the Ornstein-Uhlenbeck process, the motion of the particle in this case can be seen as a sequence of independent random displacements. In the absence of the external potential the particle is not bounded and diffuses, so that the mean square displacement at time $t \gg \tau$ is given by $\langle [x(t) - x(0)]^2 \rangle \sim 2D_x t$ with a diffusion constant $D_x \sim \sigma^2 \tau / \kappa^2$. Relaxation towards a statistically stationary state is associated with the action of the potential, and the corresponding relaxation time τ_U can be deduced from dimensional arguments. If U_0 is a typical magnitude of the potential and L is its length scale, then $\tau_U \sim L^2 \kappa / U_0$. The actual value of the relaxation time depends on the form of the potential and can be determined from numerical simulations.

It is convenient to consider the model in the dimensionless variables. We set $t = t' \tau_U$, $x(t) = x'(t')L$, $U(x) = U'(x')U_0$, $f(t) = f'(t')U_0 L^{-1}$ and $C(t) = C'(t')U_0^2 L^{-2}$. Substituting this into Eq. (4.3) and dropping primes in notations of the variables we obtain

$$\frac{dx}{dt} = -\frac{dU(x)}{dx} + f(t). \tag{4.5}$$

In the dimensionless model the time scale of relaxation is unity, and the correlation time of the force is $\omega = \tau / \tau_U$. If the correlation time is sufficiently short ($\omega \ll 1$), the small displacement of the particle in a short time interval δt (such that $\omega \ll \delta t \ll 1$) can be written by integrating Eq. (4.5):

$$\delta x \equiv x(t_0 + \delta t) - x(t_0) = -U'(x)\delta t + \delta w, \tag{4.6}$$

where

$$\delta w = \int_{t_0}^{t_0 + \delta t} dt \; f(t). \tag{4.7}$$

Here, it is assumed that the potential varies slowly on the length-scale of the distance travelled by the particle in δt due to the random noise, so that the argument in $U'(x)$ is kept fixed.

The Kramers model with the short-correlated random force can be analyzed using the Fokker-Planck equation (2.63) for the probability density $P(x,t)$, which we repeat for the convenience:

$$\frac{\partial P(x,t)}{\partial t} = -\frac{\partial}{\partial x}[v_d(x)P(x,t)] + \frac{\partial^2}{\partial x^2}[D(x)P(x,t)]. \tag{4.8}$$

We now derive the drift velocity $v_d(x)$ and the diffusion coefficient $D(x)$ using Eq. (4.6). Because the noise is assumed to be stationary, without loss of generality, we can set $t_0 = 0$ in Eqs. (4.6) and (4.7) for calculating the statistical properties of δw and δx. We first consider the drift velocity $v_d(x) = -U'(x) + \langle \delta w \rangle / \delta t$. Because the random force has zero mean, it follows that $v_d(x) = -U'(x)$.

For the diffusion coefficient we note that $\langle \delta x^2 \rangle = \langle \delta w^2 \rangle + O(\delta t^2)$, where $\langle \delta w^2 \rangle$ is given by

$$\begin{aligned} \langle \delta w^2 \rangle &= \int_0^{\delta t} dt_1 \int_0^{\delta t} dt_2 \, \langle f(t_1) f(t_2) \rangle \\ &= \delta t \int_{-\delta t}^{\delta t} dt \, C(t). \end{aligned} \tag{4.9}$$

We note that $C(t)$ decays rapidly as t increases, so that the integral over the correlation function approaches a constant value for $\delta t \gg \tau$. We have therefore:

$$\langle \delta w^2 \rangle = 2D\delta t, \tag{4.10}$$

where

$$D = \frac{1}{2} \int_{-\infty}^{\infty} dt \, C(t) \tag{4.11}$$

is the diffusion constant.

We are interested in the stationary solution of the Fokker-Planck equation satisfying $\partial_t P(x,t) = 0$. It is found by solving the following differential equation:

$$-v_d(x)P_0(x) + \frac{\partial}{\partial x}[D(x)P_0(x)] = -J_0, \tag{4.12}$$

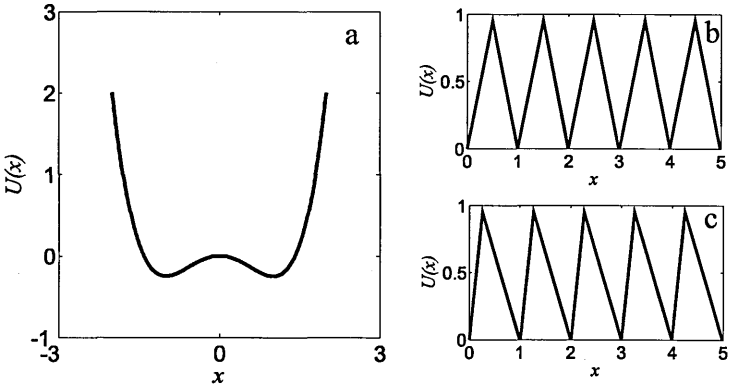

Figure 4.1: Shows three examples of the external potential: symmetric double-well potential (**a**), periodic linear piece-wise potential (**b**), periodic linear piece-wise potential with a broken reflection symmetry (**c**).

where the stationary flux J_0 is determined by the boundary conditions. The solution of Eq. (4.12) with the drift velocity $-U'(x)$ and the diffusion constant D can be readily written as

$$P_0(x) = N\mathrm{e}^{-\frac{U(x)}{D}} - \frac{J_0}{D}\int_{-\infty}^{x} dx_1\, \mathrm{e}^{\frac{U(x_1)-U(x)}{D}}, \tag{4.13}$$

where N is the normalization constant.

We now concentrate on the form of the solution (4.13) for particular choices of the potential illustrated in Fig. 4.1. First example is a symmetric double-well potential, used in modelling a two-way chemical reaction, and the other is a periodic potential. For the double-well potential illustrated in Fig. 4.1**a** the natural boundary conditions are applied [56]:

$$P(\infty) = P(-\infty) = 0. \tag{4.14}$$

Such a potential does not allow the particles to escape to infinity, so that we expect that the probability flux J_0 vanishes. We note that the first term in Eq. (4.13) goes to zero for very large x for the potential shown in Fig. 4.1**a**, and the second term in Eq. (4.13) approaches a non-zero constant, so that the boundary conditions are satisfied only if $J_0 = 0$. Thus, the solution in this case is given by

$$P_0(x) = N\exp\left[-\frac{U(x)}{D}\right], \tag{4.15}$$

For the periodic potential with period L, if we require that $P_0(x)$ is bounded for

very large x, it follows that $P_0(x)$ is periodic [56]. In the dimensionless units the condition of periodicity reads $P_0(x+1) = P_0(x)$. We use $U(x+1) = U(x)$ to write

$$P_0(x+1) = P_0(x) - \frac{J_0}{D}\int_x^{x+1} dx_1 \, \mathrm{e}^{\frac{U(x_1)-U(x)}{D}} \tag{4.16}$$

The integral in the last term is non-zero, therefore we again put $J_0 = 0$ to satisfy the boundary conditions, and the solution in this case is again given by Eq. (4.15). The important consequence of this result is that $J_0 = 0$ regardless of the shape of the periodic potential. In the studies of Brownian ratchets it is often assumed that the periodic potential has an asymmetric form (such as the sawtooth potential illustrated in Fig. 4.1**c**), so that the particles are expected to favour one of the slope to escape the potential minimum. The result shows, however, that the probability flux vanishes, which agrees with the discussion of the Brownian ratchet in section 4.1. We remark that in the case of a periodic potential $P_0(x)$ is normalized in the periodicity interval.

4.3 Fokker-Planck equation for the generalized Kramers model

We now turn to considering the generalized model described by Eq. (4.1), where the force depends upon the position of the particle, as well as time. The random force $f(x,t)$ is assumed to be a stationary and, in addition, translationally invariant Gaussian process with the statistics

$$\begin{aligned} \langle f(x,t)\rangle &= 0, \\ \langle f(x,t)f(x',t')\rangle &= C(x-x',t-t'). \end{aligned} \tag{4.17}$$

The noise is characterized by its typical magnitude σ, correlation length η and correlation time τ. We also assume that the correlation function is smooth and sufficiently differentiable.

We first re-introduce dimensionless variables taking into account the spatial depen-

dence of the noise: $t = t'\tau_U$, $x(t) = x'(t')L$, $U(x) = U'(x')U_0$, $f(x,t) = f'(x',t')U_0L^{-1}$ and $C(x,t) = C'(x',t')U_0^2L^{-2}$. The equation of motion in these dimensionless variables reads (dropping primes in the notation of the variables)

$$\frac{dx}{dt} = -\frac{dU(x)}{dx} + f(x,t). \tag{4.18}$$

We note that in the dimensionless model the correlation length is $l = \eta/L$. The corresponding equation for δx is given by analogy with the classical Kramers model:

$$\delta x = -U'(x)\delta t + \delta w, \tag{4.19}$$

where

$$\delta w = \int_{t_0}^{t_0+\delta t} dt_1 \; f[x(t_1), t_1]. \tag{4.20}$$

We now consider the coefficients of the Fokker-Planck equation, which can be derived from Eq. (4.19) taking into account the spatial dependence of the noise. Using stationary and translationally invariant properties of the noise, we set $t_0 = 0$ and $x(t_0) = 0$ in Eqs. (4.19) and (4.20) and consider the drift velocity $v_d(x) = -U'(x) + \langle \delta w \rangle / \delta t$. We remark that $\langle \delta w \rangle$ does not simply vanish in this case. If we denote $s_x(t) = -U'(x)t$, then $\langle \delta w \rangle$ is given by

$$\begin{aligned} \langle \delta w \rangle &= \int_0^{\delta t} dt \left\langle f\left[s_x(t) + \int_0^t dt_1 \; f[s_x(t_1), t_1], t \right] \right\rangle + O(\delta t^2) \\ &\approx \int_0^{\delta t} dt \; \langle f[s_x(t), t] \rangle \\ &+ \int_0^{\delta t} dt \int_0^t dt_1 \left\langle \frac{\partial f}{\partial x}[s_x(t), t] \; f[s_x(t_1), t_1] \right\rangle . \end{aligned} \tag{4.21}$$

The first term vanishes, and for the second term we use $\langle \partial_x f(x,t) f(0,0) \rangle = \partial_x C(x,t)$ and obtain

$$\begin{aligned} \langle \delta w \rangle &\approx \int_0^{\delta t} dt \int_0^t dt_1 \; \frac{\partial C}{\partial x}[s_x(t - t_1), t - t_1] \\ &= \delta t \int_0^{\infty} dt \; \frac{\partial C}{\partial x}[s_x(t), t]. \end{aligned} \tag{4.22}$$

We conclude that the drift velocity is given by

$$v_d(x) = -U'(x) + \int_0^\infty dt\, \frac{\partial C}{\partial x}[s_x(t), t]. \tag{4.23}$$

For the diffusion coefficient we write $\langle \delta w^2 \rangle$ as

$$\begin{aligned} \langle \delta w^2 \rangle &= \int_0^{\delta t} dt_1 \int_0^{\delta t} dt_2\, \langle f[s_x(t_1), t_1]\, f[s_x(t_2), t_2] \rangle + O(\delta t^2) \\ &\approx \delta t \int_{-\infty}^{\infty} dt\, C[s_x(t), t]. \end{aligned} \tag{4.24}$$

We conclude that $\langle \delta x^2 \rangle \approx \langle \delta w^2 \rangle \approx 2D(x)\delta t$, where

$$D(x) = \frac{1}{2} \int_{-\infty}^{\infty} dt\, C[s_x(t), t]. \tag{4.25}$$

Similarly to the generalized Ornstein-Uhlenbeck process, we find that the diffusion coefficient in the generalized Kramers model depends upon the dynamical variable, in this case the position of the particle. In the generalized Ornstein-Uhlenbeck model we recover the classical diffusion process when the typical distance travelled by the particle in one correlation time due to the random force is negligible compared to the correlation length of the force. In the generalized Kramers model, the diffusion constant for the classical process is recovered if the displacement of the particle due to the potential forcing is small compared to the correlation length of the random noise. When this displacement is large, similarly to the generalized Ornstein-Uhlenbeck model, the diffusion coefficient is expected to decrease.

The solution of the stationary Fokker-Planck equation (4.12) with the drift velocity and the diffusion coefficient given by Eqs. (4.23) and (4.25) is

$$P_0(x) = Z(x) \left[N - J_0 \int_{-\infty}^{x} dy\, D^{-1}(y) Z^{-1}(y) \right], \tag{4.26}$$

where

$$Z(x) = \exp\left[\int_{-\infty}^{x} dy \frac{v_d(y) - D'(y)}{D(y)} \right] \tag{4.27}$$

and N is the normalization constant. In the next two sections we are concerned with simplifying the solution (4.26) in two asymptotic limits corresponding to very large and very small absolute values of the external force $U'(x)$.

4.4 Weak forcing limit

Here we shall briefly describe how the limit of weak forcing was analyzed in [25]. We shall argue that the overall result for the probability density is incorrect, and the formula for the diffusion coefficient (4.25) cannot be used in this case. Our discussion and the results in the next section remain valid.

Let us write the diffusion coefficient by expanding the correlation function in Eq. (4.25) around $x = 0$:

$$D(x) = \frac{1}{2}\int_{-\infty}^{\infty} dt\; C(0,t) + O[U'(x)], \tag{4.28}$$

i.e. the diffusion coefficient can be approximated by a constant in the regions where the external force is so small, that the displacement of the particle in one correlation time due to the external forcing is negligible compared with the correlation length of the random force. We can estimate the ratio between successive terms in the expansion. Each term adds another derivative of the correlation function with respect to x producing a factor of l^{-1}, and another factor of t in the integral producing a factor of ω in the result. We deduce that the ratio is of order $U'(x)\omega/l$. For the drift velocity given by Eq. (4.23) we obtain

$$\begin{aligned} v_d(x) &= -U'(x) + \int_0^{\infty} dt\; \frac{\partial C}{\partial x}(0,t) \\ &- U'(x)\int_0^{\infty} dt\; t\frac{\partial^2 C}{\partial x^2}(0,t) + O[U'(x)]^2 \end{aligned} \tag{4.29}$$

with the leading term of order $U'(x)$. The correlation function is an even function of

its arguments, so that the second term vanishes, and we obtain

$$v_d(x) \approx -U'(x)(1-\xi), \tag{4.30}$$

where

$$\xi = -\int_0^\infty dt\ t\ \frac{\partial^2 C}{\partial x^2}(0,t). \tag{4.31}$$

The sign of ξ can be deduced as follows. If we can write the correlation function in the from of $C(x,t) = C_x(x)C_t(t)$ with $C_t(t) > 0$, then the sign of ξ is determined by the sign of $C_x''(0)$. If the random force de-correlates as x increases, then $x = 0$ is a local maximum of $C(x)$. Provided that the second derivative exists, it follows that $C_x''(0) < 0$ and $\xi > 0$, corresponding to the reduction of the drift velocity.

The solution (4.26) in the weak forcing limit can be thus simplified to

$$P_0(x) = Y(x)\left[N - \frac{J_0}{D_0}\int_{-\infty}^{x} dy\ Y^{-1}(y)\right], \tag{4.32}$$

where

$$Y(x) = \exp\left[-\frac{U(x)(1-\xi)}{D_0}\right], \tag{4.33}$$

and

$$D_0 = \frac{1}{2}\int_{-\infty}^{\infty} dt\ C(0,t). \tag{4.34}$$

We now consider two examples of the external potential similarly to the discussion in section 4.2: periodic potential and symmetric double-well potential. For the double-well potential we again expect that $J_0 = 0$. To prove that, we note that $Y(x)$ vanishes for very large x, and the second term in the brackets multiplied by $Y(x)$ approaches a non-zero constant. Thus, the boundary conditions are satisfied only when $J_0 = 0$. For the periodic potential, we use $U(x+1) = U(x)$ to write

$$P_0(x+1) = P_0(x) + \frac{J_0}{D_0}\int_x^{x+1} dy\ Y(x)Y^{-1}(y). \tag{4.35}$$

The integral in the last term is non-zero, and we again put $J_0 = 0$ to satisfy the

boundary conditions. We conclude that in both examples the solution in the weak external forcing limit is given by

$$P_0(x) = N\exp\left[-\frac{U(x)(1-\xi)}{D_0}\right]. \tag{4.36}$$

This result seems to suggest that the potential is reduced due to spatial correlations of the random force. In section 4.6 we present the results of the numerical simulations which clearly contradict this statement. We give brief arguments which may resolve this contradiction.

4.5 Strong forcing limit

The other asymptotic limit we consider corresponds to large absolute values of the external force. In this case the distance travelled by the particle in one correlation time due to the external force is much larger than the correlation length of the random force. We write the diffusion coefficient (4.25) by integrating over a new variable $z = -U'(x)t$ and expanding the correlation function in series around $t = 0$:

$$D(x) = \frac{1}{2|U'(x)|}\int_{-\infty}^{\infty} dz\; C(z,0) + O\left[U'(x)\right]^{-2}. \tag{4.37}$$

Using the result obtained in the previous section, the ratio between successive terms is $l/[U'(x)\omega]$, which is small in the regions where $U'(x)$ is sufficiently large. As expected, the diffusion coefficient decreases as $|U'(x)|$ increases:

$$D(x) = \frac{D_\infty}{|U'(x)|}, \quad D_\infty = \frac{1}{2}\int_{-\infty}^{\infty} dz\; C(z,0). \tag{4.38}$$

Similarly, we obtain the drift velocity from Eq. (4.23):

$$v_d(x) = -U'(x) + O[U'(x)]^{-1}. \tag{4.39}$$

Substituting (4.38) and (4.39) into (4.26) we obtain the solution in the strong external forcing limit:

$$P_0(x) = |U'(x)|\mathrm{e}^{-I(x)}\left[N - \frac{J_0}{D_\infty}\int_{-\infty}^{x} dy\ \mathrm{e}^{I(y)}\right], \tag{4.40}$$

where

$$I(x) = \frac{1}{D_\infty}\int_{-\infty}^{x} dy\ |U'(y)|U'(y). \tag{4.41}$$

For the symmetric double-well potential satisfying the natural boundary conditions, we can again show that $J_0 = 0$. We note that $I(x)$ diverges for large x, whereas the integral term in the brackets multiplied by $\exp[-I(x)]$ converges to a constant for large x. The solution corresponding to $J_0 = 0$ is given by

$$P_0(x) = N|U'(x)|\mathrm{e}^{-I(x)}. \tag{4.42}$$

For the case of a periodic potential we find J_0 by writing $P_0(1) = P_0(0)$ as

$$|U'(1)|\mathrm{e}^{-I(1)}\left[N - \frac{J_0}{D_\infty}\int_{0}^{1} dy\ \mathrm{e}^{I(y)}\right] = N|U'(0)|. \tag{4.43}$$

Using $U'(0) = U'(1)$ we find

$$J_0 = \frac{ND_\infty[\mathrm{e}^{-I(1)} - 1]}{\int_0^1 dy\ \mathrm{e}^{I(y)-I(1)}}. \tag{4.44}$$

For the periodic potential we arrive at a peculiar result: if $I(1) \neq 0$, we obtain a non-zero probability flux in the stationary state. We note that $I(x-1) = I(x) - I(1)$ for the periodic potential and rewrite the solution in a compact form:

$$P_0(x) = N|V'(x)|\mathrm{e}^{-I(x)}\int_{x}^{x+1} dy\ \mathrm{e}^{I(y)}. \tag{4.45}$$

In the next section we conclude that for the periodic potential with a broken reflection symmetry (shown in Fig. 4.1**c**) $I(1) \neq 0$, so that in this case there is a non-vanishing probability flux of the particles in the direction determined by the sign of J_0. In this case the particles are said to exhibit ratchet behaviour.

4.6 Numerical results and discussion

We performed a number of numerical experiments in order to investigate and validate our analytical results. The correlation function of the random force in our simulations was Gaussian:

$$C(x,t) = \sigma^2 \exp\left(-\frac{x^2}{2\eta^2} - \frac{t^2}{2\tau^2}\right). \tag{4.46}$$

For this correlation function we have $D_0 = \sqrt{\pi/2}\sigma^2\tau/\kappa^2$, $D_\infty = \sqrt{\pi/2}\sigma^2\eta/\kappa$, and $\xi = \sigma^2\tau^2/(\kappa^2\eta^2)$. We used two different types of the potential corresponding to the examples given in sections 4.4 and 4.5. One is the periodic potential with a broken reflection symmetry

$$U(x) = U_0[\sin(2\pi x/L) + k\sin(4\pi x/L)], \tag{4.47}$$

and the other is the symmetric double-well potential (see Fig. 4.1**a**)

$$U(x) = x^4/4 - x^2/2. \tag{4.48}$$

First we compare the results obtained in two asymptotic limits in the case of the double-well potential. In Fig. 4.2 we show the corresponding forcing $U'(x)$, the diffusion coefficient, and the stationary probability density. In general, the diffusion coefficient is given by Eq. (4.25). It can be approximated by the constant given by Eq. (4.28) in the regions where the external forcing is sufficiently weak. In the regions where the external forcing is strong, the diffusion coefficient decays according to Eq. (4.38). The probability density is given by the Eq. (4.26) with $J_0 = 0$ and can be evaluated numerically. According to Eq. (4.36), the probability density in the weak forcing limit is equivalent to the reduction of the potential by a small fraction measured in terms of the parameter ξ. In Fig. 4.2 we show the results for $\xi = 0.04$. With such a small value of ξ the difference in results of the classical Kramers model and the generalized one in the weak forcing limit is negligible and can hardly be observed using the results from the numerical simulations of the particles moving

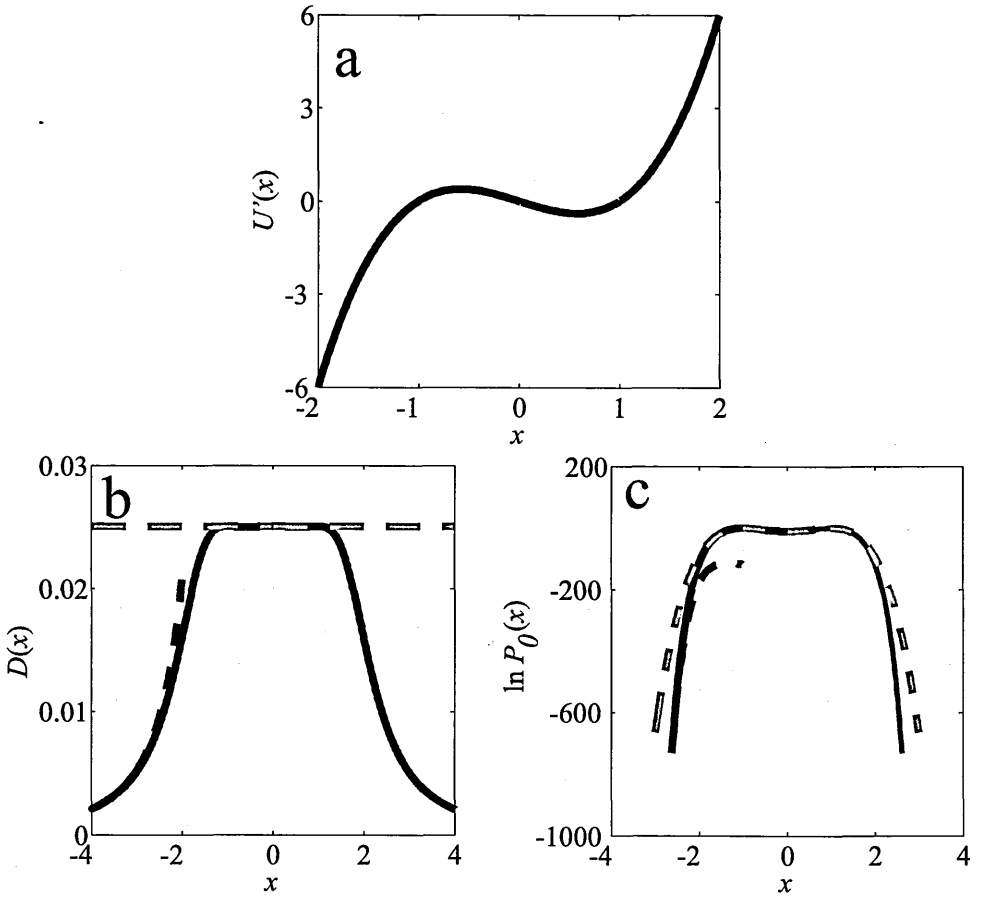

Figure 4.2: (**a**) External forcing in the double-well potential. (**b**) The diffusion coefficient given by Eq. (4.25) (black solid line), compared with the constant given by Eq. (4.28) (red dashed line) in the regions where the external forcing is weak, and with Eq. (4.38) (blue dashed line) in the region where the external forcing is strong. (**c**) The probability density $P_0(x)$ given by Eq. (4.26) (black solid line), compared with the result of the classical Kramers model (Eq. (4.15), red dashed line) in the regions where the external forcing is weak, and with Eq. (4.42) (blue dashed line) in the region where the external forcing is strong. The parameters are $\sigma = 1.0$, $\tau = 0.02$, $\eta = 0.1$, $\kappa = 1$, which gives $\xi = 0.04$.

according to the equation of motion (4.1). For $\xi \to 0$ this probability density can be then approximated by the results of the classical model Eq. (4.15) in the regions where the external forcing is weak. In the strong forcing limit we use the result given by Eq. (4.42). We also remark that when ξ is very small, there is a vanishingly small probability that the particles can reach the regions where $U'(x)$ is sufficiently large, so that the diffusion coefficient decreases significantly.

In [25] the numerical simulations were done with $\xi \approx 0.5$, where the difference between the classical and generalized models was argued to be quite significant. From our numerical simulations we found that the result in the weak forcing limit does not

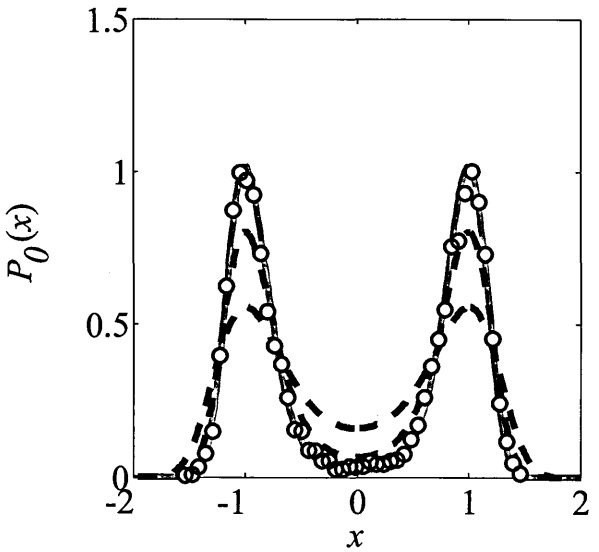

Figure 4.3: Shows the stationary probability density $P_0(x)$ in the generalized Kramers model (for the double-well potential). The theory (given by Eq. (4.49), red solid line) is compared with the results from numerical simulations (circles). Also shown are the results for $\xi = 0$ (blue dashed line) and from [25] (Eq. (4.36), black dashed line). The parameters are $\sigma \approx 3.36$, $\tau \approx 0.007$, $\eta \approx 0.034$, $\kappa = 1$. This gives $\xi \approx 0.5$.

agree with Eq. (4.36). We argue that the correct result is the increase of the potential, rather than the decrease:

$$P_0(x) = N \exp\left[-\frac{U(x)(1+\xi)}{D_0}\right]. \tag{4.49}$$

We performed the simulations with the same parameters as in [25]. The results are shown in Fig. 4.3 which confirms Eq. (4.49). We expect that as ξ decreases, the result approaches that of the classical Kramers model according to Eq. (4.49), and the result Eq. (4.36) obtained in [25] is therefore incorrect. Although the result for the drift velocity given by Eq. (4.23) is correct, we suggest that in the weak forcing limit the expression for the diffusion coefficient given by Eq. (4.25) may no longer be valid. In this case it is necessary to consider a correction of the diffusion coefficient taking into account contributions not only from the deterministic term $s_x(t) = -U'(x)t$, but also from the random force [similar to the derivation of the drift velocity in Eq. (4.21)]. The correction term for the diffusion coefficient is expected to be linear in ξ, so that the result Eq. (4.49) is justifiable. This suggestion is yet to be rigorously verified.

We conclude our discussion by noting that the results of section 4.5 appear to be

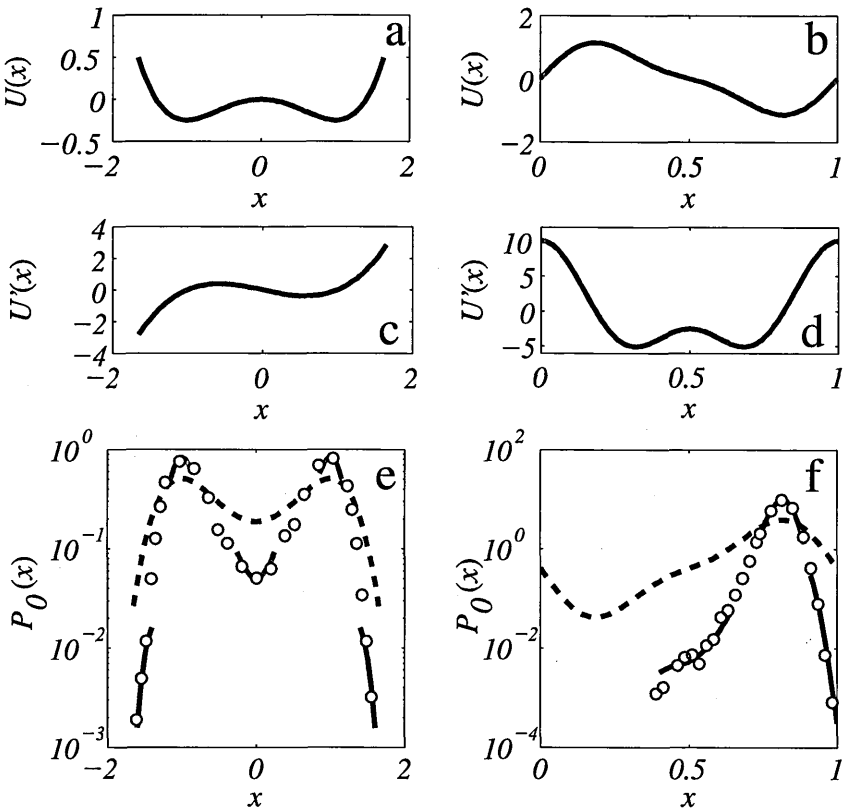

Figure 4.4: Probability density $P_0(x)$ in the generalized Kramers model. The results in panels **e** and **f** are for the motion in the non-periodic [(4.48), (**a**)] and periodic potentials [(4.47), **b**], respectively. The corresponding external force $U'(x)$ is shown in panels **c** and **d**. Data for the PDF from the numerical simulation (circles) are compared with Eq. (4.49) (red line) in the regions where $U'(x)$ is small and with Eq. (4.42) and Eq. (4.45) (blue solid lines) in the regions where $U'(x)$ is large for non-periodic and periodic cases, respectively. Corresponding PDFs for the classical Kramers model (blue dashed line) are given by Eq. (4.15). PDFs from the numerical simulations and for the classical model are normalized. Other theoretical curves are fitted by adjusting N to give the best agreement. The dimensional parameters are $\sigma = 2.0$, $\tau = 0.05$, $\eta = 0.05$, $\kappa = 1.0$, $L = 1$ in both cases. For the periodic case $U_0 = 0.5$ and $k = 0.3$ are used.

valid, because the external forcing is large and the diffusion coefficient is justifiably given by Eq. (4.25). With a sufficiently large ξ we are able to illustrate the results for the large forcing limits using the numerical simulations. The numerical results for the steady-state PDF and their comparison with the theory are summarized in Fig. 4.4. For the double-well potential the particles are concentrated around two minima of the potential with a spread which is smaller compared with the classical Kramers model, where the correlation length is infinite [according to Eq. (4.49)]. The tails of the PDF in the regions of sufficiently strong external forcing are given by Eq. (4.42).

For the periodic potential the particles are again concentrated densely around the single minimum of the potential, where the PDF is given by Eq. (4.49) with the tails given by Eq. (4.45). If the potential is periodic and asymmetric, the particles in the generalized Kramers model are expected to favour a slope with a smaller inclination to escape the minimum. In the regions where the external forcing is strong, the random impulse δw with the variance given by the diffusion coefficient (4.38) tends to decrease. Consequently, the particles tend to propagate in the regions where $|U'(x)|$ is smaller (the slope to the left of the minimum in Fig. 4.4**b**).

The direction of the transport can also be deduced from Eq. (4.41). For any periodic potential integrating $U'(x)$ in the periodicity interval gives zero. Because the integrand in Eq. (4.41) is quadratic in $U'(x)$, the sign of $I(1)$ is determined by the sign of the steepest of two slopes of the potential with a single minimum in the periodicity interval. In Fig. 4.4, it is the slope to the right of the minimum, which corresponds to $U'(x) > 0$ and $I(1) > 0$. From Eq. (4.44) we obtain $J_0 < 0$, implying that it is easier for particles to escape from the minimum using the left slope, as expected.

4.7 Summary

In this chapter we have studied a natural generalization of the classical model for diffusion, the Kramers model. The generalized model describes an overdamped particle in an external potential driven by the random force which depends on the position of the particle, as well as time. Our main original result is the probability density function of the position of the particle in a steady state, analyzed in the strong external forcing limit. We have also discussed the weak forcing limit, which yields the reduction of the drift velocity. We have argued that this does not lead to the reduction of the potential in the probability density (obtained in [25]), because the diffusion coefficient is also expected to decrease. From the numerical simulations we have obtained that in the weak forcing limit the result is equivalent to the increase of the potential compared with the classical Kramers model. In the large external forcing limit we have obtained the density function which yields a non-zero probability flux in the case of the motion

in a periodic potential with a broken reflection symmetry, implying that the particle tends to escape the potential minimum in a direction determined by the sign of the probability flux.

Chapter 5

Collision rate of inertial particles

Some parts of this chapter were published in the paper "Caustic activation of rain showers" by Wilkinson, Mehlig and Bezuglyy in Phys. Rev. Lett., **97**, 048501, (2006). The author of the thesis contributed to the numerical simulations, as well as to the discussion of the theory.

5.1 Introduction

In this chapter we study the collision rate of inertial spherical particles suspended in complex flows. This problem arises in many natural processes which involve particles aggregating due to collisions. For instance, knowing the collision rate, we can estimate how long it takes for droplets of moisture in cumulus clouds to grow to sizes of rain droplets. We may also estimate how rapidly grain dust particles in an accretion disk aggregate to form structures large enough, so that the gravitational attraction becomes significant and planetesimals are formed. The problem of planet formation is more challenging, because it is also necessary to estimate a typical relative speed of the collisions. If this speed is too large, the aggregates of the grain dust would be fragmented upon collision. Water droplets are more resistant to fragmentation upon collision due to the surface tension. In this chapter we shall study the collision rate and use our theory to estimate the time scale at which rainfall is initiated. In the following, we shall not concern with the collision speed.

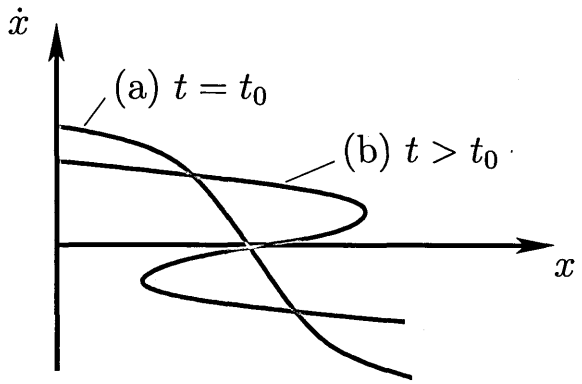

Figure 5.1: Schematic showing the formation of a caustic in the one-dimensional model: (a) Initial configuration, showing manifold representing particle velocity as a function of position. (b) This manifold has developed fold caustics. The velocity field is multivalued between the folds.

The idea of droplets coalescence in clouds has a long history [57], but a satisfying theory has been elusive and the topic remains a subject of intensive research, reviewed recently in [1]. It is believed that in cumulus clouds the convection gives rise to small-scale turbulent motion, which facilitates the coalescence of microscopic water droplets ('visible moisture') into raindrops due to collisions. Numerical experiments show a dramatic increase in the rate of collision of suspended particles, when the intensity of turbulence exceeds a certain threshold. This effect was first described in [26]. The common view is that the increased rate of collision involves spatial clustering of particles [1, 7, 26, 27], which we have mentioned in the first chapter. One exception is [12], which presents a theory having elements in common with the theory presented in this chapter, but which is more complex in its formulation and less precise in its conclusions. The widely accepted view is that clustering is due to particles being centrifuged away from regions of high vorticity. It is argued that this effect is strongest when the Stokes number (dimensionless measure of the inertia of droplets), St, is close to unity: it does not occur when the droplets are very light and simply advected by the flow ($\mathrm{St} \ll 1$), or when the motion is underdamped and vortices are too short-lived ($\mathrm{St} \gg 1$). Numerical simulations indicate, however, that the collision rate rises abruptly at a threshold value of St and remains high for $\mathrm{St} \gg 1$: this is equally true for simulations of single-scale flows, such as those presented in the thesis, and multi-scale flows, such as those in [26]. Furthermore, it has not been established that

the centrifuge mechanism is sufficiently effective to explain the large increase in the collision rate at $\mathrm{St} = O(1)$.

In our theory, the dramatic increase in the collision rate is a consequence of the formation of 'caustics' discussed briefly in the first chapter. We remind that the term 'caustics' is used in reference to the phenomenon when the velocity field of particles becomes multivalued. In figure 5.1 we remind how caustics are formed in the one-dimensional model. The velocity of the particles as a function of the position is initially single-valued [curve (a)], but particles with larger velocities overtake slower-moving particles, so that at a later time the particle velocity is multivalued [curve (b)]. The region where the velocity is a multivalued function is bounded by two fold caustics. The caustics have two effects which could enhance the collision rate of particles. Firstly, at the caustic lines there can be a divergence in the density of particles. This effect is discussed in [11, 12]. The other effect of the caustics is that when the velocity field is multivalued, particles which are very close to each other are moving with significantly different velocities, and their relative motion produces collisions. The importance of this effect was also emphasized in [12].

In our theory we consider the rate of collision between particles both with and without caustics, and the rate at which caustics are formed. Saffman and Turner [57] discussed collisions (due to shearing motion) of particles which are advected by the flow: this approximation is valid in the limit as $\mathrm{St} \to 0$; we term this advective collision rate R_a. At large Stokes numbers we use a theory due to Abrahamson [58], which treats the droplets as a gas of particles with random and uncorrelated velocities and calculates the collision rate R_g by gas-kinetic theory. This theory is regarded as being applicable only at very large Stokes numbers, and we show that two theories give results which differ by a factor of order of the size of the particle at $\mathrm{St} \approx 1$. This might be taken as evidence that at least one of these theories does not work when the Stokes number is of order unity. However, we shall argue that the gas-kinetic model is applicable as soon as caustics have formed and that the collision rate is well-approximated by

$$R = R_a + g(\mathrm{St}, \mathrm{Ku}) R_g, \tag{5.1}$$

where $g(\mathrm{St}, \mathrm{Ku})$ is the fraction of the coordinate space for which the velocity field has become multivalued due to the formation of caustics, and Ku is the Kubo number, a dimensionless measure of how rapidly the flow fluctuates. We shall show that the formation of caustics is equivalent to a noise-activated escape of the particle from an attractive fixed point in a potential (the Kramers model discussed in chapter 4). This implies that the rate of formation of caustics and, consequently, $g(\mathrm{St}, \mathrm{Ku})$ are given by the rate of escape of the particle in the Kramers model. The collision rate can be regarded as an activated process, similar to a chemical reaction. We argue that $g(\mathrm{St}, \mathrm{Ku}) = \exp(-S/\mathcal{I})$, where S is a constant which depends on Ku, and $\mathcal{I}$ is a dimensionless measure of the intensity of turbulence (defined below).

The chapter is organized as follows. In section 5.2 we remind basic equations of motion and introduce the model of collisions. Section 5.3 discusses the collision rate of particles advected in a flow. In section 5.4 we discuss the collision rate at large Stokes numbers, where a gas-kinetic model due to Abrahamson is applicable. Two asymptotic theories give results which differ by a factor of the size of the particles. In 5.5 we argue that the transition between two theories exhibits an activated behaviour due to the formation of caustics. We discuss the rate of formation of caustics in some details and show that the problem is equivalent to the problem of the escape of a particle in the Kramers model. We compare our theoretical results with numerical simulations.

5.2 The model of collisions

We discuss the collision rate in a population of independent (i.e. non-interactive) small spherical (or circular in the two-dimensional case) particles of the same radius a. The particles are suspended in a flow $\boldsymbol{u}(\boldsymbol{r}, t)$. The equation of motion of a particle at position $\boldsymbol{r}(t)$ is given by Eq. (2.38), which we repeat for reference:

$$\ddot{\boldsymbol{r}} = \gamma[\boldsymbol{u}(\boldsymbol{r}, t) - \dot{\boldsymbol{r}}] \tag{5.2}$$

with the damping rate γ. The flow $\boldsymbol{u}(\boldsymbol{r},t)$ is incompressible and characterized by its time scale τ, length scale η and velocity scale u_0. We do not include gravitational settling or other effects which may also occur. The model is characterized by a number of dimensionless parameters, which we have discussed in chapter 2. The inertia of the particles is measured using the Stokes number, $\mathrm{St} = (\gamma\tau)^{-1}$. The velocity field is characterized by the Kubo number, $\mathrm{Ku} = u_0\tau/\eta$, which measures how rapidly the flow fluctuates. Dimensional arguments of the Kolmogorov theory of turbulence suggests that in a turbulent flow $\mathrm{Ku} = O(1)$ [9]. This parameter can also be small in stirred fluids. The particle may cluster when $\mathrm{St} = O(1)$, so that the particle density number may fluctuate in space. At large, as well as at small Stokes numbers, clustering effects are negligible, and we may assume that the particles number density is constant. We denote the number density n, which gives a packing fraction $n_0 = n\eta^d$, where d is the dimensionality of space. The relative size of the particles is $a_0 = a/\eta$. Both n_0 and a_0 are typically small in clouds (see section 5.6).

Two particles are regarded as having collided if their separation falls below $2a$ (see Fig. 5.2). Different sources study different collision rates. The quantity we are interested in is a number of collisions of one test particle with other particles per unit time. Thus, the collision rate is given by the number of particles per unit time entering a sphere of radius $2a$ centred at the test particle. In different situations, after a collision two particles may coalesce, fragment or recoil, but in the following we only consider their first encounter, and do not consider various effects of collisions.

5.3 Advective collisions

In this section we discuss the collision rate R_a of particles advected by the flow. In the limit when $\mathrm{St} \ll 1$, advected particles are brought into contact by the effect of shearing motion of the fluid (see Fig. 5.3). The equation of motion of the particles reads

$$\dot{\boldsymbol{r}} = \boldsymbol{u}(\boldsymbol{r},t). \tag{5.3}$$

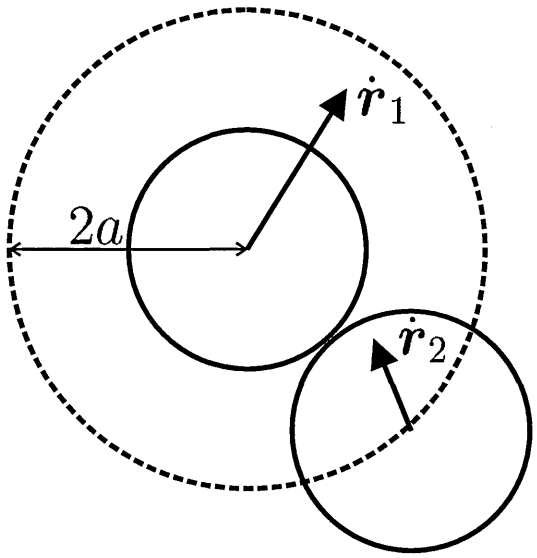

Figure 5.2: Two circular particles with velocities $\dot{r}_1$ and $\dot{r}_2$ collide when their separation falls below $2a$.

The first result on the problem of advective collisions was obtained by Smoluchowsky [59] for the motion in a laminar shear flow

$$\boldsymbol{u}(\boldsymbol{r}, t) = (ky, 0, 0), \tag{5.4}$$

where k is a constant shear rate. The number of particles which enter the sphere of radius $2a$ centred at the test particle in a small time interval is given by the change of volume flow of particles in this time interval multiplied by their number density. The change of the volume flow in the sphere is given by the surface integral

$$\frac{dV}{dt} = -\int_{v_r'<0} v_r' dA, \tag{5.5}$$

where v_r' is the radial component of the relative velocity between the test particle and the particles which enter the sphere. In Eq. (5.5) the integration is on the surface of the sphere of radius $2a$, and only contributions with negative radial components v_r' are considered (the radial direction is away from the test particle). This makes it possible to count collisions only with the particles which enter the sphere to avoid double counting of the particles that have already collided and move away from the test particle. The relative speed between two particles separated by $\delta\boldsymbol{r} = (\delta x, \delta y, \delta z)$

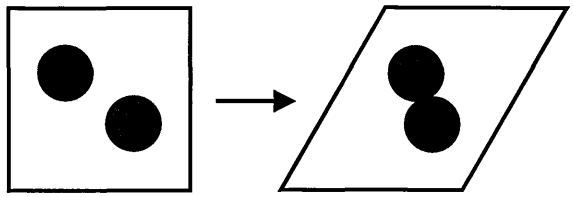

Figure 5.3: Two particles advected by the flow collide due to the effect of shearing motion of the fluid.

in a uniform shear flow is $v_r = k\delta y$. The collision rate is obtained by multiplying the volume flow by the number density of particles n and using the spherical coordinate system to evaluate the integral in Eq. (5.5) [60]:

$$R_a = -n \int_{v_r'<0} v_r' dA = \frac{4}{3} nk(2a)^3. \tag{5.6}$$

In the two-dimensional case the result is $R_a \sim a^2$.

Saffman and Turner [57] studied the collision rate of particles advected in a turbulent flow. In this case the relative speed v_r is random, and the collision rate is obtained by averaging over this speed. When $\mathrm{St} \ll 1$, the relative velocity $\delta \boldsymbol{u} = \delta \dot{\boldsymbol{r}}$ of two particles separated by $\delta \boldsymbol{r}$ is obtained by the linearization of Eq. (5.3):

$$\delta \boldsymbol{u} = \mathbf{A} \delta \boldsymbol{r} + O(|\delta \boldsymbol{r}|^2), \tag{5.7}$$

where $\mathbf{A} = \partial u_i / \partial r_j$ is the Jacobian matrix of the flow. Thus, the relative speed of the particles at small Stokes numbers is proportional to their separation, when $|\delta \boldsymbol{r}|$ is sufficiently small. Using dimensional arguments, we can estimate the collision rate in a flow characterized by its temporal, spatial and velocity scales, τ, η and u_0, respectively. The typical shear rate is u_0/η, from which we obtain that the relative speed for particles which are brought into contact is $\Delta v \sim a u_0/\eta$. The volume swept in time Δt is $\Delta V \sim a^d u_0 \Delta t/\eta$ in d spatial dimensions. Collisions typically occur when $n\Delta V \sim 1$, so that the expected rate of collision is $R_a = C_a n a^d u_0/\eta$, where C_a is a constant. Using the Saffman and Turner result, the pre-factor C_a can be obtained approximately. The formula for the collision rate in an isotropic random flow reads

(see, e.g. [62])

$$R_a = A_d(2a)an\langle|A_{11}(\mathbf{0},0)|\rangle, \tag{5.8}$$

where $A_d(r)$ is the area of the surface of the sphere of radius r (we have $A_2(r) = 2\pi r$ and $A_3(r) = 4\pi r^2$) and A_{11} is an element of the Jacobian matrix (due to rotational invariance, any element of the matrix $\mathbf{A}$ can be used in this case). For the Gaussian flow $\boldsymbol{u}(\boldsymbol{r}, t)$ we have

$$\langle|A_{11}|\rangle = \sqrt{\frac{2}{\pi}}\sqrt{\langle A_{11}^2\rangle}. \tag{5.9}$$

Using this result and Eq. (5.8) we obtain the advective collision rate in the three-dimensional case:

$$R_a = 16\sqrt{2\pi}a^3 n\sqrt{\langle A_{11}^2\rangle}. \tag{5.10}$$

In the two-dimensional case the result is

$$R_a = 4\sqrt{2\pi}a^2 n\sqrt{\langle A_{11}^2\rangle}. \tag{5.11}$$

The result based on the theory due to Saffman and Turner gives only an approximate result for the collision rate that can be calculated analytically if the correlation functions of the flow field are known, and $\langle|A_{11}|\rangle$ can be calculated explicitly. This result is only valid for a short-time initial transient of R_a, since the time-dependence of the flow is neglected. This approach gives a precise asymptote for the steady hyperbolic flow, where the particle can approach each other only once. These calculations does not account for multiple encounters in generic flows (which are not steady and may be locally elliptic). In [61, 62] the advective collision rate is obtained as a function of time for a generic flow taking into account the time-dependence of the flow and a possibility of multiple encounters. Since out primary goal is to explain precipitous increase of the collision rate at $\mathrm{St} = O(1)$, we shall use the results given by Eqs. (5.10) and (5.11) in the general formula for the collision rate discussed in section 5.5.

5.4 Collisions in a gas-kinetic model

When the inertia of particles is large (St $\gg 1$), they completely detach from the flow, and their motion becomes uncorrelated with each other and with that of the fluid. In this case a gas-kinetic model is appropriate [58]. The rate of collision in this case is exactly the same as for a hard-sphere gas with the same particle radius a and r.m.s. velocity. For illustrative purposes, we first consider the case when the test particle travels with a speed v in a homogenous population of stationary particles with a number density n. In the three-dimensional case, the test particle in time Δt collides with the particles in a cylinder of radius $2a$ and height $v\Delta t$. The number of particles ΔN in this cylinder is given by

$$\Delta N = 4\pi a^2 v \Delta t n. \tag{5.12}$$

In the two-dimensional case, it is the area of the rectangle with sides $4a$ and $v\Delta t$ which should be used to obtain this number:

$$\Delta N = 4av\Delta t n. \tag{5.13}$$

If the particles are not stationary, the speed v in the formulae for ΔN should be replaced with the relative speed v_r. The collision rate in a gas model is then obtained by dividing ΔN by Δt and averaging over the relative speed. We therefore obtain the collision rate for St $\gg 1$ in the three-dimensional case:

$$R_g = 4\pi a^2 \langle v_r \rangle n. \tag{5.14}$$

In the two-dimensional case the collision rate is given by

$$R_g = 4a \langle v_r \rangle n. \tag{5.15}$$

The average relative speed can be calculated using the equation of motion (5.2)

written in terms of the velocity $\boldsymbol{v} = \dot{\boldsymbol{r}}$:

$$\dot{\boldsymbol{v}} = \gamma[\boldsymbol{u}(\boldsymbol{r}, t) - \boldsymbol{v}]. \tag{5.16}$$

The condition that St $\gg 1$ implies that the velocity field of the fluid fluctuates very rapidly compared to the time scale of fluctuations of the velocity of the particle. In addition, if the displacement of the particle in a time interval of order τ is small compared to the length scale η, then Eq. (5.16) is analogous to the Ornstein-Uhlenbeck process [see section 2.4.4]. This displacement is of order $u_0\tau$, and it is small when the Kubo number is not very large. The velocity distribution of the particles in this case is Maxwellian [see Eq. (2.89)], and so is the distribution of their relative velocities. In a gas where the velocities of the particles are uncorrelated, we have for the relative velocity $\boldsymbol{v}_r$:

$$\langle |\boldsymbol{v}_r|^2 \rangle = 2\langle |\boldsymbol{v}|^2 \rangle. \tag{5.17}$$

Since $\boldsymbol{v}_r$ obeys Maxwellian distribution, we have for the relative speed $v_r = |\boldsymbol{v}_r|$ in the three-dimensional case:

$$\langle v_r \rangle = \sqrt{\frac{8}{3\pi}} \sqrt{\langle |\boldsymbol{v}_r|^2 \rangle}. \tag{5.18}$$

In the two-dimensional case we obtain

$$\langle v_r \rangle = \sqrt{\frac{\pi}{4}} \sqrt{\langle |\boldsymbol{v}_r|^2 \rangle}. \tag{5.19}$$

We can calculate the relative speed in terms of the velocity of the particle using Eq. (5.17):

$$\langle v_r \rangle = \frac{4}{\sqrt{3\pi}} \sqrt{\langle |\boldsymbol{v}|^2 \rangle} \tag{5.20}$$

and

$$\langle v_r \rangle = \sqrt{\frac{\pi}{2}} \sqrt{\langle |\boldsymbol{v}|^2 \rangle} \tag{5.21}$$

in the three- and two-dimensional cases, respectively. In order to obtain $\langle |\boldsymbol{v}|^2 \rangle$, we

consider the solution of Eq. (5.16):

$$\boldsymbol{v}(t) = \gamma \int_0^t dt_1 \, \mathrm{e}^{-\gamma(t-t_1)} \boldsymbol{u}[\boldsymbol{r}(t_1), t_1] \tag{5.22}$$

assuming that $\boldsymbol{v}(0) = \boldsymbol{0}$. Squaring and averaging this expression gives

$$\langle |\boldsymbol{v}(t)|^2 \rangle = \gamma^2 \mathrm{e}^{-2\gamma t} \int_0^t dt_1 \int_0^t dt_2 \, \mathrm{e}^{\gamma(t_1+t_2)} \langle \boldsymbol{u}[\boldsymbol{r}(t_1), t_1] \boldsymbol{u}[\boldsymbol{r}(t_2), t_2] \rangle. \tag{5.23}$$

When the Kubo number is not large, we can neglect the displacement of the particles in the correlation function in Eq. (5.23). For a stationary, isotropic, and translationally invariant velocity field we have then

$$\langle \boldsymbol{u}[\boldsymbol{r}(t_1), t_1] \boldsymbol{u}[\boldsymbol{r}(t_2), t_2] \rangle \approx \langle \boldsymbol{u}(\boldsymbol{0}, 0) \boldsymbol{u}(\boldsymbol{0}, t_1 - t_2) \rangle. \tag{5.24}$$

We introduce new variables $t' = t_1 + t_2$ and $t'' = t_1 - t_2$ and rewrite Eq. (5.23):

$$\begin{aligned} \langle |\boldsymbol{v}(t)|^2 \rangle &= \frac{\gamma^2}{2} \mathrm{e}^{-2\gamma t} \int_0^{2t} dt' \, \mathrm{e}^{\gamma t'} \int_{-t}^{t} dt'' \, \langle \boldsymbol{u}(\boldsymbol{0}, 0) \boldsymbol{u}(\boldsymbol{0}, t'') \rangle \\ &= \frac{\gamma}{2} (1 - \mathrm{e}^{-2\gamma t}) \int_{-t}^{t} dt'' \, \langle \boldsymbol{u}(\boldsymbol{0}, 0) \boldsymbol{u}(\boldsymbol{0}, t'') \rangle. \end{aligned} \tag{5.25}$$

When $t \gg \gamma^{-1}$, the integral over the correlation function in this expression is dominant around $t'' = 0$, so that we obtain

$$\langle |\boldsymbol{v}|^2 \rangle = K\gamma, \tag{5.26}$$

where

$$K = \frac{1}{2} \int_{-\infty}^{\infty} dt \, \langle \boldsymbol{u}(\boldsymbol{0}, 0) \boldsymbol{u}(\boldsymbol{0}, t) \rangle. \tag{5.27}$$

Using dimensional arguments we have $K \sim u_0^2 \tau$ implying that $\langle |\boldsymbol{v}|^2 \rangle \sim u_0^2 \mathrm{St}^{-1}$. The collision rate in the three-dimensional case is then given by

$$R_g = 16 \sqrt{\frac{\pi}{3}} a^2 n \sqrt{K\gamma}. \tag{5.28}$$

In the two-dimensional case we obtain

$$R_g = 2\sqrt{2\pi} a n \sqrt{K\gamma}. \tag{5.29}$$

We obtain that when $\mathrm{St} \gg 1$, the collision rate decreases algebraically as $\mathrm{St}^{-1/2}$. This result is valid for the motion in a single-scale flow and confirmed by our numerical simulations presented in section 5.5. We remark that multi-scale properties of the flow may change this result, as was shown in [63, 64], where the result in the limit of very large Stokes number is $R_g \sim \mathrm{St}^{1/2}$. This, however, does not modify our main conclusion regarding the dramatic increase of the collision rate, and in the following we shall only use the results given by Eqs. (5.28) and (5.29).

5.5 Caustic activation of the collision rate

Using the results obtained in the previous chapters, the ratio of the collision rate for the cases when $\mathrm{St} \ll 1$ and $\mathrm{St} \gg 1$ is of order a/η when $\mathrm{St} \approx 1$. This seems to suggest that either both these results or at least one of them are not valid when the Stokes number is of order unity. We argue that the collision rate for a gas-kinetic model is applicable at $\mathrm{St} \approx 1$ if caustics are taken into account. Before we proceed to the formula for the collision rate, we discuss the process of formation of caustics in more details.

5.5.1 Rate of formation of caustics

Let us consider two particles in the one-dimensional model: a reference particle at position $x(t)$ with momentum $p(t) = m\dot{x}$ and a nearby particle at position $x(t) + \delta x$ with momentum $p(t) + \delta p$. The equation describing the dynamics of δx and δp is obtained by linearizing Eq. (5.2) in the one-dimensional case. We have

$$\begin{aligned} \dot{\delta x} &= \frac{\delta p}{m}, \\ \dot{\delta p} &= -\gamma \delta p + \frac{\partial f}{\partial x} \delta x, \end{aligned} \tag{5.30}$$

where $f(x,t) = \gamma m u(x,t)$. If we denote $X = \delta p/\delta x$, we obtain

$$\begin{aligned} \dot{\delta x} &= X\frac{\delta x}{m}, \\ \dot{X} &= -\gamma X - \frac{X^2}{m} + \frac{\partial f}{\partial x}. \end{aligned} \tag{5.31}$$

The equation describing the dynamics of X is a stochastic differential equation in which the velocity gradient $\partial_x f$ acts as a random forcing term. Thus, X can be regarded as a position of a fictitious particle moving in the external potential $U(X) = \gamma X^2/2 + X^3/(3m)$ and driven by the random force. Its dynamics is therefore described by the Kramers model discussed in chapter 4. A caustic is encountered whenever δx passes through zero, implying that X goes to infinity in one direction, then jumps instantaneously to the reflected point at infinity. Let is consider the case when $\gamma = m = 1$. The potential (illustrated in Fig. 5.4) has a minimum at $X = 0$ and a maximum at $X = -1$. The rate of formation of caustics is therefore given by the rate at which X overcomes the barrier of height $U(-1)$ and escapes an attractive point $X = 0$ to $-\infty$. If the force fluctuates sufficiently rapidly, the dynamics of X can be described by the Fokker-Planck equation for the probability density $P(X,t)$. The steady-state density $P_0(X)$ for the case when the dependence of the random noise upon X can be neglected is given by Eq. (4.13):

$$P_0(X) = N\mathrm{e}^{-\frac{U(X)}{D}} - \frac{J_0}{D}\int_{-\infty}^{X} dX_1\, \mathrm{e}^{\frac{U(X_1)-U(X)}{D}}, \tag{5.32}$$

where N is the normalization constant, J_0 is the stationary probability flux, and D is the diffusion constant given by

$$D = \frac{1}{2}\int_{-\infty}^{\infty} dt\, \left\langle \frac{\partial f}{\partial x}(0,0)\frac{\partial f}{\partial x}(0,t) \right\rangle. \tag{5.33}$$

In view of the potential shown in Fig. 5.4, the solution can only be normalized when $N = 0$. We have

$$P_0(X) = -\frac{J_0}{D}\int_{-\infty}^{X} dX_1\, \mathrm{e}^{\frac{U(X_1)-U(X)}{D}}, \tag{5.34}$$

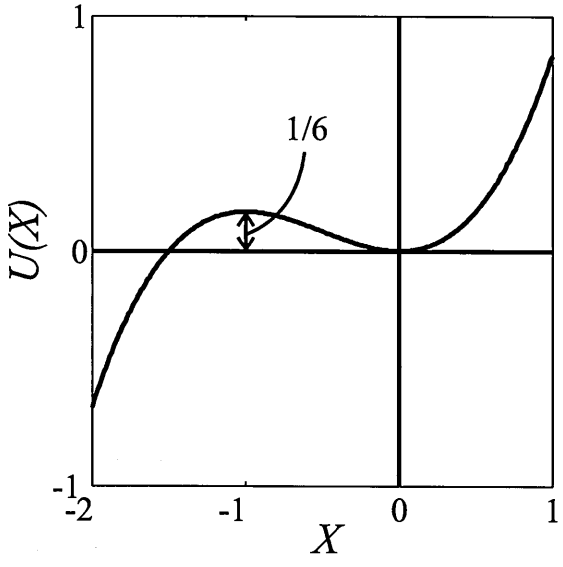

Figure 5.4: A caustic in the one-dimensional model is encountered whenever $X = \delta p/\delta x$ overcomes the potential barrier of height 1/6 (in the case of $\gamma = m = 1$) and escapes to $-\infty$.

where J_0 is determined by the normalization condition. The flux $|J_0|$ determines the rate at which X escapes the minimum, and therefore the rate at which a caustic is encountered. Using the result due to Kramers [23], this rate in the case of a single attractive point X_0 is given by

$$J_0 \sim \exp[-U(X_0)/D], \tag{5.35}$$

which is similar to the Arrhenius law for the temperature dependence of a chemical reaction rate (4.2). In the Arrhenius law, $U(X_0)$ is equivalent to the activation energy. The diffusion constant measures the strength of random fluctuations and therefore is equivalent to the temperature. In this sense we may regard the formation of caustics as an activated process.

Similar results for the rate J_0 can be obtained in two [11] and three [65] spatial dimensions. They can be expressed in terms of a dimensionless parameter $\mathcal{I}$ (which is the scaled diffusion constant) defined in terms of the strain-rate correlation function

$$\mathcal{I} = \frac{1}{2\gamma}\int_{-\infty}^{\infty} dt \left\langle \frac{\partial u_1}{\partial x_1}(\mathbf{0},t)\frac{\partial u_1}{\partial x_1}(\mathbf{0},0)\right\rangle. \tag{5.36}$$

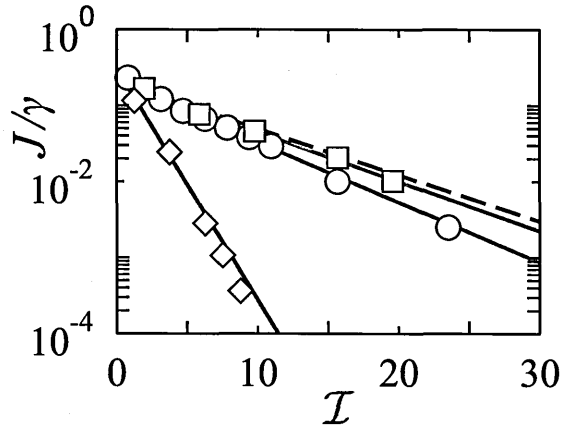

Figure 5.5: Rate of caustic formation as a function of $\mathcal{I} \propto \mathrm{Ku}^2\mathrm{St}$, showing evidence for the activated behaviour: Ku = 1 (diamonds), with action $S = 0.70$, Ku = 0.2, $S = 0.18$ (circles), and Ku = 0.04, $S = 0.15$ (boxes). Also shown is the limiting behaviour as Ku $\to$ 0, with action $S = 0.14$ (dashed line).

The corresponding rate of formation of caustics is given by

$$J_0 \sim \exp(-S/\mathcal{I}), \tag{5.37}$$

where S is a constant determined by the height of the barrier in dimensionless units. In the one-dimensional case we obtain $S = 1/6$ by putting $\gamma = m = 1$ [66]. In two and three dimensions we have $S \approx 0.14$ [11] and $S \approx 0.12$ [65]. Although these results are found in the limit as Ku $\to$ 0, our results from numerical simulations suggest that the activated behaviour is observed when Ku $= O(1)$. In Fig. 5.5 we present the numerical results for the rate J, which show evidences of the activated behaviour of the rate of formation of caustics even when Ku approaches unity. We find that the value of S depends upon Ku. For our model of the two-dimensional flow (described in section 5.5.3) we found $S = 0.70$ for Ku = 1, $S = 0.18$ for Ku = 0.2 and $S = 0.15$ for Ku = 0.04, consistent with the limiting value $S = 0.14$ for Ku $\to$ 0 quoted above.

5.5.2 Collision rate and caustics

Here, we present the formula for the collision rate which includes the formation of caustics as a prevailing factor of the increased rate at a threshold value of St. We

argue that the collision rate is well-approximated by Eq. (5.1), where the transition between the asymptotic results for $\mathrm{St} \ll 1$ and $\mathrm{St} \gg 1$ is given by the activation law (5.37). We argue that $g(\mathrm{St}, \mathrm{Ku}) = \exp(-S/\mathcal{I})$ and our formula for the collision rate reads

$$R = R_a + \exp(-S/\mathcal{I}) R_g. \tag{5.38}$$

We remark that $g(\mathrm{St}, \mathrm{Ku})$ can be seen as the fraction of the coordinate space for which the velocity field has become multivalued due to the formation of caustics. Formulae for the advective and gas-kinetic collision rates, R_a and R_g respectively, are given in sections 5.3 and 5.4. We remark that combining equations (2) and (4) of [12] gives an expression that can be written in the form $R = R_a + P\, R_c$, analogous to our Eq. (5.38), in which R_c is similar to the precise asymptote R_g. The expression for the factor P in [12] has a different dependence upon St.

5.5.3 Numerical simulations

In our numerical simulations we used a two-dimensional model in which the single-scale velocity field $\boldsymbol{u}(\boldsymbol{r}, t)$ was obtained from a random stream function $\psi(\boldsymbol{r}, t)$ by writing $\boldsymbol{u} = (\partial\psi/\partial y, -\partial\psi/\partial x)$ [see Eq. (2.10)]. The stream function $\psi(\boldsymbol{r}, t)$ was a Gaussian random field with spatially and temporally stationary, isotropic statistics and zero mean. For the correlation function of the stream function we use

$$C(r, t) = u_0^2 \eta^2 \exp\left(-\frac{t^2}{2\tau^2} - \frac{r^2}{2\eta^2}\right) \tag{5.39}$$

discussed in chapter 2. Using this correlation function we obtain:

$$\langle A_{11}^2(\mathbf{0}, 0)\rangle = \left\langle \left[\frac{\partial^2\psi}{\partial x \partial y}(\mathbf{0}, 0)\right]^2 \right\rangle = \frac{\partial^4 C}{\partial x^2 \partial y^2}(0, 0) = \frac{u_0^2}{\eta^2}, \tag{5.40}$$

$$\begin{aligned} K &= \int_{-\infty}^{\infty} dt \left\langle \frac{\partial\psi}{\partial x}(\mathbf{0}, 0) \frac{\partial\psi}{\partial x}(\mathbf{0}, t) \right\rangle \\ &= -\int_{-\infty}^{\infty} dt \, \frac{\partial^2 C}{\partial x^2}(0, t) = \sqrt{2\pi} u_0^2 \tau, \end{aligned} \tag{5.41}$$

and

$$\mathcal{I} = \frac{1}{2\gamma}\int_{-\infty}^{\infty} dt \left\langle \frac{\partial^2\psi}{\partial x\partial y}(\mathbf{0},0)\frac{\partial^2\psi}{\partial x\partial y}(\mathbf{0},t)\right\rangle$$
$$= \frac{1}{2\gamma}\int_{-\infty}^{\infty} dt \frac{\partial^4 C}{\partial x^2\partial y^2}(0,t) = \sqrt{\frac{\pi}{2}}\frac{u_0^2\tau}{\gamma\eta^2} = \sqrt{\frac{\pi}{2}}\mathrm{Ku}^2\mathrm{St}. \tag{5.42}$$

From Eq. (5.11) the collision rate in the two-dimensional case in the limit as $\mathrm{St} \to 0$ is

$$R_a = 4\sqrt{2\pi}a^2 n\frac{u_0}{\eta}. \tag{5.43}$$

The collision rate for $\mathrm{St} \gg 1$ is obtained from Eq. (5.29) and reads

$$R_g = 2^{7/4}\pi^{3/4}anu_0\sqrt{\gamma\tau} = 2^{7/4}\pi^{3/4}anu_0\mathrm{St}^{-1/2}. \tag{5.44}$$

We obtain that the collision rate as a function of the Stokes number in the two-dimensional model with the Gaussian correlation function is given by

$$R(\mathrm{Ku},\mathrm{St}) = R_a + \exp\left(-\frac{S\sqrt{2}}{\mathrm{Ku}^2\mathrm{St}\sqrt{\pi}}\right)R_g, \tag{5.45}$$

where S is a constant which depends on Ku, as explained above.

In the simulation the particles were initially uniformly distributed, and overlaying droplets were repositioned. Before counting collisions, we let the particles run for a time of order γ^{-1}, until velocity fluctuations relaxed. As explained in section 5.2, the particles collide when their separation falls below $2a$. Collisions may be counted using a number of efficient algorithms (see, e.g. [67]). The important issue here is to ensure that in a time interval Δt, which is used for numerical integration of the equation of motion (5.2), the collisions are not missed during one time step, and that the same particles do not collide at successive time steps. It can also be time-consuming to calculate the collision rate if it is necessary to consider systems of a large number of particles. Here, we only used a simple algorithm following distances between the particles at each time step. We used a small Δt to prevent missing collisions and repositioned particles after they collided. In the course of our simulation we calculated

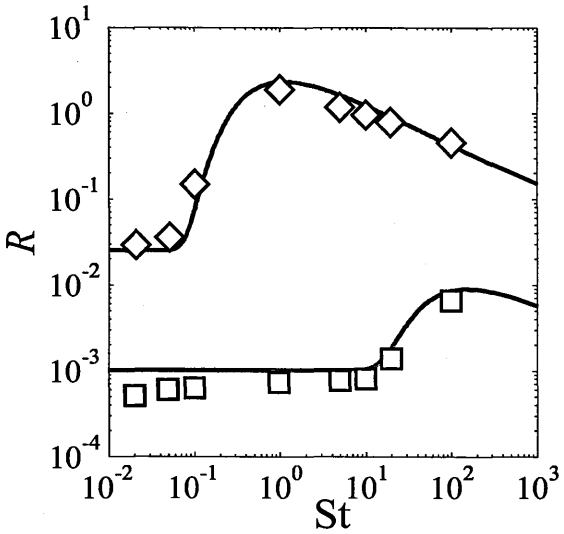

Figure 5.6: The collision rate as a function of the Stokes number, for two different values of the Kubo number. In the simulations we used $n = 10^3$, $a = 5 \times 10^{-4}$, $\eta = 0.1$, $\tau = 0.1$, and varied u_0 and γ: Ku $= 1$ (diamonds), Ku $= 0.04$ (boxes). The theoretical curves are given by Eq. (5.45), with S obtained from figure 5.5. For the case of small Ku, the Saffman-Turner result for the advective collision rate is an upper bound, since the flow fluctuates very rapidly.

the number of collisions at each time step R_i, which is the number of collisions per pair of particles. The collision rate for one test particle is then obtained as

$$R = \lim_{N_t \to \infty} \frac{2}{n(N_t \delta t)} \sum_{i=1}^{N_t \delta t} R_i, \tag{5.46}$$

where N_t is the number of time steps. We run several simulations with different realizations of the velocity field to produce a smooth average.

In Fig. 5.6 we show the comparison of our numerical results for the rate of collision R for a single particle with the theory given by Eq. (5.45) in the case of Ku $= 1$ and Ku $= 0.04$. The sharp increase of the collision rate is evident at St ≈ 1 for Ku $= 1$. For the case of a small Kubo number the increase occurs at a larger St. Also, in this case, the Saffman-Turner result for the advective collision rate is clearly an upper bound. This happens because the case of a small Kubo number corresponds to a rapidly fluctuating flow, so that the time-dependence is indeed important. The results at St ≈ 1 for our single-scale flow are very similar to the simulations using Navier-Stokes flows, reported in [26, 27], implying that multi-scale aspects of those simulations are

not essential in understanding the dramatic increase of the collision rate.

5.6 Application to clouds

In this section we try to estimate the collision rate in cumulus clouds. The calculations based on the result of Saffman and Turner gives a collision time of order several hours [1, 57], which is hard to reconcile with a rapid onset of rainfall from cumulus clouds. The properties of clouds are very variable and the sizes of visible moisture droplets have a large dispersion, but typically the average of the radius is approximately 10μm and the density is $n \approx 10^8\text{m}^{-3}$ [1]. According to Stokes's formula for the viscous drag on a sphere (2.36), $\gamma = 9\rho_f\nu/2\rho_p a^2$, where ν is the kinematic viscosity of air, ρ_p and ρ_f are the densities of water and air respectively. The properties of air vary with temperature and pressure, but we can take for typical values $\nu = 10^{-5}\text{m}^2/\text{s}$ and $\rho_f = 1.4\text{kg}/\text{m}^3$. The density of water is $\rho_p = 10^3\text{kg}/\text{m}^3$. Using these values we estimate $\gamma \approx 500\text{s}^{-1}$.

The turbulent motion is a multi-scale flow with an approximately power-law spectrum of spatial fluctuations of $\boldsymbol{u}(\boldsymbol{r}, t)$, as explained in chapter 2. The dissipation rate ϵ is highly variable between different clouds. Values of ϵ as high as $0.1\text{m}^3\text{s}^{-2}$ are observed in very unstable atmosphere [1], but could be smaller; this estimates the Kolmogorov scales $\eta \approx 3 \times 10^{-4}\text{m}$, $\tau \approx 10^{-2}\text{s}$ and $u_0 \approx 3 \times 10^{-2}\text{m}/\text{s}$ implying that $\text{St} \approx 0.2$.

We now estimate the collision rate using a gas-kinetic model. In the three-dimensional model the collision rate is $R_{\text{g}} = 16\sqrt{\pi/3}na^2\sqrt{\langle|\boldsymbol{v}|^2\rangle}$. Using the result of section 5.4 [see Eq. (5.26)], we obtain $\sqrt{\langle|\boldsymbol{v}|^2\rangle} \sim \text{St}^{-1/2}\, u_0$. Using the data above, this estimate gives a collision rate of $R_g \approx 5 \times 10^{-3}\text{s}^{-1}$ when $\text{St} \approx 1$ implying that the time scale of collisions is approximately 200s. This implies that rainfall can indeed be initiated on a timescale of a few minutes, provided that a sufficiently large part of the cloud has a turbulence intensity $\mathcal{I}$ which exceeds the threshold of forming caustics S.

5.7 Summary

In this chapter we have discussed quantitatively the collision rate of small spherical particles. When the inertia of the particles is small, the collision rate is given by the theory due to Saffman and Turner, with the result $R_a \sim a^d$ in d spatial dimensions. As the inertia of the particles increases, they may cluster, which is thought to be a dominant factor in a dramatic increase of the collision rate observed in numerical simulations. We have argued that the clustering mechanism is not sufficient to explain this increase and the fact that the collision rate remains high even for the particles with very large inertia. We have suggested that this increase is due to the formation of fold caustics in the velocity field of the particles, which cause their relative motion. The process of the formation of caustics has been shown to be equivalent to a noise-activated escape of a particle from the potential well. The collision rate contains a factor $\exp(-S/\mathcal{I})$, implying that when the intensity of turbulence $\mathcal{I}$ exceeds S, the collision rate increases drastically and remains high. Our estimates for the collision rate in the atmosphere using a gas-kinetic model can explain a rapid, of order a few minutes, initiation of rainfall from unstable cumulus clouds.

Part II

Motion of non-spherical particles

Chapter 6

Advection of small axisymmetric particles: textures and apparent singularities

Some parts of this chapter were published in the paper "Fingerprints of random flows?" by Wilkinson, Mehlig and Bezuglyy in Phys. Fluid. **21**, 043304, (2009). Numerical simulations were solely performed by the author of the thesis, the theory was developed in collaboration.

6.1 Introduction

In this chapter we consider the motion of small ellipsoidal particles advected in a moving incompressible fluid. The suspended particles align with their neighbours in a manner determined by the strain-rate of the flow. In a turbulent or randomly moving fluid the direction vector field of the axisymmetric particles forms complex textures (or patterns), illustrated by Fig. 6.1. We concentrate on two-dimensional textures, because it is hard to observe the direction field in three dimensions. The particles direction field is a non-oriented vector field in a two-dimensional space (by non-oriented, we mean that directions differing by π are equivalent). In such a field we might expect to see point singularities of the direction field of the type illustrated

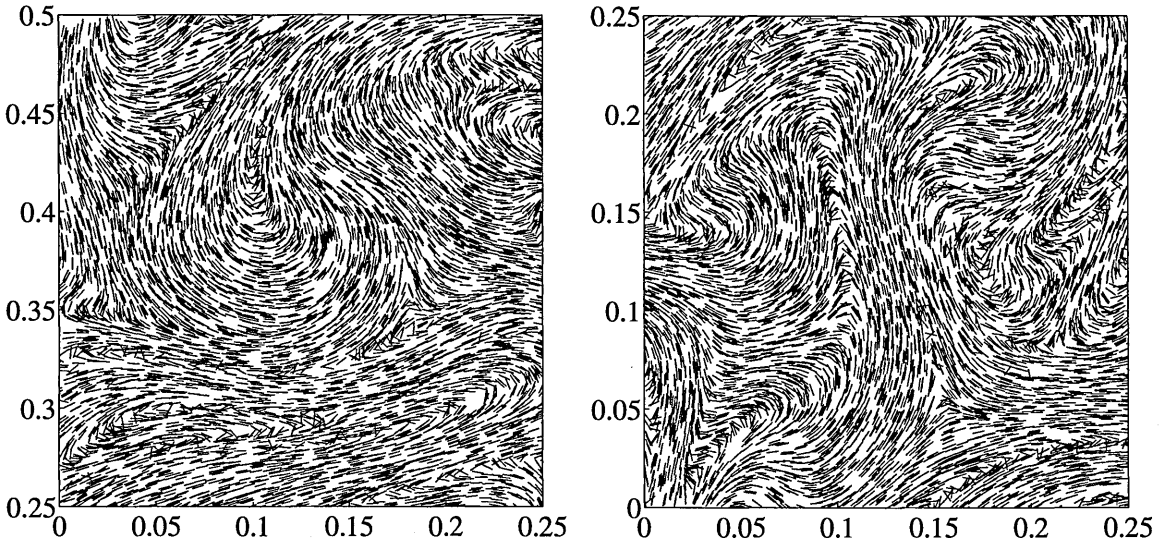

Figure 6.1: Simulations of the orientations of axisymmetric particles advected in a random incompressible flow in two dimensions. These appear to show singularities which are analogous to those occurring in fingerprint patterns, illustrated in Fig. 6.2. The simulations describe a dilute suspension of very small rod-like particles: here their sizes are exaggerated to make the textures visible. Details of the simulation are specified in the text below.

in Fig. 6.2, which are also present in fingerprint patterns [28] (where the patterns formed by ridges are another example of a non-oriented vector field in two dimensions). Such singularities of a non-oriented vector field are also observed in textures of liquid crystals [68] and lines of curvature in the vicinity of umbilical points of a surface [69].

The actual textures that we observe in Fig. 6.1 do indeed have structures which resemble the core and delta singularities of fingerprints. In this chapter we discuss the mechanism of the formation of such structures in the textures of rod-like particles. We remark that the singularities are characterized by a topological invariant, termed the Poincaré index, which is illustrated in Fig. 6.3, and topological arguments will be central to the discussion in this chapter. For a vector field in the plane, the Poincaré index of a closed curve is the number of 2π clockwise rotations of the vector field as the curve is traversed, also clockwise. Curves with a non-zero Poincaré index encircle a singularity of the field.

Suspensions of small anisotropic particles called rheoscopic fluids are often used for flow visualization [70, 71, 72]. This uses the principle that the intensity of scattering of light from a localized source will depend upon the orientation of the suspended

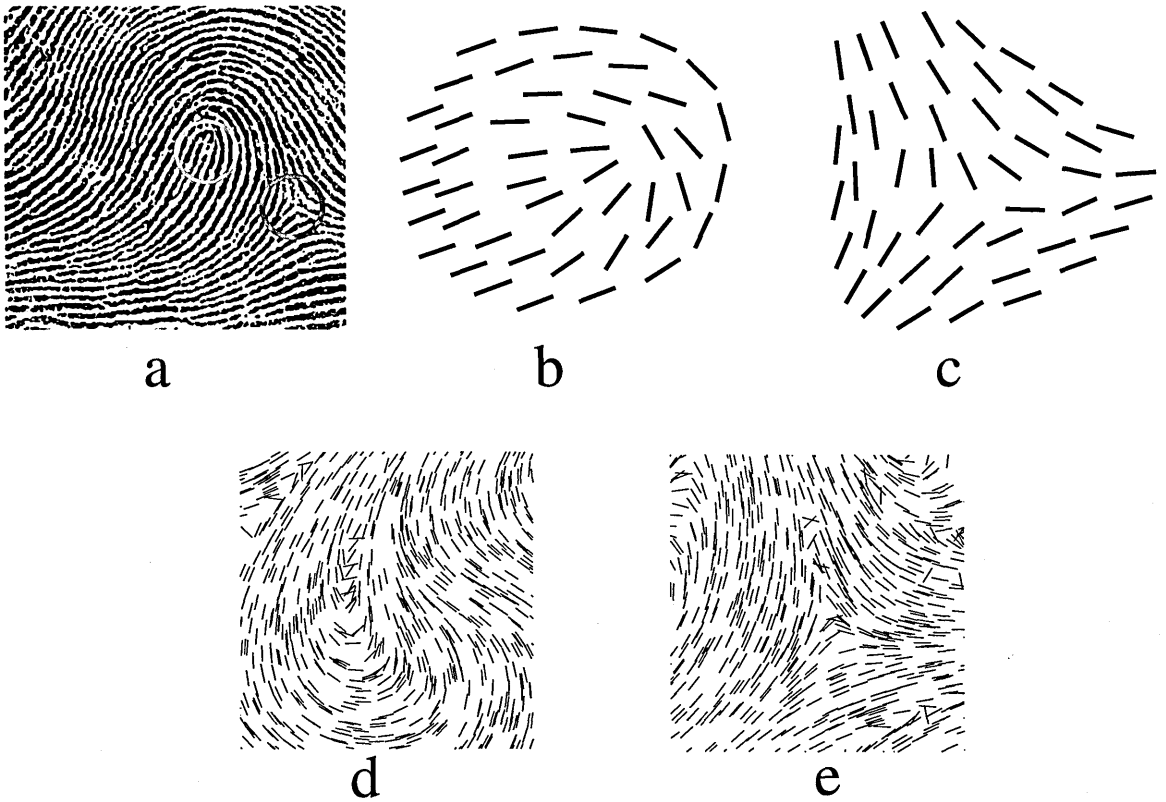

Figure 6.2: The textures illustrated in Fig. 6.1 have similarities with fingerprint patterns, such as those shown in panel **a** (taken from [28]), which contain two elementary point singularities of non-oriented vector fields in two-dimensions: in fingerprint patterns these are known as the 'core' (**b**) and the 'delta' (**c**). They are marked by red and green circles, respectively in panel **a**. Examples of these singularities as they appear in particle textures are shown in panels **d** and **e**, respectively.

particles. The information in this visualization can be enhanced by using light sources with different colours [36]. Here we show how the colours might be used to reveal information about the topology of the textures formed on the surface of the rheoscopic fluid. For illustrative purposes, we assume that the intensity of scattering from a particle at angle θ from a source at angle ϕ (relative to a line perpendicular to the particle's axis of symmetry) is proportional to $\cos^2(\theta - \phi)$. This approximation can be justified when the particles are short compared to the wavelength of the light (see also the discussion in chapter 7). Accordingly, if three light sources of red (R), green (G) and blue (B) colours are arranged at angle ϕ equal to 0, $2\pi/3$ and $4\pi/3$, respectively, then the colour C reflected by the particle at angle θ is an admixture of the primary

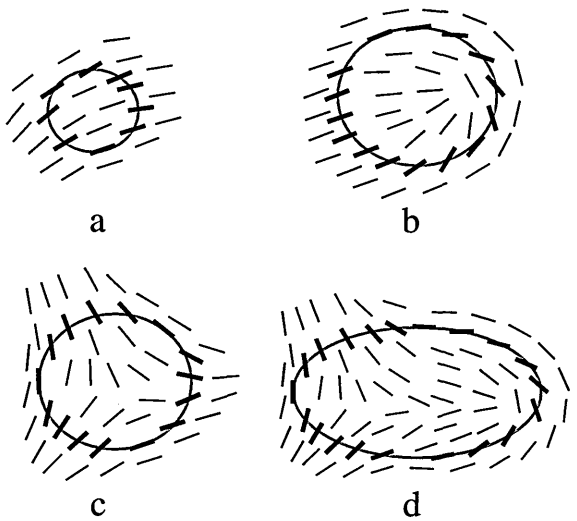

Figure 6.3: Given a non-oriented vector field $\mathbf{n}(\boldsymbol{r})$ in two dimensions and a closed curve $\mathcal{C}$, the Poincaré index $N(\mathcal{C})$ is defined as the number of multiples of 2π by which the direction of $\mathbf{n}$ rotates (in the clockwise direction) as $\mathcal{C}$ is traversed (also clockwise). For a non-oriented vector field, such as the direction of the particles, the Poincaré index may take half-integer values. (**a**) For a field without singularities, $N = 0$. (**b**) For a curve which encircles a core, $N = \frac{1}{2}$. This singularity can be regarded as having a 'charge' of $N = \frac{1}{2}$. (**c**) For a curve which encircles a delta, $N = -\frac{1}{2}$. (**d**) For a curve which encircles more than one singularity, their charges are summed. This curve encircles a combination of a core and delta which is termed a 'loop'. For this case $N = -\frac{1}{2} + \frac{1}{2} = 0$.

colours given by

$$C = R\cos^2(\theta) + G\cos^2(\theta - 2\pi/3) + B\cos^2(\theta - 4\pi/3)\ . \tag{6.1}$$

Singularities with a non-zero Poincaré index in this case could be detected by examining the colours along a closed path. If the colours cycle through all three primaries as the path is traversed, this path must contain a singularity of the particles directions. The sign of the Poincaré index is determined by the order in which the primary colours cycle ($R \rightarrow G \rightarrow B$ or $R \rightarrow B \rightarrow G$). Alternatively, if the particles are organized in a vortex, then each primary colour is repeated twice on traversing a path ($R \rightarrow G \rightarrow B \rightarrow R \rightarrow G \rightarrow B$) and the Poincaré index in this case is $+1$ (see Fig. 6.4). In Fig. 6.5 we demonstrate the potential of this approach by re-displaying the textures in Fig. 6.1 using Eq. (6.1). The physics of scattering or reflection from anisotropic particles is complex, but this illustration is indicative of what can be seen

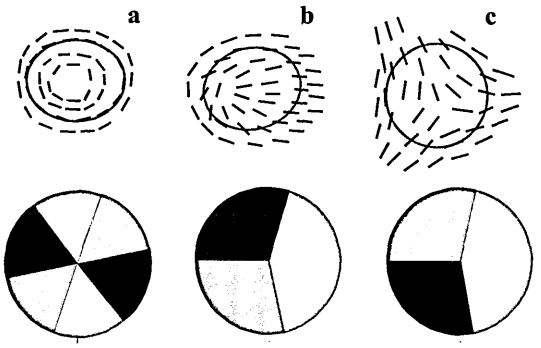

Figure 6.4: (**a**) Shows the direction field around a vortex with Poincaré index 1 and the corresponding colour texture cycling through $R \to G \to B \to R \to G \to B$. Also shows the same for a 'core' singularity with index $\frac{1}{2}$ (**a**) and for a 'delta' singularity with index $-\frac{1}{2}$ (**b**), respectively.

with different coloured light sources. We remark that the two-dimensional flow can be realized in a thin layer of the rheoscopic fluid floating upon a denser fluid which is stirred gently. We shall return to the experimental studies of rheoscopic visualizations in the next chapter.

This chapter is organized as follows. In section 6.2 we discuss the solution of equation of motion (2.54) describing the dynamics of the orientation of the particle. Jeffery [45] obtained the solution for a simple shear flow, showing that ellipsoids with a finite aspect ratio undergo a tumbling motion. In this thesis we use a general solution of Jeffery's nonlinear equation of motion in terms of a companion linear equation. The same solution is given by Szeri [29], who refers to earlier works [46, 73] which contain related ideas, but not the full solution. The solution is given in terms of the matrix describing the history of the flow along the particle trajectory, which we term the 'pseudomonodromy matrix'. It can be shown that in a generic complex flow, at long times, the particle orientation is asymptotic to the direction of the eigenvector of the pseudomonodromy matrix corresponding to the largest eigenvalue.

Section 6.3 discusses the extent to which the solution we describe in section 6.2 can exhibit singularities. We start by presenting an argument showing that the direction field cannot have any singularities. This implies that the Poincaré index for any curve is zero, and is hard to reconcile with the appearance of Figs. 6.1 and 6.2. However, we show that the singularities are approached in an asymptotic sense. From numerical

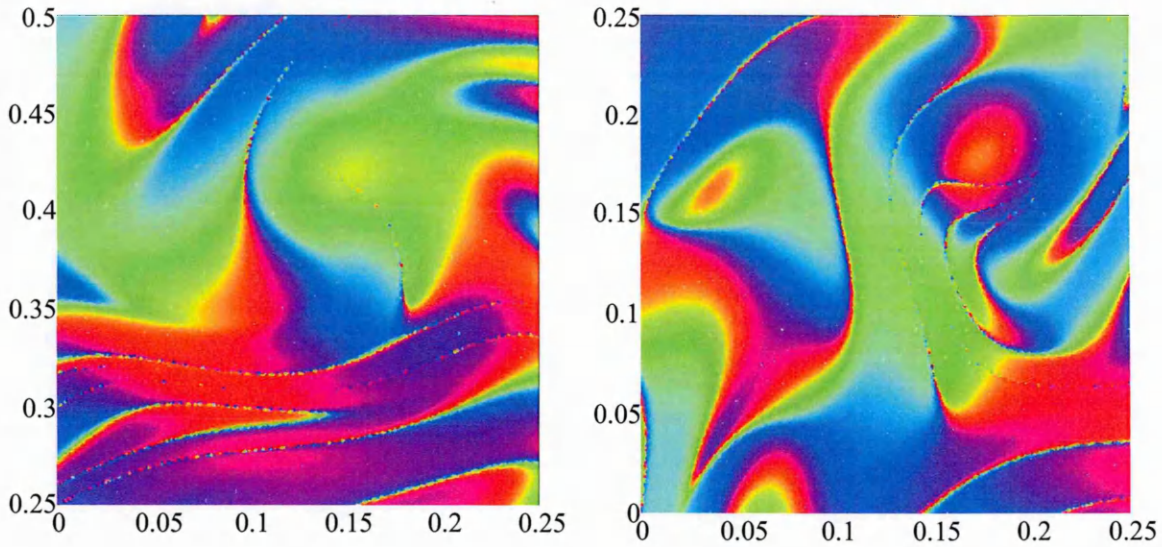

Figure 6.5: The textures shown in Fig. 6.1 colour-coded using Eq. (6.1) to illustrate how they can be visualized using coloured light sources.

simulations we observe that the eigenvector field, to which the particles orientation field is asymptotic, can have a non-zero Poincaré index implying that the asymptotic correspondence between these vector fields breaks down somewhere. We show that it fails along certain lines, which we term 'scar lines', where the orientation vector of the particles abruptly changes its direction by π. The scar line emerges and sharpens as the two vector fields asymptotically approach each other. As the scar line sharpens, there is fewer particles which lie in the region where the direction differs from the asymptotic value. The result is that the scar line disappears. At the ends of the scar line there remains a point singularity of the type illustrated in Fig. 6.2.

In section 6.4 we consider the behaviour of the solution of the equation of motion discussed in section 6.2 in the long-time limit. The solution appears to be incompatible with a statistically stationary limit, but this is shown not to be the case. We also show that the probability distribution of the gradient of the angle has an approximately log-normal distribution. This is consistent with the existence of apparent singularities in the particles textures, where the angle of the particles changes very abruptly.

In section 6.5 we briefly discuss the textures in three-dimensional flows and in section 6.6 we summarize the results of this chapter.

We stress that throughout this thesis non-spherical particles in the fluid are as-

sumed to be so small and so dilute that they do not influence the fluid flow and are unlikely to come into contact with each other (the sizes of the particles in Fig. 6.1 and other figures have been grossly exaggerated to make the patterns visible). This assumption is valid for most applications of rheoscopic suspensions, which reflect light effectively even at very small volume fractions. It is natural to question whether our results have any relevance to nematic liquid crystals, which consist of rod-like molecules. The orientation vector field in liquid crystals is mainly a consequence of the interaction between the molecules. We found that there is no apparent connection between the dilute limit, where the particle orientation satisfies a differential equation, and the physics of liquid crystals, where the orientation field minimizes an energy functional, known as the Oseen-Frank potential [68].

The discussion throughout this chapter uses numerical simulations for illustrative purposes. The simulations were done by integrating Eqs. (2.45) and (2.54) using the first-order Euler method. The aspect ratio of the particle α is a parameter in Eq. (2.54). The simulations here were done with $\alpha \to \infty$ which corresponds to very thin rods. In the course of the discussion we shall show that qualitatively the results are independent from the value of the aspect ratio. In this chapter we consider the case when the initial orientation field of the particles is non-random and continuous. In particular, in our simulations, the particles were initially oriented in the same direction. For the model of the flow we used an incompressible two-dimensional single-scale flow with the stationary, isotropic and translationally invariant statistics, with the Gaussian correlation function (2.26). The parameters of the velocity field were $u_0 = 1.0$, $\eta = 0.1$ and $\tau = 0.1$ in all cases.

6.2 Equation of motion and its solution

The configuration of an axisymmetric particle advected in a flow can be specified by the position $\boldsymbol{r}(t)$ of its mid-point, and by a unit vector $\mathbf{n}(t)$ aligned with the particle's axis of symmetry. We recall (see section 2.2) that the equation of motion for the

position is simply advection and the dynamics of $\mathbf{n}$ is given by the equation

$$\dot{\mathbf{n}} = \mathbf{B}\mathbf{n} - \mathbf{n}(\mathbf{n} \cdot \mathbf{B}\mathbf{n}), \tag{6.2}$$

where $\mathbf{B}$ is a 'weighted' strain matrix:

$$\mathbf{B} = \frac{D_\alpha + 1}{2}\mathbf{A} + \frac{D_\alpha - 1}{2}\mathbf{A}^T. \tag{6.3}$$

Here $\mathbf{A}$ is the matrix of derivatives of the flow, $A_{ij} = \partial u_i / \partial r_j$, and D_α is a parameter which depends on the aspect ratio of the particle [see Eq. (2.53)] and ranges from -1 (corresponding to a thin disk in the three-dimensional case) to 1 (corresponding to a thin rod). We now consider how a solution of the equation of motion (6.2) may be obtained. The solution which we describe below was first given in [29], but a very brief derivation is given below in order to establish notations.

We can solve the non-linear equation (6.2) in terms of the solution of an auxiliary problem, which is linear. Specifically, we solve the equation

$$\dot{\boldsymbol{d}} = \mathbf{B}(t)\boldsymbol{d} \tag{6.4}$$

to determine a vector $\boldsymbol{d}(t)$. Here $\mathbf{B}(t)$ is the matrix $\mathbf{B}$ evaluated at the position reached by the particle at time t. This equation is solved with the initial condition $\boldsymbol{d}(t_0) = \mathbf{n}_0$, where $\mathbf{n}_0$ is the initial orientation of the particle at time t_0. Now, we multiply $\boldsymbol{d}(t)$ by a scalar $a(t)$, chosen such that $\mathbf{n}(t) = a(t)\boldsymbol{d}(t)$ is a unit vector. We find that this normalized vector does indeed satisfy Eq. (6.2). We therefore have a solution of the nonlinear equation for $\mathbf{n}(t)$ in the form

$$\mathbf{n}(t) = \frac{\boldsymbol{d}(t)}{|\boldsymbol{d}(t)|}\,. \tag{6.5}$$

This is an exact and completely general solution for the orientation, in terms of the solution of a companion linear problem given by Eq. (6.4).

Now, we determine a matrix $\mathbf{M}(t)$ which is the solution of

$$\frac{d}{dt}\mathbf{M} = \mathbf{B}[\boldsymbol{r}(t), t]\mathbf{M} \tag{6.6}$$

with the initial condition $\mathbf{M}(0) = \mathbf{I}$ (the identity matrix). Given this matrix, the solution of Eq. (6.6) is $\boldsymbol{d}(t) = \mathbf{M}(t)\boldsymbol{d}_0$, for any choice of the initial orientation $\boldsymbol{d}_0$, so that a single solution suffices for all initial directions. Let $\mathbf{M}(\boldsymbol{r}, t, t_0)$ be the solution of Eq. (6.6) for a particle which reaches position $\boldsymbol{r}$ at time t, having started at $\boldsymbol{r}_0$ at time t_0. Now define $\mathbf{n}(\boldsymbol{r}_0)$ as the initial direction (at time t_0) of the particle, expressed as a function of the initial position $\boldsymbol{r}_0$. In this most general case the exact solution becomes

$$\mathbf{n}(\boldsymbol{r}, t) = \frac{\mathbf{M}(\boldsymbol{r}, t, t_0)\mathbf{n}(\boldsymbol{r}_0, t_0)}{|\mathbf{M}(\boldsymbol{r}, t, t_0)\mathbf{n}(\boldsymbol{r}_0, t_0)|} \,. \tag{6.7}$$

In the case of rod-like particles, with $D_\alpha = 1$, the matrix $\mathbf{B}(t)$ is equal to the velocity-gradient matrix $\mathbf{A}(t)$. In this case the matrix $\mathbf{M}(t)$ has a simple physical interpretation, and in the following we use $\mathbf{M}_A(t)$ to denote the solution of Eq. (6.2) in the special case where $\mathbf{B} = \mathbf{A}$. Let us consider the trajectories of two particles advected by the flow: a reference particle with trajectory $\boldsymbol{r}(t)$, and a nearby particle with trajectory $\boldsymbol{r}(t) + \delta\boldsymbol{r}(t)$. To the leading order in $|\delta\boldsymbol{r}|$, the separation vector is determined by the matrix $\mathbf{M}_A(t)$: $\delta\boldsymbol{r}(t) = \mathbf{M}_A(t)\,\delta\boldsymbol{r}(0)$. In the language of dynamical systems theory, a matrix with this property is termed a 'monodromy' matrix. We consider volume preserving flows, so that $\mathrm{tr}[\mathbf{A}(t)] = 0$. From Eq. (6.3), the matrix $\mathbf{B}(t)$ also has the property that $\mathrm{tr}[\mathbf{B}(t)] = 0$, as if it were the velocity-gradient of some fictitious volume-preserving flow. We then obtain that $\det[\mathbf{M}(t)] = 1$. We will therefore refer to the solution $\mathbf{M}(t)$ of Eq. (6.6) as the 'pseudomonodromy' matrix of the flow. For the case of rod-like particles, with $D_\alpha = 1$, it is the same as the true monodromy matrix of the flow.

The degree to which the solution can be presented in a closed form depends upon the specifics of the flow field. First, we comment on the exactly solvable case of a time-independent flow with constant velocity gradient $\mathbf{A}$, because this case already exhibits solutions showing both alignment and tumbling. In this case the matrix $\mathbf{B}$ is

also constant, and the solution of the linear auxiliary Eq. (6.4) is

$$\boldsymbol{d}(t) = \mathbf{M}(t)\boldsymbol{d}_0 = \exp(\mathbf{B}t)\boldsymbol{d}_0. \tag{6.8}$$

The matrix $\exp(\mathbf{B}t)$ may be expressed in terms of the eigenvalues and eigenvectors of $\mathbf{B}$. The matrix $\mathbf{B}$ is typically non-symmetric, and correspondingly its eigenvectors need not be orthogonal. The behaviour of the solution is determined by the eigenvalues λ_i of $\mathbf{B}$. We consider incompressible flows, implying that $\mathrm{tr}[\mathbf{B}] = 0$, so that the eigenvalues of $\mathbf{B}$ sum to zero. We discuss both the three-dimensional and two-dimensional cases below.

Apart from degenerate cases, the spectrum of $\mathbf{B}$ in the three-dimensional case may take one of three forms:

1. Eigenvalues are real and distinct, with at least one of them positive. The axis of the particle aligns with the eigenvector $\boldsymbol{u}_+$ corresponding to the largest eigenvalue λ_+ of $\mathbf{B}$.

2. There may be a real and positive eigenvalue λ_+ and a complex pair with negative real parts. In this case the axis also aligns with the dominant eigenvector $\boldsymbol{u}_+$.

3. There may be two complex conjugate eigenvalues with positive real parts (so that the real eigenvalue is negative), with complex conjugate eigenvectors. When these two eigenvectors are combined with complex-conjugate coefficients, the resulting real vector lies in a plane. In the long-time limit the vector $\boldsymbol{d}(t)$ spirals outwards in this plane. This case corresponds to a tumbling motion of the particle.

In the case of a two-dimensional incompressible flow, the matrix $\mathbf{B}$ may have either two reciprocal real eigenvalues (hyperbolic case), or else two complex conjugate eigenvalues which lie on the unit circle (elliptic case). In the hyperbolic case the vector $\boldsymbol{d}(t)$ comes into alignment with the eigenvector of $\mathbf{B}$ which corresponds to the positive eigenvalue. In the elliptic case, where $\mathbf{B}$ has purely imaginary eigenvalues $\pm i\omega$, the pseudomonodromy matrix $\mathbf{M}(t)$ can be expressed in terms of a normal form

representing rotation in the plane, in which case the vector $\boldsymbol{d}(t)$ rotates reversing direction rapidly at times separated by π/ω.

6.2.1 Asymptotic form of the solution

Let λ_+ and $\boldsymbol{u}_+$ be respectively the eigenvalue of $\mathbf{M}$ with the largest magnitude and the corresponding eigenvector, normalized to unit length. We term these the dominant eigenvalue and eigenvector. The other eigenvalue and eigenvector are denoted λ_- and $\boldsymbol{u}_-$ and are termed subdominant. We assume that the random flow $\boldsymbol{u}(\boldsymbol{r},t)$ has a positive Lyapunov exponent Λ implying that the infinitesimal separation between fluid elements tend to grow exponentially. This is a typical situation in a generic time-dependent flow which does not decay. In this case the elements of $\mathbf{M}(\boldsymbol{r},t,t_0)$ tend to increase exponentially as a function of $t-t_0$ (note that this assumptions might not be valid in the case of simpler flows such as a recirculating flow). Correspondingly, the ratio $|\lambda_+/\lambda_-|$ is expected to increase exponentially (recall that $\lambda_+\lambda_- = 1$). If $|\lambda_+/\lambda_-| \gg 1$, applying the matrix $\mathbf{M}$ to almost any vector is expected to result in a vector which is nearly aligned with $\boldsymbol{u}_+$. This can be shown as follows. Let us write the initial direction as

$$\mathbf{n}_0 = \alpha_+\boldsymbol{u}_+ + \alpha_-\boldsymbol{u}_-. \tag{6.9}$$

Applying the matrix $\mathbf{M}$ produces the vector $\mathbf{M}\mathbf{n}_0 = \alpha_+\lambda_+\boldsymbol{u}_+ + \alpha_-\lambda_-\boldsymbol{u}_-$. Since the ratio of eigenvalues grows exponentially, we conclude that $\mathbf{M}\mathbf{n}_0 \sim \boldsymbol{u}_+$ for almost all vectors as $t-t_0$ increases. This is illustrated by the simulation in Fig. 6.6.

6.3 Apparent singularities of the direction field

Now, we consider whether it is possible for the vector field $\mathbf{n}(\boldsymbol{r},t)$ to have singularities, where $\mathbf{n}$ changes discontinuously as a function of $\boldsymbol{r}$. First we show (section 6.3.1) that it is not possible for $\mathbf{n}(\boldsymbol{r},t)$ to have singularities in a strict sense. It is however possible that the field could approach a singularity in some asymptotic sense. Accordingly, we also consider (section 6.3.2) whether the eigenvector field $\boldsymbol{u}_+(\boldsymbol{r},t)$, to which $\mathbf{n}(\boldsymbol{r},t)$ is

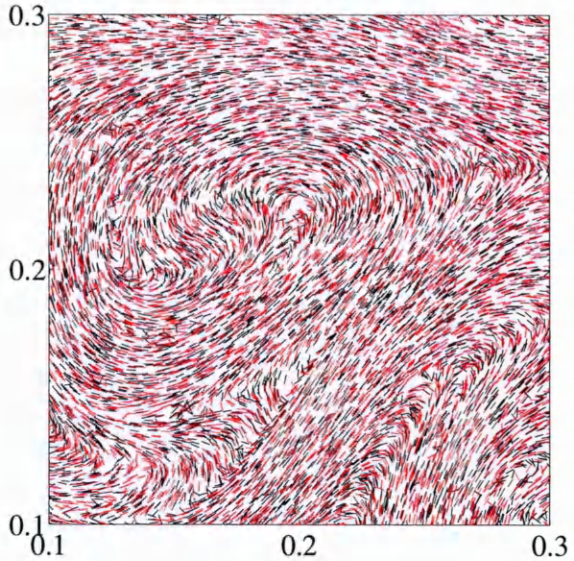

Figure 6.6: Illustrating the correspondence between the particle direction field $\mathbf{n}(\boldsymbol{r}, t)$ (black) and the eigenvector field $\boldsymbol{u}_+(\boldsymbol{r}, t)$ (red) at large time.

asymptotic, has any singularities. Although $\boldsymbol{u}_+(\boldsymbol{r}, t)$ does not contain singularities, we show that it can have a non-trivial topology. There are regions where the pseudomonodromy matrix $\mathbf{M}$ is elliptic (with conjugate eigenvalues on the unit circle), so that the dominant eigenvector $\boldsymbol{u}_+$ is not defined. We term these regions of rotational flow 'gyres'. We find that the Poincaré index of the eigenvector $\boldsymbol{u}_+$ around the boundary of a gyre can be non-zero. In sections 6.3.3 and 6.3.4 we consider how the smooth field $\mathbf{n}(\boldsymbol{r}, t)$ can be asymptotic to the topologically non-trivial field $\boldsymbol{u}_+(\boldsymbol{r}, t)$.

6.3.1 Absence of singularities

For any finite value of $t - t_0$, the pseudomonodromy matrix $\mathbf{M}(\boldsymbol{r}, t, t_0)$ is a smooth function of the final position of the trajectory, $\boldsymbol{r}$. The solution (6.7) can therefore only be discontinuous if the initial direction field is discontinuous, or if the denominator $|\mathbf{M}\mathbf{n}_0|$ is equal to zero, which is only possible if there are points where $\det(\mathbf{M}) = 0$. This is not possible, since we consider area-preserving flows, where $\det(\mathbf{M}) = 1$. If the initial direction vector field $\mathbf{n}_0(\boldsymbol{r})$ is non-singular, we conclude that the direction field $\mathbf{n}(\boldsymbol{r}, t)$ remains non-singular for all times. Because the vector field generated by Eq. (6.7) is smooth, the Poincaré index of this field is zero for any closed curve, in apparent contradiction to the simulations shown in Fig. 6.1.

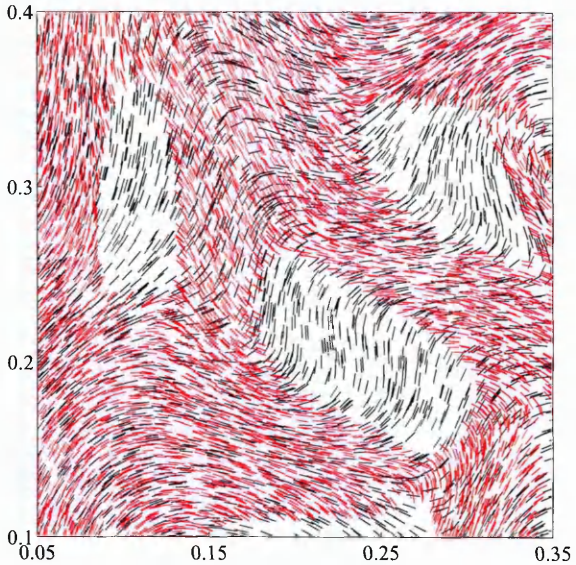

Figure 6.7: Eigenvector field $\boldsymbol{u}_+(\boldsymbol{r},t)$ (red) and particle direction field $\mathbf{n}(\boldsymbol{r},t)$ (black) at small time $t-t_0$. The regions where there are no red vectors arise because the eigenvector field of the dominant eigenvalue of the pseudomonodromy matrix $\mathbf{M}(\boldsymbol{r},t,t_0)$ is undefined in regions (which we term 'gyres') where $\mathbf{M}(\boldsymbol{r},t,t_0)$ is elliptic. Note that at small $t-t_0$ the gyres occupy a large fraction of the area and have simple boundaries. In this figure it can be seen that two of the gyres have non-zero Poincaré index.

6.3.2 Topology of the eigenvector field

We have shown that the direction field $\mathbf{n}(\boldsymbol{r},t)$ is asymptotic to the field of eigenvectors, $\boldsymbol{u}_+(\boldsymbol{r},t)$. We shall see that the latter field has a non-trivial topology.

The only type of singularity of the eigenvector field which is possible is where the pseudomonodromy matrix is equal to the identity matrix. It is a co-dimension three condition for the monodromy matrix to have this form, so it is non-generic in the two-dimensional problem which we consider. There is, however, another way in which the eigenvector field $\boldsymbol{u}_+(\boldsymbol{r},t)$ can have non-trivial topology.

In an area-preserving flow there will be regions of the plane, where the eigenvalues are complex and have the same magnitude, so that $\boldsymbol{u}_+$ is undefined. We refer to these regions where the normal form of $\mathbf{M}(\boldsymbol{r},t)$ is a rotation as 'gyres'. Each gyre is surrounded by a boundary. We find that the Poincaré index of the field $\boldsymbol{u}_+$ on the boundary of a gyre may not be equal to zero (two examples are illustrated in Fig. 6.7). This appears to contradict the result that $\mathbf{n}$ is asymptotic to $\boldsymbol{u}_+$, because we have seen that the Poincaré index of $\mathbf{n}$ is always zero.

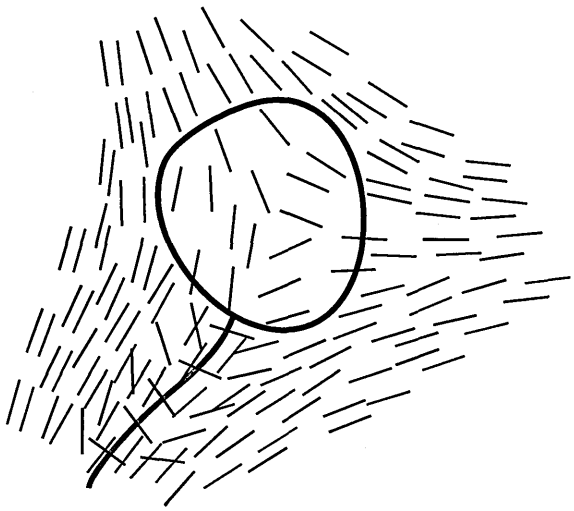

Figure 6.8: The direction vector $\mathbf{n}$ (black lines) is asymptotic to the vector field of eigenvectors $\boldsymbol{u}_+$ (red lines). The vector field $\boldsymbol{u}_+$ is undefined in 'gyres', where the normal form of the pseudomonodromy matrix is a rotation. The Poincaré index of the field $\boldsymbol{u}_+$ on the boundary of the gyre need not be equal to zero, whereas the Poincaré index of $\mathbf{n}$ is zero. In these cases the field $\mathbf{n}$ rotates by π in the vicinity of one or more 'scar lines' (green).

6.3.3 Asymptotic singularities of the direction field

We have seen that $\mathbf{n}(\boldsymbol{r}, t)$ is non-singular, but that it is asymptotic to a vector field $\boldsymbol{u}_+(\boldsymbol{r}, t)$ which may be topologically non-trivial. One way to resolve this contradiction is to assume that the field $\boldsymbol{u}_+(\boldsymbol{r}, t)$ has become trivial by the time $\mathbf{n}(\boldsymbol{r}, t)$ approaches it, due to gyres with opposite topological charges coalescing. Our numerical studies show that this is not a sufficient explanation.

There is, however, another way to resolve this apparent contradiction which is both more interesting and which does lead to an explanation of the textures seen in Fig. 6.1. Let us consider the set of points where $\mathbf{n}$ need not be asymptotic to $\boldsymbol{u}_+$. There are two ways in which this can occur. Both lead to structures which we term 'scar lines'.

In Eq. (6.9) we have expressed the initial direction field in terms of the eigenvectors of the pseudomonodromy matrix. The assumption that the Lyapunov exponent of the flow is positive implies that at most positions the ratio of eigenvalues grows exponentially with time and $\mathbf{n}$ aligns increasingly closely with $\boldsymbol{u}_+$. There are two ways in which this alignment can break down, leading to two types of scar lines:

1. **Type I scar lines.**

The direction field $\mathbf{n}$ need not approach $\boldsymbol{u}_+$ when α_+ is sufficiently small. The locus where $\alpha_+ = 0$ forms a set of lines in the plane, and as these lines are crossed, the direction of $\mathbf{n}$ rotates by $\pm\pi$. We term these lines 'type I scar lines'. The vector $\mathbf{n}$ differs significantly from $\boldsymbol{u}_+$ when $|\alpha_+| \exp(\Lambda|t - t_0|)$ is of order unity. This region where the direction flips therefore becomes vanishingly small at $t - t_0 \to \infty$. Accordingly, we can think of the scars lines as 'healing over', i.e. becoming invisible.

These scar lines must terminate at gyres. Fig. 6.8 is a schematic illustration the fields $\mathbf{n}$ and $\boldsymbol{u}_+$ in the vicinity of a charged gyre and its associated scar line. Fig. 6.9 shows type I scar lines in our numerical simulations.

2. **Type II scar lines**

Our argument that $\mathbf{n}$ aligns with $\boldsymbol{u}_+$ also fails if the eigenvalue ratio $|\lambda_+/\lambda_-|$ does not increase. The eigenvalue ratio is small in the vicinity of the gyres. The area of the gyres must decrease exponentially as $t - t_0$ increases. Generically, the gyres will be stretched and folded, as well as decreasing in area. In the long-time limit, the gyres occur in the form of very narrow strips where $|\mathrm{tr}(\mathbf{M})| \leq 2$. Upon crossing this strip, the sign of λ_+ changes, and correspondingly the vector $\mathbf{M}\,\mathbf{n}_0$ smoothly reverses direction. This implies that the direction of $\mathbf{n}$ reverses on crossing these narrow gyres: these are the type II scar lines.

6.3.4 Disappearance of scar lines and emergence of point singularities

The width of the region around a scar line where the fields $\mathbf{n}$ and $\boldsymbol{u}_+$ are significantly misaligned shrinks as $t - t_0 \to \infty$. As this region shrinks, eventually there is a small probability that any particle actually lies in the region where these vectors are misaligned. In this case, for all practical purposes the scar line has disappeared. Consider a loop which encircles the end of a scar line. Initially the Poincaré index of $\mathbf{n}$ about this loop is zero. When the angle change of $\pm\pi$ associated with crossing the scar line disappears, the Poincaré index of the circuit becomes $N = \pm\frac{1}{2}$. The

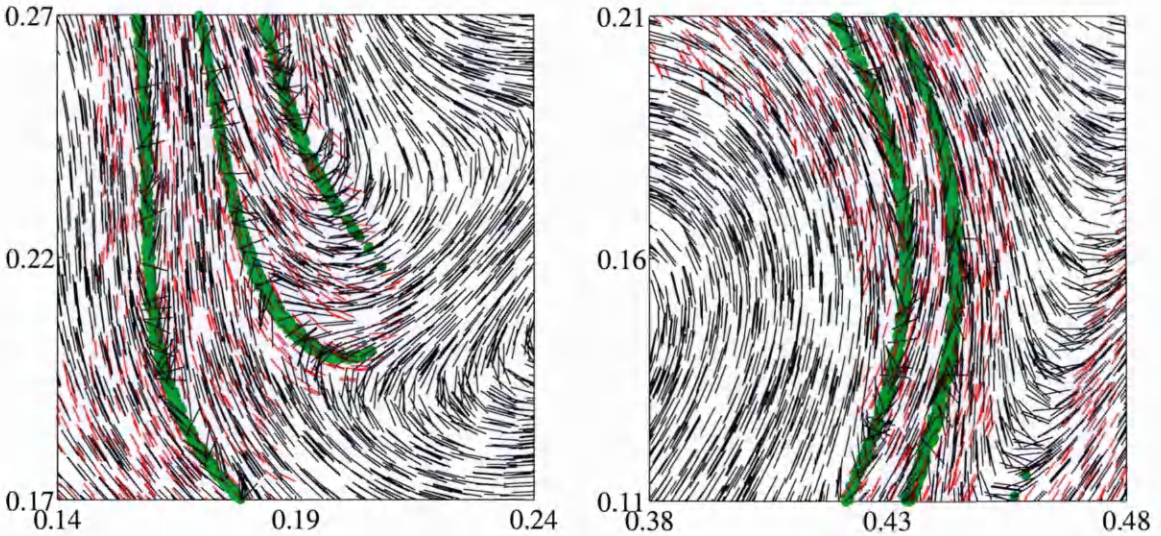

Figure 6.9: Numerical examples of type I scar lines. The particles directions $\mathbf{n}$ are shown in black, eigenvector $\boldsymbol{u}_+$ is shown in red, and the position of the scar line is indicated by a sampling of points where $|\alpha_+| < 10^{-2}$ (green). The direction of the particles is seen to flip around in the vicinity of the scar line.

disappearance of the scar line is therefore associated with the emergence of a point singularity at the positions where the ends of this line were located. This is illustrated schematically in Fig. 6.10, and by the numerical simulations in Fig. 6.11. This effect gives rise to the apparent singularities seen in Fig. 6.1.

6.3.5 A remark about eigenvector directions

We conclude this section by remarking that the eigenvectors $\boldsymbol{u}_+$ and $\boldsymbol{u}_-$ become co-linear on the boundary of the gyre. This observation can be understood using the following argument. On the boundary of the gyre, the matrix $\mathbf{M}$ only has one eigenvalue (which may be $+1$ or -1). The set of 2×2 matrices satisfying $\det \mathbf{M} = 1$ has three parameters, and if the eigenvalues are constrained to be $\lambda = 1$ (say), it becomes a two-parameter family of matrices. We now identify a parametrization of this family. Consider the eigenvalue equation, $\mathbf{F}\boldsymbol{u} = \lambda \boldsymbol{u}$, for matrices of the Jordan form

$$\mathbf{F}(\kappa) = \begin{pmatrix} 1 & \kappa \\ 0 & 1 \end{pmatrix} . \tag{6.10}$$

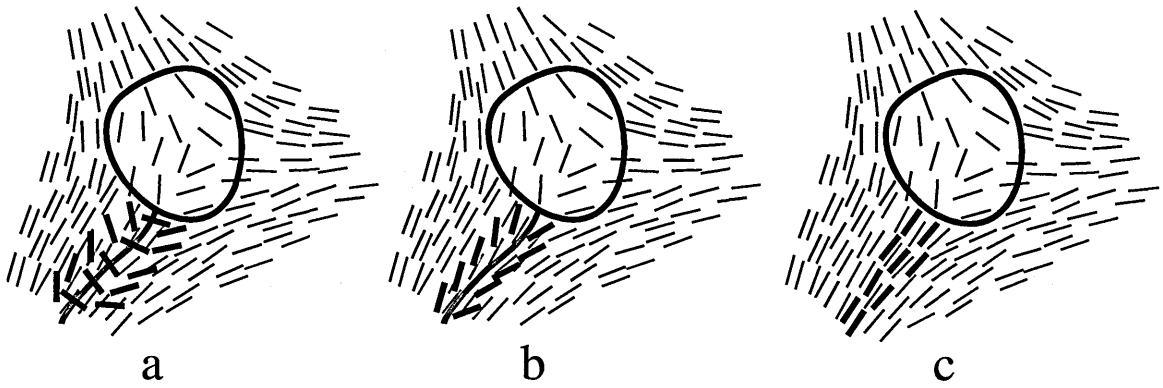

Figure 6.10: (**a**) The particle direction (black) is a smooth vector field containing a scar line which ends on the boundary of a gyre. As time increases, the scar line narrows (**b**). When the scar line has narrowed to the extent that it does not include the actual position of any particle, it disappears (**c**). This leaves a point singularity at the end of the scar line: in this case a delta. In practice, the picture is more complex because the positions of the gyre and the scar line both change as time increases.

These are a one parameter family of matrices which have only one eigenvector, $\boldsymbol{u} = (1, 0)$, and one eigenvalue, $\lambda = 1$. If $\mathbf{R}$ is a rotation matrix

$$\mathbf{R}(\theta) = \begin{pmatrix} \cos\theta & \sin\theta \\ -\sin\theta & \cos\theta \end{pmatrix} \tag{6.11}$$

we see that we can generate a two-parameter family of 2×2 matrices

$$\mathbf{M}(\theta, \kappa) = \mathbf{R}^{-1}(\theta)\mathbf{F}(\kappa)\mathbf{R}(\theta) \tag{6.12}$$

which have only one eigenvalue, $\lambda = 1$. By construction of the matrix $\mathbf{M}(\theta, \kappa)$ we can show that this two parameter family spans the set of 2×2 matrices with only one eigenvalue, $\lambda = 1$. But we have seen that these matrices have only one eigenvector, namely $\boldsymbol{u} = \mathbf{R}(\theta)(1, 0)^{\mathrm{T}}$. We conclude that as we approach the boundary of a gyre from the outside, the two eigenvectors $\boldsymbol{u}_+$ and $\boldsymbol{u}_-$ become co-linear. This implies that α_+ and α_- both diverge as we approach the boundary of the gyre.

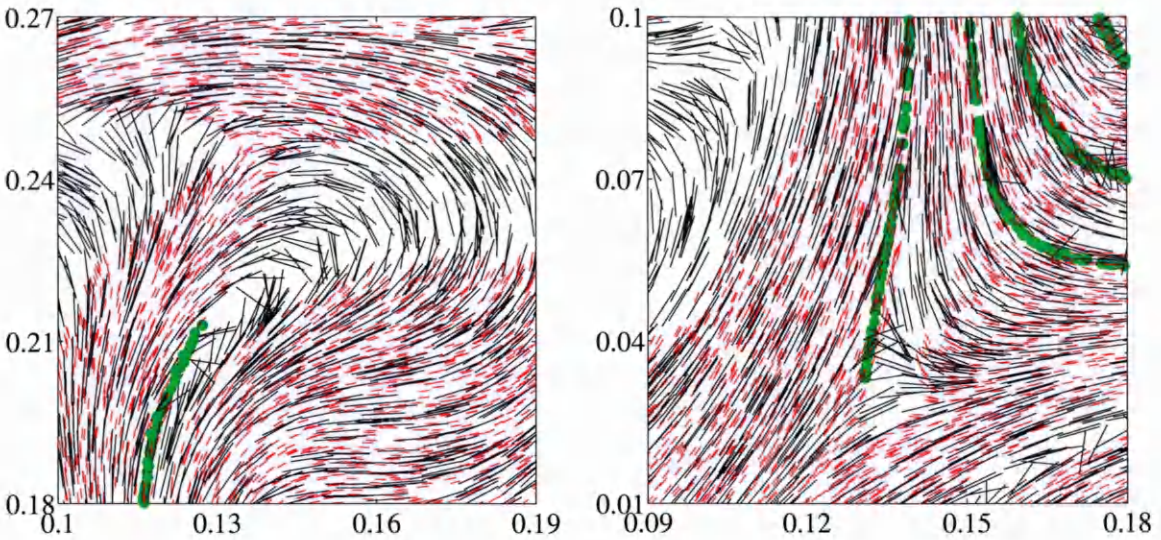

Figure 6.11: Simulation showing healed scar lines. The particles are shown in black, and the eigenvector field is shown in red. The points in green show positions of particles where $|\alpha_+| < 10^{-2}$ (and are therefore very close to scar lines). In these examples, because the scar line has become very narrow, the direction of the particles is not seen to flip around in the vicinity of the scar line, and a singularity emerges at the end of the scar line, namely a core (left) or a delta (right).

6.4 The long-time limit

6.4.1 Sensitivity to final position

The velocity field $\boldsymbol{u}(\boldsymbol{r}, t)$ is assumed to be statistically stationary, therefore we expect that at long time the patterns formed by the particles also become statistically stationary (so that at long times it becomes impossible to estimate the time from the statistics of a realization of the particle positions). This property is, however, not manifest in the solution (6.7). As $t - t_0 \to \infty$, the norm of the pseudomonodromy matrix grows. Also, while its elements are everywhere a smooth function of the initial position, the elements of $\mathbf{M}(\boldsymbol{r}, t, t_0)$ do become ever more sensitive to the position $\boldsymbol{r}$ as $t - t_0 \to \infty$. These observations suggest that as time increases the vector field $\mathbf{n}(\boldsymbol{r}, t)$ should vary increasingly rapidly as a function of $\boldsymbol{r}$, the final position of the particles. We argue below that this is not the case, and that $\mathbf{n}(\boldsymbol{r}, t)$ does reach a statistically stationary state.

If the eigenvector $\boldsymbol{u}_+(\boldsymbol{r}, t)$ corresponding to the largest eigenvalue is less sensitive to the final position $\boldsymbol{r}$ than the matrix $\mathbf{M}(\boldsymbol{r}, t, t_0)$ itself, then the apparent contradiction

discussed above can be resolved. We now argue that this is, in fact, the case.

Let us consider a 2×2 random matrix $\mathbf{M}(t, t_0)$ generated by Eq. (6.6) with the initial condition $\mathbf{M}(t_0, t_0) = \mathbf{I}$, where $\mathbf{I}$ is the unit matrix. The time-dependence of the matrix $\mathbf{M}$ has a positive Lyapunov exponent, Λ, describing exponential growth of the largest eigenvalue λ_+ as a function of $|t - t_0|$. Our discussion of the sensitivity of the solution will use an observation about the subdominant eigenvector $\boldsymbol{u}_-$, corresponding to the smallest eigenvalue λ_-. We start by showing that this eigenvector approaches a constant direction, which depends upon the initial realization of $\mathbf{B}$ in the first few multiples of the Lyapunov time, Λ^{-1}. The direction of the other eigenvector, $\boldsymbol{u}_+$ continues to fluctuate randomly.

To demonstrate this result, we consider the change in this eigenvector $\boldsymbol{u}_-(t)$ during a small time step δt. Let $\mathbf{X}(t)$ be a matrix formed using the eigenvectors of $\mathbf{M}(t)$, such that $\mathbf{D} = \mathbf{X}\mathbf{M}\mathbf{X}^{-1} = \mathrm{diag}(\lambda+, \lambda_-)$ is the diagonal matrix formed from the eigenvalues of $\mathbf{M}(t)$. In the transformed basis, the matrix at time $t + \delta t$ is

$$\mathbf{M}' = \mathbf{X}\,\mathbf{M}(t+\delta t)\,\mathbf{X}^{-1} = \mathbf{X}\,[\mathbf{I} + \mathbf{B}\delta t]\,\mathbf{M}\,\mathbf{X}^{-1} = [\mathbf{I} + \mathbf{B}'(t)\delta t]\,\mathbf{D} \tag{6.13}$$

where $\mathbf{B}' = \mathbf{X}\mathbf{B}\mathbf{X}^{-1}$. We write the eigenvalue equation for the subdominant eigenvalue of the matrix $\mathbf{M}'$, with subdominant eigenvector $\boldsymbol{u}'_-$:

$$\begin{aligned}
\mathbf{M}'\boldsymbol{u}'_- &= \begin{pmatrix} 1 + B'_{11}\delta t & B'_{12}\delta t \\ B'_{21}\delta t & 1 + B'_{22}\delta t \end{pmatrix} \begin{pmatrix} \lambda_+ & 0 \\ 0 & \lambda_- \end{pmatrix} \begin{pmatrix} \delta u'_- \\ 1 \end{pmatrix} \\
&= \begin{pmatrix} \lambda_+(1 + B'_{11}\delta t) & \lambda_- B'_{12}\delta t \\ \lambda_+ B'_{21}\delta t & \lambda_-(1 + B'_{22}\delta t) \end{pmatrix} \begin{pmatrix} \delta u'_- \\ 1 \end{pmatrix} \\
&= (\lambda_- + \delta\lambda_-) \begin{pmatrix} \delta u'_- \\ 1 \end{pmatrix} .
\end{aligned} \tag{6.14}$$

Neglecting terms of higher order in δt, the first element of this eigenvalue equation gives

$$\delta u'_- = -\frac{\lambda_-}{\lambda_+ - \lambda_-} B'_{12}\delta t \; . \tag{6.15}$$

In the limit as $t \to \infty$ the eigenvalues satisfy $|\lambda_+/\lambda_-| \to \infty$, and therefore $\delta u'_-/\delta t \to 0$. We conclude that the eigenvector of the subdominant eigenvalue approaches a constant direction. Writing the eigenvector of the dominant eigenvalue of $\mathbf{M}'$ as $\boldsymbol{u}'_+ = (1, \delta u'_+)$, the corresponding expression is

$$\delta u'_+ = B'_{21}\delta t \ . \tag{6.16}$$

Here the coefficient of δt continues to fluctuate as $t \to \infty$, and we conclude that the dominant eigenvector continues to rotate.

Now, given the orientations of the particles at time t, let us consider their orientations at the earlier time t_0. This map is determined by a time-reversed version of Eq. (6.6). Its solution is constructed by analogy with Eq. (6.7), replacing $\mathbf{M}$ with $\mathbf{M}^{-1}$. The eigenvector of $\mathbf{M}(t, t_0)$ corresponding to its largest eigenvalue is also the eigenvector of $\mathbf{M}^{-1}(t, t_0)$ corresponding to its smallest eigenvalue. Using the result discussed above, the eigenvector corresponding to the smallest eigenvalue of $\mathbf{M}^{-1}(t, t_0)$ becomes insensitive to t_0 when $\Lambda|t - t_0| \gg 1$. The eigenvector of $\mathbf{M}(t, t_0)$ corresponding to the largest eigenvalue becomes therefore insensitive to t_0. We conclude that although the matrix $\mathbf{M}(t, t_0)$ has an increasingly sensitive dependence upon position as $t - t_0 \to \infty$, the eigenvector $\boldsymbol{u}_+$ does not become increasingly sensitive. Because the particle directions are asymptotic to these vectors, the particle directions do not become increasingly sensitive to the position $\boldsymbol{r}$ as time increases, except in the vicinity of gyres.

We conclude that as $t - t_0 \to \infty$, the vector field $\mathbf{n}(\boldsymbol{r}, t)$ is statistically stationary, approaching the vector field $\boldsymbol{u}_+(\boldsymbol{r}, t)$ almost everywhere.

6.4.2 Distribution of angle gradients

We have seen that the particle directions do not become increasingly sensitive to the position as time increases. It is desirable to quantify the sensitivity to the position. We have seen that the textures formed by the particle orientations show regions where the particle direction varies very rapidly with the position, relative to other regions.

Earlier, we described how the existence of scar lines explains the structures seen in specific realizations of the patterns. In this section we consider the probability distribution of the angle gradient, showing that the distribution is very broad, being well approximated by a log-normal distribution. This very broad distribution of the angle gradient is consistent with the existence of the structures described in section 6.3.

We now consider how to calculate the angle gradient $\boldsymbol{g} = \boldsymbol{\nabla}\theta$. In the following, we obtain an expression for one component, g_1, of $\boldsymbol{g}$. We obtain an expression for g_1 which is argued to be log-normally distributed.

Let us consider the difference between the eigenvector directions between two pseudomonodromy matrices evaluated along neighbouring trajectories. The reference trajectory has pseudomonodromy matrix $\mathbf{M}(t)$ and the neighbouring trajectory has pseudomonodromy matrix $\mathbf{M}(t) + \delta\mathbf{M}(t)$. We have seen that the subdominant eigenvector $\boldsymbol{u}_-$ of each pseudomonodromy matrix approaches a constant direction as $t \to \infty$, so the angle between them, $\delta\theta(t)$, must approach a constant value, that is $\delta\theta(t) \to \delta\theta_\infty$ as $t \to \infty$. Let $\delta\mathbf{M}(t)$ be the change in the pseudomonodromy matrix due to shifting the end point of the trajectory at time t from $\boldsymbol{r} = (r_1, r_2)$ to $\boldsymbol{r} + \delta\boldsymbol{r} = (r_1, r_2) + (\delta r_1, 0)$. The first component of $\boldsymbol{g}$ is $g_1 = \lim_{\delta r_1 \to 0} \delta\theta/\delta r_1$.

We introduce an orthonormal basis $\boldsymbol{u}_1$, $\boldsymbol{u}_2$ satisfying $\boldsymbol{u}_i \cdot \boldsymbol{u}_j = \delta_{ij}$, where $\boldsymbol{u}_2 = \boldsymbol{u}_-(t)$ is the subdominant eigenvector of $\mathbf{M}(t)$. The elements of $\mathbf{M}$ in this basis are $M'_{ij} = \boldsymbol{u}_i \cdot \mathbf{M}(t)\boldsymbol{u}_j$, which form the matrix

$$\mathbf{M}' = \begin{pmatrix} M'_{11} & 0 \\ M'_{21} & \lambda_- \end{pmatrix} . \tag{6.17}$$

When the end-point of the particle trajectory is shifted by a distance $\delta\boldsymbol{r} = (\delta r_1, 0)$, the matrix $\mathbf{M}'$ is perturbed to $\mathbf{M}' + \delta\mathbf{M}'$, and the angle of the subdominant eigenvector $\boldsymbol{u}_-$ changes by a small amount $\delta\theta$, which can be obtained by solving the eigenvalue

equation

$$\begin{pmatrix} M'_{11}+\delta M'_{11} & \delta M'_{12} \\ M'_{21}+\delta M'_{21} & \lambda_- + \delta M'_{22} \end{pmatrix} \begin{pmatrix} \delta\theta \\ 1 \end{pmatrix} = (\lambda_- + \delta\lambda_-) \begin{pmatrix} \delta\theta \\ 1 \end{pmatrix} . \tag{6.18}$$

Using the first line of this equation to solve for $\delta\theta$, retaining leading order terms we obtain

$$\delta\theta = -\frac{\delta M'_{12}}{M'_{11} - \lambda_-} . \tag{6.19}$$

We note that when t is large, so that $\lambda_+/\lambda_- \gg 1$, we may drop the term λ_- from the denominator, and approximate the first element of the gradient vector by

$$g_1 = \lim_{\delta r_1 \to 0} \frac{\delta\theta}{\delta r_1} \sim -\frac{\boldsymbol{u}_1 \cdot \frac{\partial \mathbf{M}(t)}{\partial r_1} \boldsymbol{u}_2}{\boldsymbol{u}_1 \cdot \mathbf{M}(t) \boldsymbol{u}_1} . \tag{6.20}$$

It is not immediately clear that this expression approaches a constant value, but below we show that this is, in fact, the case.

It is desirable to have an explicit expression for the coefficients $\delta M'_{ij}(t)$. Note that the pseudomonodromy matrix $\mathbf{M}(t)$ satisfying $d\mathbf{M}/dt = \mathbf{B}(t)\mathbf{M}$ can be approximated by a product:

$$\mathbf{M}(t) = \lim_{\delta t \to 0} \prod_{j=1}^{\mathrm{Int}(t/\delta t)} [\mathbf{I} + \mathbf{B}(j\delta t)\delta t] , \tag{6.21}$$

where $\mathrm{Int}(x)$ is an integer part of x. Writing $\mathbf{C} = \partial\mathbf{B}/\partial r_1$, the monodromy matrix for the displaced trajectory is

$$\begin{aligned} \mathbf{M}(t) + \delta\mathbf{M}(t) &= \lim_{\delta t \to 0} \prod_{j=1}^{\mathrm{Int}(t/\delta t)} [\mathbf{I} + \mathbf{B}(j\delta t)\delta t + \mathbf{C}(j\delta t)\delta r_1 \delta t] \\ &= \mathbf{M}(t) + \delta r_1 \lim_{\delta t \to 0} \sum_{k=1}^{\mathrm{Int}(t/\delta t)} \prod_{j=1}^{\mathrm{Int}[(t-t')/\delta t]} [\mathbf{I} + \mathbf{B}(t' + j\delta t)\delta t] \\ &\quad \times \mathbf{C}(k\delta t)\, \delta t \prod_{j=1}^{\mathrm{Int}(t'/\delta t)} [\mathbf{I} + \mathbf{B}(j\delta t)] + O(\mathbf{C}^2) . \end{aligned} \tag{6.22}$$

Approximating sum as an integral we find

$$\frac{\partial \mathbf{M}(t)}{\partial r_1} = \int_0^t dt' \, \mathbf{M}(t,t') \, \mathbf{C}(t') \, \mathbf{M}(t',0) \; . \tag{6.23}$$

We now consider why g_1, given by Eq. (6.20), is independent of t in the limit as $t \to \infty$. We introduce the initial time in the arguments of the pseudomonodromy matrix, writing the pseudomonodromy matrix giving displacements at time t in terms of those at time t_0 as $\mathbf{M}(t,t_0)$. Consider the vectors $\boldsymbol{v}_1 = \mathbf{M}(t,0)\boldsymbol{u}_1$ and $\boldsymbol{v}_2 = \delta\mathbf{M}(t,0)\boldsymbol{u}_2$, where $\boldsymbol{u}_1$, $\boldsymbol{u}_2$ are two arbitrary vectors. We will show that the vectors $\boldsymbol{v}_1$ $\boldsymbol{v}_2$ almost always become co-linear as $t \to \infty$. First, we choose a time t_1 such that $(t-t_1)\Lambda \gg 1$. Note that we can write $\mathbf{M}(t,t_0) = \mathbf{M}(t,t_1)\mathbf{M}(t_1,t_0)$. The direction of the vector $\boldsymbol{v}_1 = \mathbf{M}(t,t_0)\boldsymbol{u}_1$ is almost always nearly co-linear with the direction of the dominant eigenvector of $\mathbf{M}(t,t_1)$, independent of the vector $\boldsymbol{u}_1$. In the case of the vector $\boldsymbol{v}_2 = \delta\mathbf{M}(t,t_0)\boldsymbol{u}_2$, we can write

$$\begin{aligned} \delta\mathbf{M}(t,t_0) &= \delta r_1 \, \mathbf{M}(t,t_1) \int_{t_0}^{t_1} dt' \, \mathbf{M}(t_1,t') \, \mathbf{C}(t') \, \mathbf{M}(t',t_0) \\ &\quad + \delta r_1 \int_{t_1}^{t} dt' \, \mathbf{M}(t,t') \, \mathbf{C}(t') \, \mathbf{M}(t',t_0) \\ &= \mathbf{M}(t,t_1) \, \delta\mathbf{M}(t_1,t_0) \, [1 + O((t-t_1)/t)] \end{aligned} \tag{6.24}$$

so that to leading order $\boldsymbol{v}_2$ is also co-linear with the dominant eigenvector of $\mathbf{M}(t,t_1)$. We conclude that the vectors $\boldsymbol{v}_1$ and $\boldsymbol{v}_2$ are almost always co-linear, provided $\Lambda(t - t_0) \gg 1$.

Let us consider the evaluation of Eq. (6.20) in the case where

$$\mathbf{M} = \mathbf{M}(t,t_0) = \mathbf{M}(t,t')\mathbf{M}(t',t_0) = \mathbf{M}_2\mathbf{M}_1 \tag{6.25}$$

where $\mathbf{M}_1 = \mathbf{M}(t',t_0)$, $\mathbf{M}_2 = \mathbf{M}(t,t')$. Correspondingly, neglecting terms of order δr_1^2, we have

$$\delta\mathbf{M} = \mathbf{M}_2\delta\mathbf{M}_1 + \delta\mathbf{M}_2\mathbf{M}_1 \; . \tag{6.26}$$

We consider the case where $\Lambda(t - t_0) \gg 1$, with $t > t' > t_0$. In order to establish

that the angle $\delta\theta$ becomes asymptotically independent of time, we must show that $\delta\theta = \delta\theta_1$, where $\delta\theta$ is given by Eq. (6.20) and where $\delta\theta_1$ is the expression obtained by replacing $\delta\mathbf{M}$, $\mathbf{M}$ with $\delta\mathbf{M}_1$, $\mathbf{M}_1$. Thus, in view of Eqs. (6.25) and (6.26), we must show that

$$\delta\theta = -\frac{\boldsymbol{u}_1 \cdot \delta\mathbf{M}_1\boldsymbol{u}_2}{\boldsymbol{u}_1 \cdot \mathbf{M}_1\boldsymbol{u}_1}, \tag{6.27}$$

where $\delta\theta$ can be written using Eqs. (6.20) and (6.26):

$$\delta\theta = -\frac{\boldsymbol{u}_1 \cdot \mathbf{M}_2\delta\mathbf{M}_1\boldsymbol{u}_2}{\boldsymbol{u}_1 \cdot \mathbf{M}_2\mathbf{M}_1\boldsymbol{u}_1} - \frac{\boldsymbol{u}_1 \cdot \delta\mathbf{M}_2\mathbf{M}_1\boldsymbol{u}_2}{\boldsymbol{u}_1 \cdot \mathbf{M}_2\mathbf{M}_1\boldsymbol{u}_1}. \tag{6.28}$$

The second term on the right-hand side of the equality is negligible, because $\mathbf{M}_1\boldsymbol{u}_2 = \lambda_-\boldsymbol{u}_-$, and $\lambda_- \to 0$ as $t \to \infty$. In the first term the additional factor of $\mathbf{M}_2$ makes no difference to the value of $\delta\theta$ only if the vectors $\delta\mathbf{M}_1\boldsymbol{u}_2$ and $\mathbf{M}_1\boldsymbol{u}_1$ are co-linear. But we have argued above that these vectors are asymptotically co-linear in the limit as $\Lambda(t - t_0) \to \infty$. Thus we conclude that the angle $\delta\theta$ between two sub-dominant eigenvectors $\boldsymbol{u}_-$ in forward-time propagation does become independent of time as $t \to \infty$, justifying Eq. (6.20). We can now use the arguments of section 6.4.1 to draw conclusions about the dependence of the reverse-time propagation of the dominant eigenvectors $\boldsymbol{u}_+$, which determine the particle direction. In particular, we conclude that the angle gradient at time t does become independent of the initial time t_0 as $t - t_0 \to \infty$.

We have seen that the angle gradient of the orientation field of the particles remains finite in the long-time limit. It is of interest to consider the probability distribution of the angle gradient. We argue that this quantity has an approximately log-normal distribution. Since the pseudomonodromy matrix may be expressed as a product of a large number of independent random factors, the matrix elements of both $\delta\mathbf{M}$ and $\mathbf{M}$ are log-normally distributed. The distribution of their ratio is also log-normal. We conclude that the distribution of the angle gradient, given by Eq. (6.20), is therefore also log-normal at large times, provided the correlation time of the flow τ is short compared to the Lyapunov time Λ^{-1}. In Fig. 6.12 this result is illustrated by a histogram of the distribution of the logarithm of the angle gradient for the same

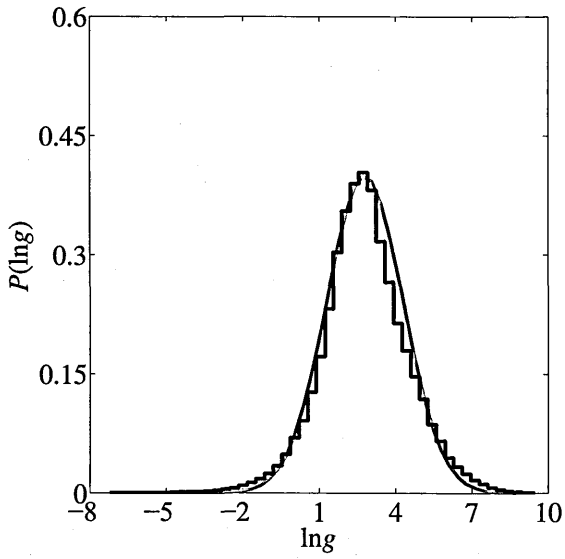

Figure 6.12: Histogram of the probability density of the angle gradient, showing that this has an approximately log-normal distribution. The parameter values of the simulation are the same as for the other figures.

parameter values as used in the other numerical simulations. A Gaussian fit matches the histogram very closely.

6.4.3 Textures in the long time limit

In the long-time limit, the application of the concepts discussed in section 6.3 requires careful consideration. This is because, at very large times, the pseudomonodromy matrix $\mathbf{M}(\boldsymbol{r}, t)$ becomes increasingly sensitive to the final position of the particles, $\boldsymbol{r}$. As $t - t_0$ increases the gyres may shrink in area, their boundaries may stretch, and they may merge together. Also, gyres with a zero Poincaré index may disappear. We expect that at very large times the gyres are extended into lines where $\mathrm{tr}(\mathbf{M})$ changes sign. These lines are expected to become ever more closely spaced as $t - t_0 \to \infty$, with typical spacing $\eta \exp(-\lambda|t - t_0|)$. Following the reasoning presented in section 6.3, at large $t - t_0$ we expect that $\boldsymbol{u}_+$ fluctuates on a length scale η, independent of $t - t_0$. The definition of the type I scar lines depends on the initial direction field, and these structures are therefore expected to become irrelevant at very large times.

In order to discuss the long-time limit, we consider an expression for the direction field $\mathbf{n}(\boldsymbol{r}, t)$ in terms of the dominant eigenvector field. Let $\mathbf{M}(\boldsymbol{r}, t, t_0)$ be the pseudomonodromy matrix for a trajectory reaching $\boldsymbol{r}$ at time t, starting at time t_0, and

let $\boldsymbol{u}_+(\boldsymbol{r},t,t_0)$ be the corresponding dominant eigenvector. As $t-t_0 \to \infty$ we expect that $\mathbf{n}(\boldsymbol{r},t) \sim \boldsymbol{u}_+(\boldsymbol{r},t)$ for almost all points in the plane. We can therefore construct the vector field $\mathbf{n}(\boldsymbol{r},t)$ from the dominant eigenvector $\boldsymbol{u}_+(\boldsymbol{r},t,t_0)$ as follows

$$\mathbf{n}(\boldsymbol{r},t) = \lim_{t_0 \to -\infty} \boldsymbol{u}_+(\boldsymbol{r},t,t_0) \ . \tag{6.29}$$

Let us consider the way in which this limit is approached, keeping t fixed and letting $t_0 \to -\infty$, starting from a time $t_0 = t - \delta t$ which is very close to t. We know that there exist gyres which shrink, stretch and fold as $t_0 \to -\infty$, and that the Poincaré index of $\boldsymbol{u}_+$ about the boundary of these gyres may be non-zero. There are two possibilities for the manner in which the limit $t - t_0 \to \infty$ is approached. The first possibility is that gyres with opposite topological charges combine, so that in the limit the field $\boldsymbol{u}_+(\boldsymbol{r},t,t_0)$ becomes topologically trivial. Numerical experiments indicate that this case is not realized in practice. The other possibility is that as the gyres shrink the field $\mathbf{n}(\boldsymbol{r},t)$ can develop singularities which shrink in size and which cause no abrupt changes of their direction except in the vicinity of the gyres. We have seen that there exist type II scar lines where the direction of $\mathbf{n}(\boldsymbol{r},t)$ changes by π on crossing a narrow gyre.

As $t_0 \to -\infty$, the gyres become narrower and the scar lines heal over, that is there is unlikely to be any particle close to the gyre, so that the gyres therefore have no visible effect on the field $\mathbf{n}(\boldsymbol{r},t)$. Consider a loop which encircles the end of a type II scar line. Initially the Poincaré index of $\mathbf{n}(\boldsymbol{r},t)$ about this loop is zero. When the angle change of $\pm\pi$ associated with crossing the scar line disappears as the scar line heals over, the Poincaré index of the circuit becomes $N = \pm\frac{1}{2}$. The disappearance of the scar line is therefore associated with the emergence of a point singularity at the positions where the ends of this line were located.

We have shown in section 6.4 that the patterns formed by the eigenvector field $\boldsymbol{u}_+(\boldsymbol{r},t,t_0)$ are statistically stationary in the long-time limit, because the direction of the dominant eigenvector is determined only by the recent history of the pseudomonodromy matrix, over a few multiples of its Lyapunov time, Λ^{-1}. This is true despite

the fact that the elements of $\mathbf{M}(\boldsymbol{r}, t, t_0)$ have unbounded growth and become increasingly sensitive to $\boldsymbol{r}$ as $t - t_0 \to \infty$. We have also presented an argument showing how the direction field $\mathbf{n}(\boldsymbol{r}, t)$ and its apparent singularities are obtained from the dominant eigenvector field using Eq. (6.29). We conclude that the textures of the direction field are also statistically stationary in the long-time limit.

6.5 Three-dimensional flows

Thus far, we have considered textures in two-dimensional flows. In this section we consider what additional structures might arise when the flow is three-dimensional. The principal difference is that in a three dimensional flow the direction vector $\mathbf{n}(\boldsymbol{r}, t)$ covers a sphere rather than a circle (it remains non-oriented), but the equation of motion (6.2) and its solution (6.7) have the same form. In three dimensions, there are many new questions which can be addressed, and some of the implications of the solution (6.7) for three-dimensional flows have been considered in [29, 30]. Here we confine ourselves to a discussion of those aspects which are relevant to the experiment on a rheoscopic fluid discussed in the next chapter In the three-dimensional case, the interpretation of experimental results is most straightforward if the rheoscopic agent is sufficiently concentrated that the reflected light comes from the surface layer of the liquid.

For the problem which we consider, the colour of the scattered light is determined solely by the direction of the projection of $\mathbf{n}(\boldsymbol{r}, t)$ in the plane of the fluid surface, evaluated at a point on the fluid surface. This projected vector field, $\mathbf{n}_{\mathrm{p}}(\boldsymbol{r}, t)$, can have singularities, if there are positions where the particles point out of the surface of the liquid. The projected vector field $\mathbf{n}_{\mathrm{p}}(\boldsymbol{r}, t)$ then has a simple zero, which has Poincaré index $+1$, as well as the fingerprint-like singularities.

Our explanation for the occurrence of apparent singularities with Poincaré index $\pm\frac{1}{2}$ depends upon the existence of gyres, where there is no dominant eigenvalue, and where the eigenvector has a non-zero Poincaré index on traversing the boundary. In the three-dimensional case, we must consider how these concepts are modified.

In section 6.2 we have argued that in a three dimensional volume preserving flow the pseudomonodromy matrix $\mathbf{M}$ has three possible spectral types. Type 1 and 2 correspond to the alignment of particles with corresponding dominant eigenvectors and type 3 corresponds to three-dimensional gyres which occupy a finite volume in the three-dimensional space. The arguments used in section 6.3 can be extended to the three-dimensional case by considering the projected vector $\mathbf{n}_{\mathrm{p}}(\boldsymbol{r}, t)$ in the plane of the fluid surface. This vector is asymptotic to the projection of the dominant eigenvector in the plane of the fluid surface, $\boldsymbol{u}_{+\mathrm{p}}(\boldsymbol{r}, t)$. The arguments of section 6.3 remain valid provided the Poincaré index of $\boldsymbol{u}_{+\mathrm{p}}(\boldsymbol{r}, t)$ around the curve where the gyre intersects the fluid surface is non-zero, for some of the gyres. Numerical experiments have shown that this condition is satisfied, so that on the surface of a three-dimensional flow the field $\mathbf{n}_{\mathrm{p}}(\boldsymbol{r}, t)$ does contain fingerprint-like textures, as well as simple singularities which have an integer Poincaré index.

We remark that this observation has an interesting consequence for the three-dimensional structure of the gyres. If the plane is moved down through the fluid, the curve representing the intersection of the gyre with this plane will deform. If this curve shrinks to a point, by continuity the Poincaré index associated with $\boldsymbol{u}_{+\mathrm{p}}(\boldsymbol{r}, t)$ must be zero. A curve can be shrunk to a point on a surface with the topology of a sphere, but a surface with non-zero genus g can contain curves which cannot be shrunk to a point. It follows that the three-dimensional gyres include examples which are multiply-connected (for example, a torus has $g = 1$).

We conclude that if the flow is three-dimensional, the fingerprint-like textures still appear on the surface, but that there are also points where the projected orientation vector field $\mathbf{n}_{\mathrm{p}}(\boldsymbol{r}, t)$ has simple zeros, with Poincaré index $+1$, due to particles aligning perpendicular to the surface. Fig. 6.13 shows examples of the orientations of rod-like particles in a thin layer within a three-dimensional incompressible random flow, projected onto the plane of the paper. This figure shows the occurrence of singularities with Poincaré index $+1$ where the particles point out of the plane, as well as the fingerprint-like textures.

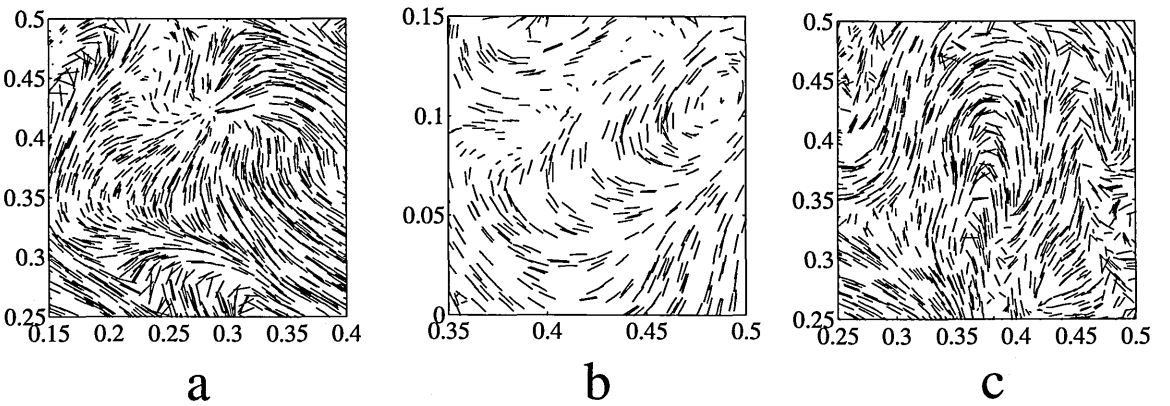

Figure 6.13: Projected orientations of particles suspended in a three-dimensional flow. Only particles in a thin layer (with depth much smaller than the correlation length of the velocity field) are shown. These textures may have singularities due to the particles becoming perpendicular to the plane (**a**, **b**), as well as fingerprint-like singularities (**c**).

6.6 Summary

In this chapter we have discussed patterns formed by small axisymmetric particles advected in a complex flow. The direction field of the particles is a non-oriented vector field and may contain topological singularities with a half-integer Poincaré index. Our numerical simulations show that the direction field does contain such singularities, which are of the same type as those seen in fingerprints. Based on the solution of the equation of motion we have found that the singularities cannot exist in a strict mathematical sense, but we have argued that they are approached in an asymptotic sense. First, scar lines emerge where the particles abruptly change direction by π. At later times, the scar lines become so narrow that they effectively disappear, but their ends remain as point singularities with a half-integer Poincaré index. We have shown that the direction field of the particles reaches statistically stationary state in the long-time limit, and that the distribution of the angle gradient is approximately log-normal, which is consistent with the existence of singularities, where the particles changes directions abruptly.

Chapter 7

Theoretical and experimental studies of rheoscopic visualizations

Most parts of this chapter are based on two papers: "Poincaré indices of rheoscopic visualisations" (arxiv : 0903.3615) and "Emergent order in rheoscopic swirls" (in preparation), both by Wilkinson, Mehlig and Bezuglyy. The author of the thesis performed most of the numerical simulations and contributed to the discussion of the theory. The experiment was set up and performed by the author of the thesis. The idea of the experiment was originally suggested by Michael Wilkinson.

7.1 Introduction

In the previous chapter we have developed the theory explaining an existence of apparent singularities with a half-integer Poincaré index in the textures of axisymmetric particles in a random flow in a plane. The solution of the equation of motion (6.7) indicates that in a random flow with a positive largest Lyapunov exponent the textures in the long-time limit are independent of the initial orientation field and approach the field of dominant eigenvectors of the pseudomonodromy matrix. The textures at short time, on the other hand, do have a memory of the initial orientations. The apparent singularities occur at the end-point of scar lines which are specific to the choice of the initial conditions. In the previous chapter we considered the case when

the initial orientation field of the particles is non-random and uniform, so that the scar lines appear as continuous lines. It is desirable to understand the textures for other choices of the initial conditions, as well as the degree to which our theory can be related to the motion of a rheoscopic fluid, a suspension of small elongated light-reflecting crystals (these are typically coated mica flake or crystalline guanine [70]). When a rheoscopic fluid is left to stand for a while, the particles become randomly oriented due to the effects of Brownian motion. We, therefore, can assume that the initial orientation field is random and isotropic in this case. When the fluid is set in motion, the crystals start to align, and at later times we can describe the distribution of angles by a probability density function. The alignment of the particles may be quantified by an order parameter. In section 7.2 we describe a natural choice of the order parameter for the particle orientations. The order parameter is a vector with the length varying from 0 to 1, where 0 corresponds to an isotropic configuration and 1 corresponds to a perfect alignment of the particles with the direction of the corresponding dominant eigenvector of the pseudomonodromy matrix. The direction of the order parameter is defined by the predominant orientation of the particles at a given point. We obtain the formula for the order parameter using the solution of the equation of motion described in the previous chapter. The order parameter field is a non-oriented vector field which can exhibit singularities with a half-integer Poincaré index. The numerical simulations indicate that singularities do exist in the order parameter field. Unlike the case in the previous chapter, these are true singularities, and they are located at the points in a plane where the length of the order parameter is 0. In section 7.3 we describe the normal form of these structures.

The order parameter can be related to the reflection of light by a rheoscopic fluid. It is expected that when the particles are oriented isotropically, the light is diffused by many randomly oriented particles, whereas when the particles are aligned, the light is reflected in a way which depends on their orientation and the degree of the alignment. In the previous chapter we have presented the method to illustrate the topology of the textures by means of a colour-coding using three light sources [see Fig. 6.4 and Eq. (6.1)]. Using similar arguments, in section 7.4, we present a model which relates

the order parameter to the reflection of light by a rheoscopic fluid. In section 7.5 we report on the results of the experiment involving a randomly stirred rheoscopic fluid illuminated by three coloured lights. The patterns we observe in the experiment support our theory of an existence of singularities with a half-integer Poincaré index in the textures of anisotropic particles. We remark that the idea of using coloured light sources was previously suggested in [36], but the technique was not used to reveal the topology of the textures.

7.2 Order parameter

7.2.1 General definition of the order parameter

In the case we consider below, the particles are aligned in a plane so that their direction is defined by a single angle θ. We describe the angle distribution of the particles at a given point in space and time by the probability density $P(\theta)$, which is initially uniform. Because the direction field is non-oriented, the probability density $P(\theta)$ satisfies $P(\theta + \pi) = P(\theta)$. This probability density depends upon both position and time, but we suppress the arguments $\boldsymbol{r}$ and t in the discussion below.

A suitable order parameter for the axisymmetric particles can be obtained from $P(\theta)$ by first calculating the 'inertia tensor' of the orientation of the particles, which has components

$$I_{ij} = \int_0^{2\pi} d\theta \; P(\theta)[\mathbf{n}_i \cdot \mathbf{n}(\theta)][\mathbf{n}_j \cdot \mathbf{n}(\theta)] \tag{7.1}$$

where $\mathbf{n}(\theta)$ is a unit vector in the direction θ, and $\mathbf{n}_i$ is a unit vector in the direction of i-th axis of the Cartesian coordinate system [in the two-dimensional case these are $\mathbf{n}_1 = (1, 0)$ and $\mathbf{n}_2 = (0, 1)$]. The three distinct components of I_{11}, I_{12}, I_{22} are not independent, because $\mathbf{n}(\theta)$ is constrained to have unit length. They can be mapped to the order parameter vector $\boldsymbol{\zeta}$ as follows. The inertia tensor has real, positive eigenvalues $\mathcal{I}_1, \mathcal{I}_2$, with $\mathcal{I}_1 \geq \mathcal{I}_2$ and corresponding orthonormal eigenvectors $\boldsymbol{U}_1, \boldsymbol{U}_2$. The eigenvalues satisfy $\mathcal{I}_1 + \mathcal{I}_2 = 1$, and the case $\mathcal{I}_1 = 1$ corresponds to a perfect alignment, whereas $\mathcal{I}_1 = \mathcal{I}_2 = \frac{1}{2}$ corresponds to an isotropic distribution. We define $\boldsymbol{\zeta}$

to be a non-oriented vector in the direction $\boldsymbol{U}_1$ with magnitude which is a function of $\mathcal{I}_1 - \mathcal{I}_2$. We first consider a special case where the particles align with the direction θ_0 with probability p_0, or else are randomly distributed with probability $1 - p_0$, that is the probability density is given by

$$P(\theta) = \frac{p_0}{2}[\delta(\theta - \theta_0) + \delta(\theta - \theta_0 - \pi)] + \frac{1 - p_0}{2\pi} . \tag{7.2}$$

It is natural to define the order parameter so that $\boldsymbol{\zeta} = p_0 \mathbf{n}(\theta_0)$ in this case. For this distribution, in the case $\theta_0 = 0$ we find $\mathcal{I}_1 = (1 + p_0)/2$ and $\mathcal{I}_2 = (1 - p_0)/2$, so that $\mathcal{I}_1 - \mathcal{I}_2 = p_0$. We, therefore, define the order parameter as

$$\boldsymbol{\zeta} = (\mathcal{I}_1 - \mathcal{I}_2)\boldsymbol{U}_1 . \tag{7.3}$$

This is a general definition for the order parameter of non-spherical particles in two dimensions. An analogous definition can be used in three dimensions, where a general inertia tensor has six independent components, but the inertia tensor for the particle directions has five parameters because of the constraint that $|\mathbf{n}| = 1$.

7.2.2 Order parameter in terms of the pseudomonodromy matrix

We calculate the order parameter for the case where the particles are initially randomly oriented, so that the initial direction $\mathbf{n}_0$ at a given point in a plane is uniformly distributed about the unit circle. According to the solution presented in the previous chapter [Eq. (6.7)], a vector $\mathbf{n}_0$ on the circle is mapped to a vector $\boldsymbol{d}(t) = \mathbf{M}\mathbf{n}_0$ which lies on an ellipse (we recall that $\mathbf{M}$ is the pseudomonodromy matrix satisfying $\det(\mathbf{M}) = 1$). This ellipse is described by its aspect ratio, $\nu_e \geq 1$, and by the direction of its long axis, θ_0. In the following we obtain the probability density $P(\theta)$ and use this to obtain the order parameter $\boldsymbol{\zeta}$ in terms of ν_e and θ_0.

An angle interval $d\phi$ on the unit circle is mapped to a segment of the ellipse which is at an angle θ to its longer axis and which spans an angle interval $d\theta$. The angle θ is

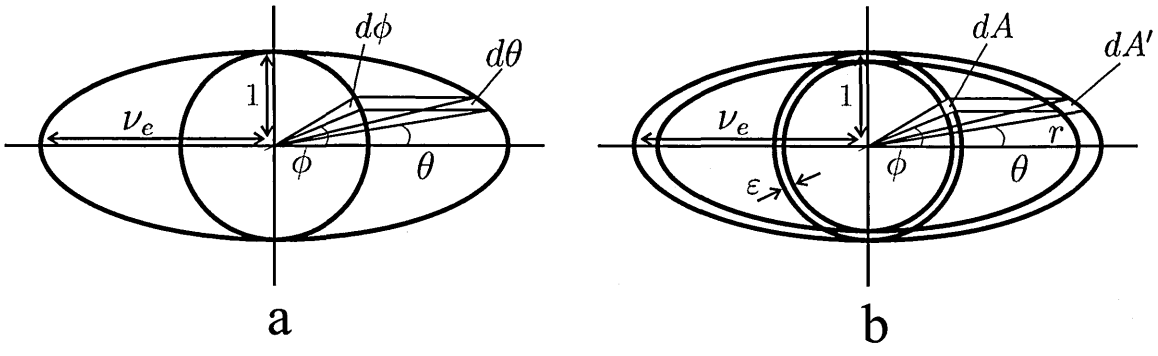

Figure 7.1: Illustrating the geometrical construction used to determine the probability density of the angle, $P(\theta)$.

independent of the overall scale of the ellipse, and it is convenient to consider the case where the short axis intersects the unit circle (see Fig. 7.1**a**). The probability element for the direction of $\mathbf{n}_0$ being in the interval $d\phi$ is $dP = d\phi/2\pi$, because the initial probability density is uniform. This is the same as the probability element for $\boldsymbol{d}(t)$ being in the interval $d\theta$ on the ellipse, so that the probability density $P(\theta)$ satisfies

$$dP = P(\theta)d\theta = \frac{1}{2\pi}d\phi. \tag{7.4}$$

An elementary geometrical construction can be used to surmise the relation between $d\phi$ and $d\theta$. Instead of considering the mapping of a circle to an ellipse, let us consider the image of a narrow annulus of angular width $d\phi$ between a circle with unit radius and one with radius $1-\varepsilon$ (with $\varepsilon \ll 1$), so that the area of this element is $dA \sim \varepsilon d\phi$. The element of the annulus is the set difference between two segments of discs spanned by an angle $d\phi$, one of unit radius, the other of radius $1-\varepsilon$. These segments are transformed into regions which may also be approximated by segments of circles: the larger one is approximated by a segment of a circle of radius r spanned by an angle $d\theta$, having area $\sim \frac{1}{2}r^2 d\theta$, and the smaller one by a segment which is smaller in area by a factor $(1-\varepsilon)^2 \sim 1-2\varepsilon$ (see Fig. 7.1**b**). The area of the transformed image of the annulus is therefore $dA' = \varepsilon r^2 d\theta$. Because the transformation from a circular region to an ellipse stretches the x-axis by the factor ν_e, we also have $dA' = \nu_e \varepsilon d\phi$. We conclude that $d\phi = r^2 d\theta/\nu_e$, where r is the distance from the origin to a point on the ellipse at angle θ from the long axis. The equation of the ellipse is

$\nu_e^2 = x^2 + \nu_e^2 y^2$, where $x = r\cos\theta$, $y = r\sin\theta$, so that $\nu_e^2 = r^2[(\nu_e^2 - 1)\sin^2\theta + 1]$. Using Eq. (7.4) we conclude that the probability density for the direction of the vector $\boldsymbol{d}$ is

$$P(\theta) = \frac{r^2}{2\pi\nu_e} = \frac{\nu_e}{2\pi}\frac{1}{(\nu_e^2 - 1)\sin^2(\theta - \theta_0) + 1}, \tag{7.5}$$

where θ_0 is the direction of the long axis. Using the identities

$$\begin{aligned} \int_0^{2\pi} dx \, \frac{\cos^2 x}{A\sin^2 x + 1} &= 2\pi\frac{\sqrt{A+1} - 1}{A} \\ \int_0^{2\pi} dx \, \frac{\sin^2 x}{A\sin^2 x + 1} &= 2\pi\frac{\sqrt{A+1} - 1}{A\sqrt{A+1}} \end{aligned} \tag{7.6}$$

we find that for this probability density the elements of the inertia tensor are

$$\begin{aligned} I_{11} = 1 - I_{22} &= \frac{\nu_e}{\nu_e + 1}\cos^2\theta_0 + \frac{1}{\nu_e + 1}\sin^2\theta_0 \\ I_{12} &= \frac{\nu_e - 1}{\nu_e + 1}\cos\theta_0\sin\theta_0 \, . \end{aligned} \tag{7.7}$$

The eigenvalues of the inertia tensor are then $\mathcal{I}_1 = \frac{\nu_e}{\nu_e+1}$ and $\mathcal{I}_2 = \frac{1}{\nu_e+1}$. The order parameter for an initially uniform angular distribution is therefore

$$\zeta = \frac{\nu_e - 1}{\nu_e + 1}\mathbf{n}(\theta_0). \tag{7.8}$$

It remains to express the aspect ratio $\nu_e \geq 1$ of the ellipse in terms of the matrix $\mathbf{M}$. The equation defining the unit circle $|\mathbf{n}_0| = 1$ can be written $\boldsymbol{x} \cdot \boldsymbol{x} = 1$. In terms of $\boldsymbol{x}' = \mathbf{M}\boldsymbol{x}$, this condition becomes the equation for an ellipse: $\boldsymbol{x}' \cdot \mathbf{K}\boldsymbol{x}' = 1$, with

$$\mathbf{K} = (\mathbf{M}^{-1})^{\mathrm{T}}\mathbf{M}^{-1} = (\mathbf{M}\mathbf{M}^{\mathrm{T}})^{-1} \, , \tag{7.9}$$

where $\mathbf{K}$ is a real, symmetric, positive definite matrix. For a symmetric matrix we can write $\mathbf{O}^T\mathbf{K}\mathbf{O} = \mathbf{D}$, where $\mathbf{O}$ is an orthogonal matrix and $\mathbf{D}$ is a diagonal matrix. The orthogonal matrix $\mathbf{O}$ determines a rotation of the coordinate system $\boldsymbol{y} = \mathbf{O}^T\boldsymbol{x}$ in which the equation of the ellipse reads $\lambda_1 y_1^2 + \lambda_2 y_2^2 = 1$, where λ_1 and λ_2 are eigenvalues of $\mathbf{K}$. The aspect ratio ν_e is therefore the square root of the ratio of the

eigenvalues of $\mathbf{K}$, such that $\nu_e \geq 1$, while θ_0 is the direction of the eigenvector of $\mathbf{K}$ corresponding to the smallest eigenvalue.

In a generic flow with a positive largest Lyapunov exponent the pseudomonodromy matrix $\mathbf{M}$ will become hyperbolic almost everywhere, having a unique largest eigenvalue, which increases with time. The particles will then align very close to the direction of the dominant eigenvector, irrespective of their initial orientation. However, if the pseudomonodromy matrix remains elliptic, there is no dominant eigenvector and the final direction remains dependent upon the initial orientation. In the hyperbolic case, where there is a perfect alignment, the length of the order parameter vector approaches unity, but in the elliptic case it is shorter than unit length.

7.3 Singularities of the order parameter

In Fig. 7.2 we show the results of the numerical simulations for the order parameter field obtained from Eqs. (7.8) and (7.9) for small axisymmetric particles (with a very large aspect ratio) moving in a random flow field (we used the same model of the flow as in the previous chapter), starting from an isotropic distribution of angles. The zeros of the order parameter are clearly visible and the patterns in the vicinity of these zeroes resemble the core (Fig. 7.2**a**) and delta (Fig. 7.2**b**) singularities.

If zeros of the vector order parameter field exist, the Poincaré index of a curve may be non-zero even though the order parameter depends smoothly upon the position (as can be seen in Fig. 7.2). A singularity where the order parameter is equal to zero occurs where the ellipse, upon which the vector $\boldsymbol{d}(t) = \mathbf{M}(t, t_0)\mathbf{n}_0$ lies, degenerates to a circle. Thus, zeros of the order parameter occur when $\mathbf{M}$ is a rotation matrix.

First, we consider whether such singularities are generic. Because the two-dimensional flow is area-preserving, the 2×2 matrix $\mathbf{M}$ satisfies $\det(\mathbf{M}) = 1$. This matrix can be written in a form determined by three parameters λ, κ, χ:

$$\mathbf{M} = \mathbf{D}(\lambda, \lambda^{-1})\, \mathbf{S}(\kappa)\, \mathbf{O}(\chi) \tag{7.10}$$

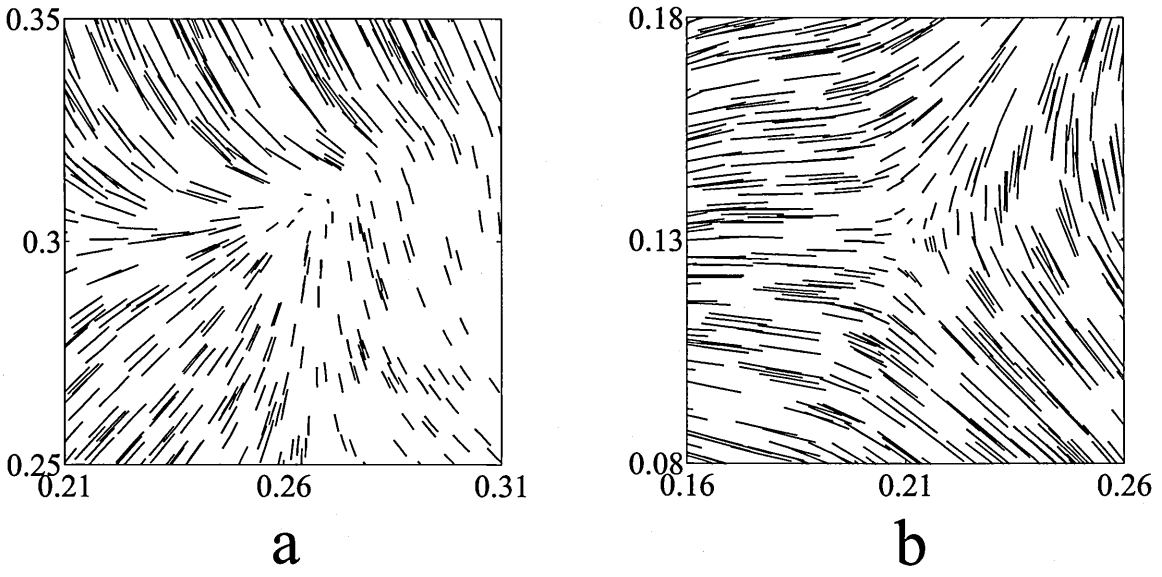

Figure 7.2: Shows the order parameter field for axisymmetric particles in a random flow computed using Eqs. (7.8) and (7.9). Panel **a** shows a core singularity and panel **b** shows a delta singularity. The model and parameters of the flow are the same as in the previous chapter.

where $\mathbf{D}$, $\mathbf{S}$ and $\mathbf{O}$ are respectively diagonal, shear and rotation matrices:

$$\mathbf{D}(\lambda_1, \lambda_2) = \begin{pmatrix} \lambda_1 & 0 \\ 0 & \lambda_2 \end{pmatrix}, \quad \mathbf{S}(\kappa) = \begin{pmatrix} 1 & \kappa \\ 0 & 1 \end{pmatrix},$$
$$\mathbf{O}(\chi) = \begin{pmatrix} \cos\chi & \sin\chi \\ -\sin\chi & \cos\chi \end{pmatrix}. \tag{7.11}$$

The matrix $\mathbf{K}$ in Eq. (7.9), therefore, has a simple dependence upon the parameters λ, κ:

$$\mathbf{K}^{-1} = \mathbf{M}\mathbf{M}^{\mathrm{T}} = \begin{pmatrix} \lambda^2(1+\kappa^2) & \kappa \\ \kappa & \lambda^{-2} \end{pmatrix}. \tag{7.12}$$

The singularity occurs when $\lambda = 1$ and $\kappa = 0$ (with no condition upon χ), which is realized upon varying two parameters. Since the coordinate space is two-dimensional, the singularities have co-dimension zero, implying that they occur at isolated points in a plane.

We now consider the form of the order parameter field in its vicinity. To the leading order, generically the parameters λ and κ depend linearly on the position

in the vicinity of a singular point at which the monodromy matrix becomes a pure rotation. Let us assume that there is a singular point at $\boldsymbol{r}_0 = (x_0, y_0)$. In the vicinity of this point there exists a coordinate system $\boldsymbol{R} = (X, Y)$ such that the monodromy matrix is in the normal form

$$\mathbf{M}(\boldsymbol{R}) = \mathbf{D}(1 + \tfrac{1}{2}X, 1 - \tfrac{1}{2}X)\,\mathbf{S}(\pm Y)\,\mathbf{O}(\chi) + O(\boldsymbol{R}^2)\ . \tag{7.13}$$

The local coordinate system is related to $\boldsymbol{r}$ by a linear transformation: $\boldsymbol{r} - \boldsymbol{r}_0 = \mathbf{T}\boldsymbol{R}$, where $\mathbf{T}$ is a 2×2 matrix and the sign in Eq. (7.13) is chosen so that $\mathbf{T}$ is a non-inverting transformation, i.e. $\det(\mathbf{T}) > 0$.

It is instructive to analyze the behaviour of the order parameter in the vicinity of the singularities. Retaining only the leading order terms in X and Y from Eq. (7.13), we find

$$\mathbf{M}\,\mathbf{M}^{\mathrm{T}} = \begin{pmatrix} 1 + X & \pm Y \\ \pm Y & 1 - X \end{pmatrix} + O(R^2) \tag{7.14}$$

where $R = \sqrt{X^2 + Y^2}$. The eigenvalues of $\mathbf{M}\mathbf{M}^{\mathrm{T}}$ are $\lambda_\pm = 1 \pm R + O(R^2)$, so that $\nu_e = \sqrt{\lambda_+/\lambda_-} = 1 + R + O(R^2)$. Writing $(X, Y) = (R\cos\Theta, R\sin\Theta)$ and $(\cos\Theta', \sin\Theta')^{\mathrm{T}}$ for the eigenvector of $\mathbf{M}\mathbf{M}^{\mathrm{T}}$ corresponding to λ_+, we find $\Theta' = \pm\frac{1}{2}\Theta$, so that

$$\boldsymbol{\zeta}(R, \Theta) = \frac{R}{2}\,\mathbf{n}(\pm\tfrac{1}{2}\Theta) + O(R^2)\ . \tag{7.15}$$

If the positive sign is chosen, $\boldsymbol{\zeta}$ points in the radial direction ($\Theta' = \Theta \bmod \pi$) for only one ray ($\Theta = 0$). For the negative sign, $\boldsymbol{\zeta}$ points radially outwards along three rays ($\Theta = 0, \pm 2\pi/3$). These properties are characteristic of the core and delta singularities, respectively. The order parameter for the normal form is plotted in Fig. 7.3 for both choices of the sign in Eq. (7.14).

We conclude by noting that similarly to the case considered in the previous chapter additional structures are observed when the flow is three-dimensional. In this case, in addition to the 'fingerprint' singularities with a half-integer Poincaré index, singularities with integer Poincaré index are observed as well.

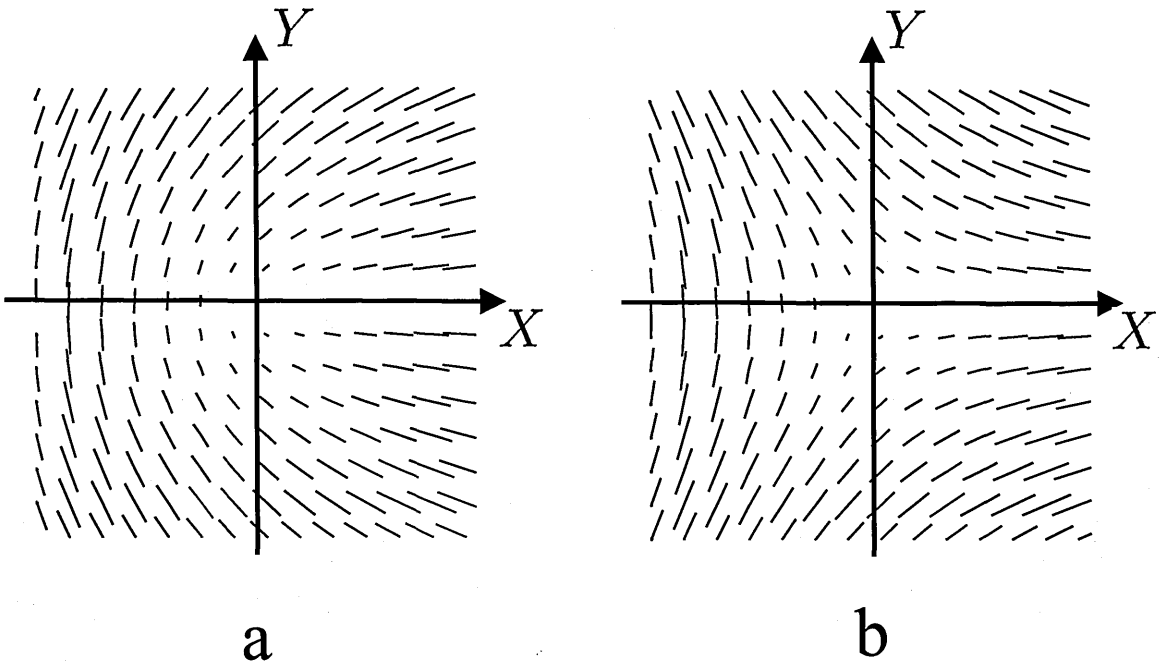

Figure 7.3: (a) Shows the order parameter field $\boldsymbol{\zeta}(\boldsymbol{R})$ for the canonical singularity computed using Eq. (7.14), with a positive sign of Y. This is a core singularity. (b) Shows the order parameter field when the negative sign is chosen. This is a delta singularity.

7.4 Relating the order parameter to light reflection

The order parameter can be investigated experimentally by examining the reflection of light by a rheoscopic fluid. Because we are primarily interested in two-dimensional flows, we consider how the light scattering may be related to the order parameter in the case where the illumination is confined to a surface. This is relevant when the rheoscopic fluid is a thin layer floating on a denser, immiscible fluid, or when the rheoscopic agent is used without dilution, so that the optical depth is very small (implying that scattered light comes from a thin layer close to the surface). The image contrast is greatest when the illumination comes from a direction in the same plane as the surface, and we choose to specify its direction by means of the angle ϕ of the direction perpendicular to that from which the beam is incident.

The intensity of light reflected by the microscopic crystals depends upon their orientation relative to the direction of the source of the light. The angular dependence

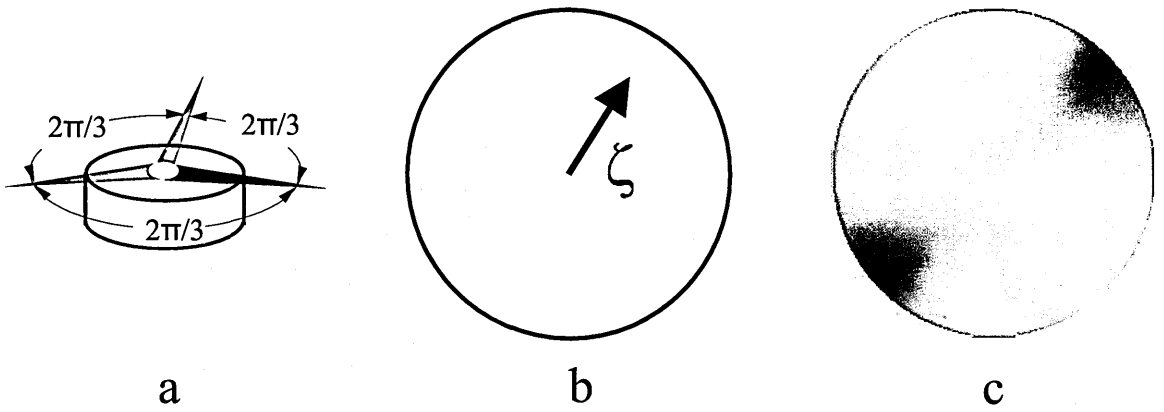

Figure 7.4: (**a**) The direction and degree of ordering of the axes of the crystals in a rheoscopic fluid can be revealed by scattering light from red, green and blue sources arranged around the sample. (**b**) The degree of order of the particles is described by an order parameter vector $\boldsymbol{\zeta}$ lying within a unit circle, which points in the predominant direction of the alignment, with magnitude $0 \leq |\boldsymbol{\zeta}| \leq 1$ indicating the degree of the alignment. (**c**) The colour of the reflected light is a function of the order parameter given by Eq. (7.16). Because the orientation of the vector $\boldsymbol{\zeta}$ is irrelevant, this colour map is symmetric under reflection.

of the reflection depends upon a variety of factors, of which the ratio of the size of the crystals to the wavelength of light and their surface roughness are important. If the crystals are aligned with their long axis at angle θ, the intensity of the reflected light will be $f(\phi - \theta)$, for some function f which is even and periodic with period π and which reaches maximum for $\phi - \theta = \pi n$, where n is an integer. In the following we consider the limit where the crystals are smaller than the wavelength of light, in which case the amplitude of the scattered radiation is proportional to the projected area of the crystal in the direction of the incident light. This implies that a particle at angle θ scatters light from a source which is perpendicular to the direction ϕ with an intensity proportional to $\cos^2(\theta - \phi)$. For larger crystals the function $\cos^2(\theta - \phi)$ is replaced by another function $f(\theta - \phi)$. This would make a quantitative but not a qualitative difference to the colour images which are displayed here.

More detailed information about the orientation of the particles may be revealed by using three different light sources with different colours, illuminating the fluid from three different directions. At any given position the fluid reflects light with a colour C determined by an additive mixing of the scattered light from red (R), green (G) and blue (B) sources, arranged about the sample at directions separated by $2\pi/3$,

so that ϕ takes value 0, $2\pi/3$ and $4\pi/3$ for R, G and B components, respectively, as illustrated in Fig. 7.4**a**. This results in the light being reflected with a colour C determined by

$$C = I(0)\,R + I(2\pi/3)\,G + I(4\pi/3)\,B, \tag{7.16}$$

where $I(\theta)$ is the 'inertia' of the axial distribution relative to the direction θ:

$$I(\theta) = \int_0^{2\pi} d\theta'\; P(\theta')\cos^2(\theta - \theta')\;. \tag{7.17}$$

Eq. (7.16) is very similar to Eq. (6.1) which we have used in the previous chapter for illustrating the textures using a colour-coding. The difference is that here, in order to compute the intensity of the reflected light, we average over random initial particle orientations, whereas in the previous chapter we have used an actual particle direction for that purpose. Using the probability density (7.5) we obtain in terms of the parameters ν_e and θ_0:

$$\begin{aligned} C \;=\; & \frac{1}{4(\nu_e+1)}\{4R[\nu_e\cos^2\theta_0 + \sin^2\theta_0] \\ & +\; G[2(1-\nu_e)\cos^2\theta_0 - 2\sqrt{3}(\nu_e-1)\sin\theta_0\cos\theta_0 + 3\nu_e+1] \\ & +\; B[2(1-\nu_e)\cos^2\theta_0 + 2\sqrt{3}(\nu_e-1)\sin\theta_0\cos\theta_0 + 3\nu_e+1]\}\;. \end{aligned} \tag{7.18}$$

The colour map produced by Eq. (7.18) is shown in Fig. 7.4**c**. In Fig. 7.5 we use this colour map to illustrate reflection produced by three coloured light sources corresponding to the order parameter field shown in Fig. 7.2. In principle just two of the functions $I(0)$, $I(2\pi/3)$ and $I(4\pi/3)$ are sufficient to determine the two parameters of the order parameter vector. However, using three colours has two advantages: with three colours the ratios of the scattered intensities can be used, so that the normalization of the intensities is not relevant. Using three colours the Poincaré index of singularities can be detected, as explained in the previous chapter. The index of a given curve is determined by the number of complete cycles of the primary colours, as the curve is traversed in a clockwise direction. A sequence $R \to G \to B$ adds 1/2 to the index, whereas a sequence $R \to B \to G$ subtract 1/2 from the net index.

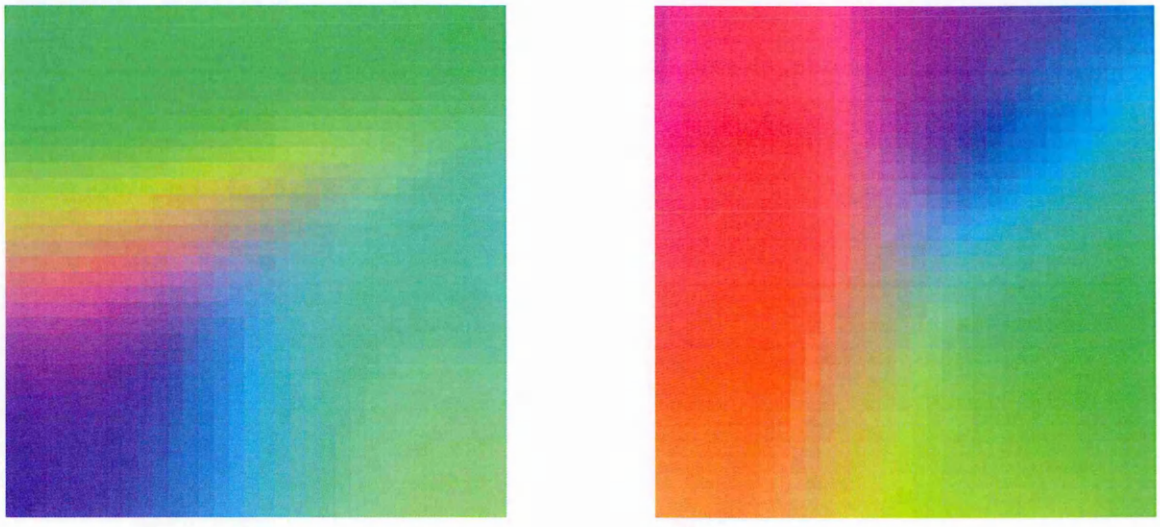

a b

Figure 7.5: Light reflection from three light sources calculated using Eq. (7.18) corresponding to the vector fields in Fig. 7.3.

7.5 The experiment

It is an interesting and challenging problem to understand what aspects of the flow are revealed by the patterns seen in a rheoscopic fluid. In particular, we are interested in a relation between these patterns and the theory presented in this and previous chapters. The purpose of the experiment reported here is to illustrate the topology of the textures using coloured light sources.

The setup of the experiment is shown in Fig. 7.6. The rheoscopic fluid was contained in a 'beaker' (a small lid) of radius 3.2cm with non-reflecting walls and bottom. The fluid we used was commercially available rheoscopic fluid (see, e.g. [74]). The actual properties of the fluid (such as density of the particles, dimensions of the particles, optical properties, etc.) remained unknown. We have discussed the possibility of generating 2d random flows by floating a thin layer of the rheoscopic fluid on a surface of the denser fluid which is stirred by e.g. a magnetic stirrer. We were unable to reproduce such a setup, mainly because of difficulties in dealing with dense fluids, which are sometimes poisonous and very volatile. Instead, we simply poured a thin layer (3-5mm) of the undiluted rheoscopic fluid in the beaker and stirred it manually.

The light sources were arranged around the beaker on fixed stands at the height

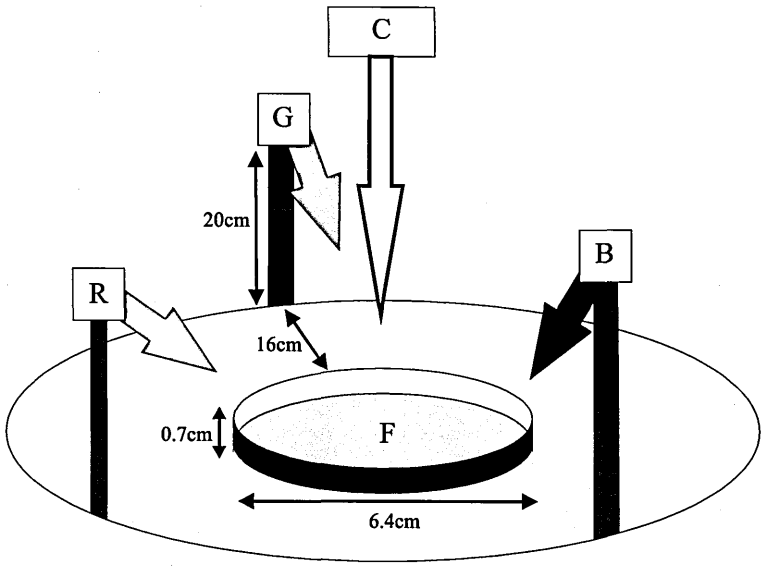

Figure 7.6: Shows the setup of the experiment. A beaker containing a thin layer (width varies from 3 to 5mm) of the rheoscopic fluid (F) is illuminated by three light source (R,G,B) arranged at angles 0, $2\pi/3$ and $4\pi/3$ around the sample. The surface of the fluid is observed by the camera (C) from above.

around 20cm. The light in this case came from top and from sides to the surface of the fluid. The light for each source was produced by several light-emitting diodes (LED) of red, green and blue colours bound together. In particular, red light was produced by five red LEDs (forward voltage (fv) - 2.5V, luminous intensity (li) - 0.8-1.0cd), green light was produced by four green LEDs (fv - 3.5V, li - 5.0cd), and blue light was produced by four blue LEDs (fv - 3.2V, li - 0.88-2.5cd). Although the luminous intensity of a single green LEDs was appreciably larger, we found no significant difference between blue and green sources when four LEDs were combined. We used an additional red LED to compensate the difference in luminosity, since it was the weakest light source. Each combined light source was passed through an individual piece of scratched glass, so that the light from several LEDs of the same colour produced a single diffused source of coloured light. The stands were then slightly adjusted, so that the mixing produced approximately uniform white colour on the surface of the fluid.

The motion of the fluid in the beaker was captured by the camera from above. We used Sony HDR-SR10 camcorder to capture the motion in high definition and then extracted snapshots for the analysis. We found that it is technologically simpler

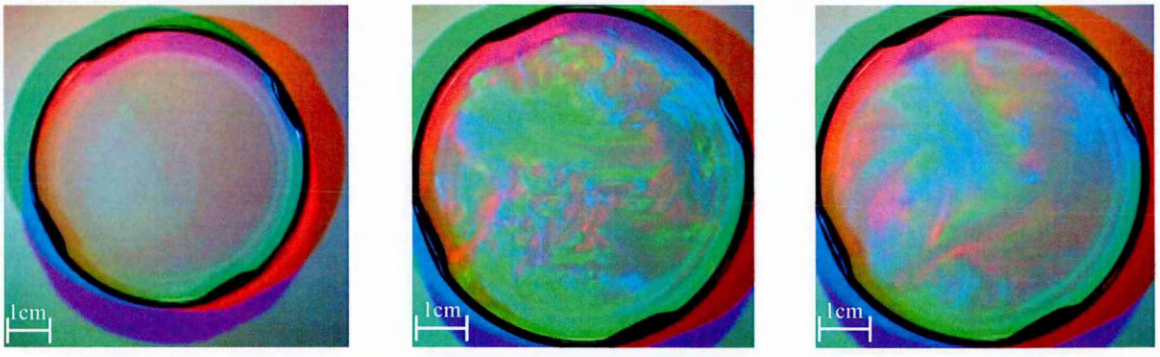

Figure 7.7: Shows three typical snapshots of the surface of the rheoscopic fluid in the experiment: (**a**) fluid is stationary, (**b**) fluid is stirred, (**c**) fluid is left to evolve.

and the results are better compared to making individual shots. The experiment was performed in a dark room to exclude the influence of an ambient light. In such poor light conditions amateur cameras tend to produce unnatural colours, if the white balance is set automatically. To prevent this, at the beginning of the experiment, the white balance of the camera was set manually by putting a piece of white paper on top of the beaker. This enabled the camera to adjust its settings to produce realistic colours.

In Fig. 7.7 we show a set of typical snapshots observed in the experiment. The first snapshot (Fig. 7.7**a**) illustrates the initial configuration, when the fluid is left to stand for some time. The surface in this case looks uniform and whitish. The colour-mixing can be noticed just outside the beaker. The walls of the beaker shade each colour in turn, producing a circular pattern with prime colours separated by intermediate colours (orange, purple and cyan).

The second snapshot (Fig. 7.7**b**) illustrates the fluid just after it was stirred. It shows chaotic colourful patterns, indicating that the particles already start to align. After the fluid is stirred it is left to evolve by itself for some time until the motion is damped out. This time depends on the thickness of the layer and the radius of the beaker. At this stage, the patterns become dim, but the colours are still visible (as illustrated in Fig. 7.7**c**). If we wait even longer, the particles again become randomly oriented, and the fluid returns to its initial state illustrated by Fig. 7.7**a**.

Our main experimental results are presented in Fig. 7.8. We indicate two points

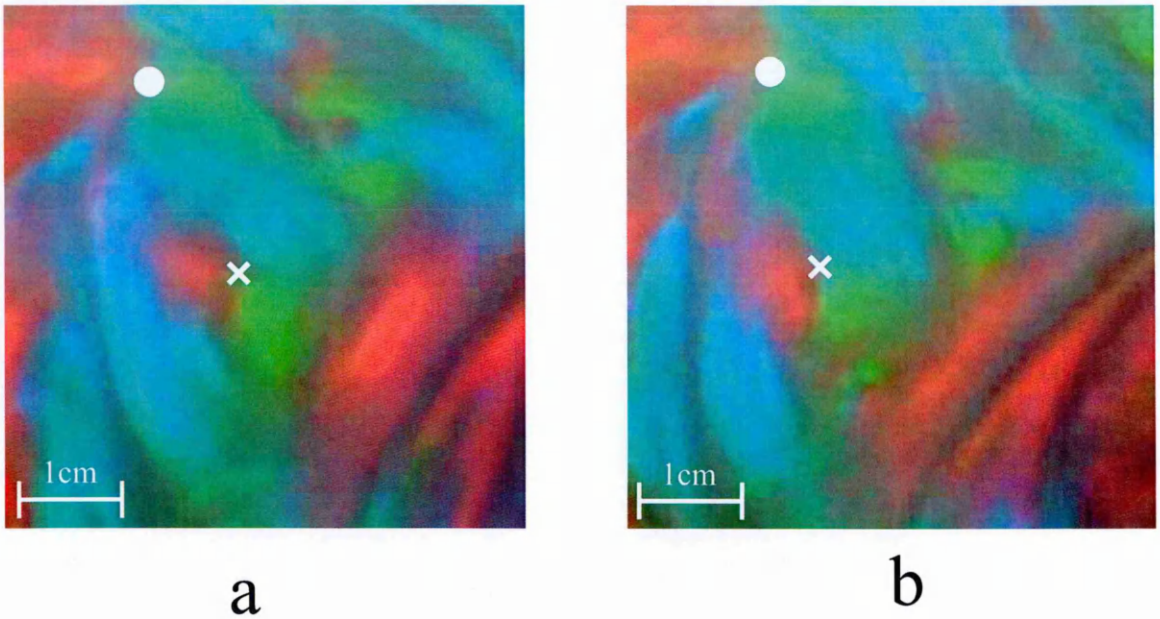

Figure 7.8: Shows the outcome of the experiment: two snapshots (**b** is later than **a**) illustrating patterns on the surface of the rheoscopic fluid which exhibit topological singularities. In each snapshot a cross indicates a delta singularity, and a circle indicates a core singularity.

with the property that, on traversing a small clockwise circuit around these points, we encounter the primary colours without repetition ($R \to G \to B$ for the circle and $R \to B \to G$ for the cross). Such a property is characteristic to the singularities with a half-integer Poincaré index. This is a persuasive evidence that in our simple experiment we were able to visualize the topology of the textures, which exhibit singularities with a half-integer Poincaré index, as predicted by the theory.

7.6 Summary

In this chapter we have discussed the order parameter, characterizing the alignment of small axisymmetric particles and its relation to the reflection of light by a rheoscopic fluid. We have chosen the order parameter to be a non-oriented vector which points in the predominant direction of the alignment, with the length which determines the degree of the alignment. We have obtained the probability density function which determines how an initially isotropic distribution of the particles evolves in time. Using this function, we have obtained the order parameter in terms of the pseudomonodromy

matrix of the flow. The order parameter field exhibits singularities located at points where the length of the vector is zero. We have found that these zeros have normal forms which are analogous to the core and delta singularities of fingerprints discussed in chapter 6. We have shown how the order parameter can be related to the reflection of the light by a rheoscopic fluid. If the fluid is illuminated by three light sources (red, green, and blue), the Poincaré index is determined by following the change of the primary colours on traversing a closed curve. We have performed a simple experiment with the results that strongly support our theoretical findings.

Chapter 8

Conclusions

We conclude the thesis by summarizing our main results and proposing a number of possible questions and extensions for further research.

8.1 Part I: motion of spherical particles

In part I of the thesis we studied a number of problems involving spherical particles suspended in complex flows. We discussed diffusion of a particle driven by a random force which depends upon the position of the particle, as well as time. We also discussed quantitatively the collision rate of inertial spherical particles.

The diffusion of particles was analyzed using the Fokker-Planck equation describing a time evolution of the probability density of the particle position or momentum. It is applicable when the dynamics of a stochastic variable consists of small independent disturbances.

Our theory for the collision rate explains a sharp increase of the collision rate, as the dimensionless parameter measuring the intensity of turbulence exceeds a threshold. This phenomenon was previously observed in numerical experiments and attributed to spatial clustering of the particles. We argued that the clustering mechanism is not dominant, and that the prevailing factor of the increase is the formation of fold caustics in the velocity field of the particles.

8.1.1 Summary of the results

Our main original results in part I are as follows:

- two generalized models for diffusion of a particle, the generalized Ornstein-Uhlenbeck process and the Chandrasekhar-Rosenbluth model with a short-range interaction potential, have the same scaling of the diffusion coefficients, leading to the same short-time asymptotic dynamics. This is surprising because two models are described by different microscopic processes;

- the short-time asymptotic dynamics in both models is characterized by anomalous diffusion of the momentum with the universal exponent $2/5$ and ballistic diffusion of the displacement; the probability distribution of the velocity in the generalized Ornstein-Uhlenbeck process at large time is non-Maxwellian;

- the particles in the generalized Kramers model can exhibit ratchet behaviour when the external potential is periodic and asymmetric and the external forcing is sufficiently strong;

- the collision rate of inertial spherical particles exhibits an 'activated' behaviour containing a factor $\exp(-S/\mathcal{I})$, where $\mathcal{I}$ is the intensity of turbulence and S is a constant. The activated behaviour is due to fold caustics where the velocity field of the particles becomes multivalued; our theory does not involve spatial clustering and predicts a rapid (of order a few minutes) onset of rainfall from unstable cumulus clouds.

8.1.2 Scope for further research

Our generalizations of the classical diffusion processes involved a random force which depends upon the position of a particle, as well as time. Although the models are interesting in their own right, we have not yet found a physical model of motion of particles in fluids where the generalized Ornstein-Uhlenbeck model is applicable. In most of the fluid-mechanical applications particles cannot accelerate to such velocities that they travel over many correlation lengths in one correlation time. However,

models of particles accelerated by random electro-magnetic forces can provide a scope for further research. In particular, the model for cosmic ray acceleration proposed by Fermi [19] may be a good candidate for a physical realization of the generalized Ornstein-Uhlenbeck process, which requires further investigation.

The generalized Kramers model exhibits a number of interesting features, and it is necessary to find physical processes where the random noise has spatial correlations. The most probable candidates are random fluctuations generated by ultrasonic waves and particle moving on the surface of a solid body. It is also necessary to discuss the validity of the corresponding Fokker-Planck equation in the regime which gives rise to the result corresponding to the increase of the potential in the weak forcing limit. This result differs from the one obtained in [25] (discussed in section 4.4) and needs to be understood thoroughly.

Our theory for the collision rate provides a remarkable agreement with the numerical simulations despite its heuristic nature. In the simulations we used single-scale flows and argued that multi-scale properties of turbulence may not be relevant. Our theory involves only monodisperse system of particles, whereas in clouds the droplets can have a variety of sizes. As the particles collide and aggregate, their size distribution may change. In future, it is required to extend our theory to more realistic models, incorporating different aspects of motion of water droplets in clouds.

8.2 Part II: motion of non-spherical particles

In part II we discussed textures of small axisymmetric particles advected in complex flows. Our discussion in chapters 7 and 8 was mainly based on a powerful solution of the equation of motion, first mentioned by Szeri [29]. This solution is topologically trivial, if the initial orientation field is smooth, indicating that the patterns from the numerical simulations require careful consideration, as they exhibit apparent topological singularities. We presented arguments showing that the singularities in the textures were asymptotic. The same solution was used to describe evolution of a statistically isotropic distribution of the particle orientation. We introduced an order

parameter vector characterizing the alignment of the particles, which was shown to exhibit true topological singularities. We showed how the order-parameter may be related to the reflection of light by a rheoscopic fluid and discussed a corresponding experiment.

8.2.1 Summary of the results

Our main original results in part II are as follows:

- textures of small axisymmetric particles in a complex flow, obtained from the numerical simulations, exhibit apparent topological singularities with a half-integer Poincaré index;

- based on the solution of the equation of motion, the singularities cannot exist in a strict mathematical sense. It is argued that they are approached in an asymptotic sense. First, the scar lines emerge where the particles change direction rapidly. Later, these scar lines narrow to the extent that they do not contain actual positions of the particles. In this case, the scar lines effectively disappear, but their ends remain as point singularities;

- if the initial orientation field of the particles is random, it is appropriate to describe the textures using the probability density function of the orientation. The alignment of the particle is characterized using the order parameter, a vector pointing in the direction of the predominant orientation of the particles, with length representing the degree of the alignment; the order-parameter field exhibits true topological singularities with a half-integer Poincaré index, located at points in space where the length of the order parameter is zero;

- the order parameter is related to the reflection of light by a rheoscopic fluid illuminated by coloured light sources; the results of the experiment on a rheoscopic fluid show strong evidences confirming our theory.

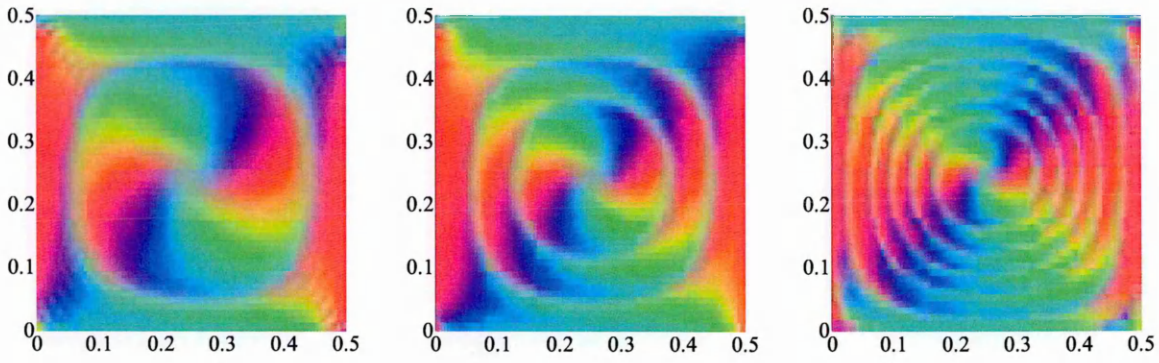

Figure 8.1: Illustrates a spiral pattern obtained from the numerical simulation [using Eq. (7.18)] which may be generated by motion of a rheoscopic fluid illuminated by three coloured light sources in a two-dimensional cellular flow, with stream function $\psi(x, y) = \sin(x)\sin(y)/2\pi$. The arms of the spiral tighten as time increases. The times are (successively from left to right) $t = 5$, $t = 9$, and $t = 18$.

8.2.2 Scope for further research

In the thesis we only discussed the case of axisymmetric particles, and little is known about motion of triaxial bodies, where the solution of the corresponding equation of motion is not available. It is not clear whether this case significantly differs from the case of axisymmetric particles discussed in the thesis, but for completeness advection of triaxial bodies should also be investigated.

We only discussed the case when the flow is complex, so that its largest Lyapunov exponent is positive, and the norm of the pseudomonodromy matrix grows exponentially with time. There are cases when the pseudomonodromy matrix does not have large eigenvalues, and the particle directions may depend increasingly sensitively on the position in the long-time limit. We can extend our theory for the case of recirculating steady flows, where there is no guarantee that the pseudomonodromy matrix has an eigenvalue which increases with time. In a recirculating two-dimensional flow the particles follow contours of the stream function of the flow. If these contours are closed curves, then the trajectories of the particles are periodic. It was first shown by Szeri [29] that in steady recirculating flows there are stream lines (which we term 'hyperbolic bands') where the particle approaches a definite direction, and stream lines (termed 'elliptic bands') where the particle continues tumbling and does not approach a definite directions. We have shown that the behaviour of a particle depends

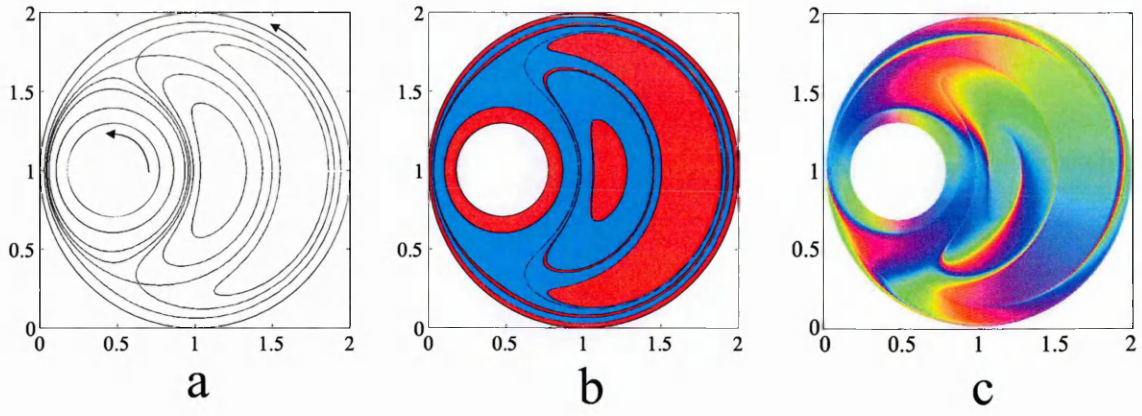

Figure 8.2: (**a**) Shows contours of the stream function for a journal bearing flow. In this example both cylinders rotate in the same direction, with the angular velocity of the inner cylinder exceeding that of the outer cylinder by a factor of 20. (**b**) These contours can be coloured according to whether a particle approaches definite direction (blue), or whether it continues tumbling (red). (**c**) Illustrates the reflection of red, green and blue light from rheoscopic fluid in a journal bearing flow in the long-time limit obtained from the numerical simulation.

on whether the pseudomonodromy matrix calculated for one period of motion has two real eigenvalues (hyperbolic case) or two complex eigenvalues (elliptic case).

If we are concerned with the reflection of light by a rheoscopic fluid in a steady recirculating motion, the order parameter in the elliptic bands may vary on such a small length scale, that in the experiment the patterns could fluctuate on a scale below the resolving power of the eye. This can be illustrated by the numerical experiment for a simple stirring motion, which produces an increasing tightly wound spiral pattern (see Fig. 8.1). In order to fully understand the evolution of the textures, it is required to calculate local average of the order parameter in the long-time limit. Preliminary calculations show that the singularities of the average order parameter are located in the elliptic bands and have the same structure as in the case discussed in chapter 7. We illustrate our current findings in Fig. 8.2 in application to the motion of rod-like particles in a 'journal bearing' flow, i.e. a steady two-dimensional flow between two non-slip, non-concentric rotating cylinders. The stream lines of the flow are shown in Fig. 8.2**a**. They can be labelled according to the form of the one-period pseudomonodromy matrix (hyperbolic or elliptic). In the hyperbolic bands, the theory discussed in chapter 7 is applicable, and the light reflection is calculated using Eq. (7.18). In the elliptic bands, the local average of the order parameter is used. In a journal bearing

flow we expect to see patterns shown in Fig. 8.2**c**.

The experimental results may be improved in several ways. Instead of manually stirring the fluid, a two-dimensional flow may be realized by floating a thin a layer of a rheoscopic fluid on top of a denser fluid which is stirred. In view of the developing theory for the order parameter in steady flows, the corresponding experiment may also be performed. It would be particularly interesting to observe spiral patterns in a cellular flow of a stirred fluid. If the results of such experiment are consistent with our suggestions, then the flow between two rotating eccentric cylinders should also be investigated experimentally.

Personal bibliography

- V. Bezuglyy, B. Mehlig, M. Wilkinson, K. Nakamura, and E. Arvedson, "Generalized Ornstein-Uhlenbeck processes", *J. Math. Phys.*, **47**, 073301, (2006).
- V. Bezuglyy, B. Mehlig, and M. Wilkinson, "Universal anomalous diffusion of weakly damped particles", preprint, (2009).
- V. Bezuglyy, "Generalized Kramers model", preprint, (2009).
- M. Wilkinson, B. Mehlig, and V. Bezuglyy, "Caustic activation of rain showers", *Phys. Rev. Lett.*, **97**, 048501, (2006).
- M. Wilkinson, V. Bezuglyy, and B. Mehlig, "Fingerprints of random flows?" *Phys. Fluid.*, **21**, 043304, (2009).
- V. Bezuglyy, B. Mehlig, and M. Wilkinson, "Poincaré indices of rheoscopic visualisations", arxiv:0903.3615, (2009)
- M. Wilkinson, V. Bezuglyy, and B. Mehlig, "Emergent order in rheoscopic swirls", preprint, (2009).

Bibliography

[1] R. A. Shaw, *Annu. Rev. Fluid Mech.*, **35**, 183-227, (2003).

[2] K. Mann and J. Lazier, *Dynamics of marine ecosystems. Biological-physical interactions in the oceans*, Blackwell Scientific Publications, Boston, (1991).

[3] V. W. Beckwith, T. Henning, and Y. Nakagawa, *Dust properties and assembly of large particles in protoplanetary disks*, in Protostars and Planets IV, edited by V. Manning, A. P. Boss, and S. S. Russell, University of Arizona Press, Tucson, (2000).

[4] C. Oppenheimer, *Geophys. Res. Lett.*, **23**, 2057, (1996).

[5] N. I. Shakura and R. A. Sunyaev, *Astronomy and Astrophysics*, **24**, 337, (1973).

[6] J. M. Deutsch, *J. Phys. A*, **18**, 1449, (1985).

[7] M. R. Maxey, *J. Fluid Mech.*, **174**, 441, (1987).

[8] J. Sommerer and E. Ott, *Science*, **359**, 334, (1993).

[9] M. Wilkinson, B. Mehlig, S. Östlund, and K. P. Duncan, *Phys. Fluids*, **19**, 113303, (2007).

[10] J. Bec, L. Biferale, G. Boffetta, M. Cencini, S. Musachchio, and F. Toschi, *Phys. Fluids*, **18**, 091702 (2006).

[11] M. Wilkinson and B. Mehlig, *Europhys. Lett.*, **71**, 186, (2005).

[12] G. Falkovich, A. Fouxon, and G. Stepanov, *Nature* (London), **419**, 151, (2002).

[13] M. V. Berry, *Singularities in Waves*, Les Houches Lecture Series Session XXXV, eds. R. Balian, M. Kléman and J-P. Poirier, North Holland: Amsterdam, 453-543, (1981).

[14] L. F. Richardson, *Weather prediction by numerical process*, Cambridge University Press, (1922).

[15] A. N. Kolmogorov, *Proceedings of the USSR Academy of Sciences*, **30**, 299, (1941), A. N. Kolmogorov, *Proceedings of the USSR Academy of Sciences*, **32**, 16, (1941).

[16] E. Arvedson, B. Mehlig, M. Wilkinson, and K. Nakamura, *Phys. Rev. Lett.*, **96**, 030601, (2005).

[17] V. Bezuglyy, B. Mehlig, M. Wilkinson, K. Nakamura, and E. Arvedson, *J. Math. Phys.*, **47**, 073301, (2006).

[18] G. E. Ornstein and L. S. Uhlenbeck, *Phys. Rev.*, **36**, 823, (1930).

[19] E. Fermi, *Phys. Rev.*, **75**, 1169, (1949).

[20] P. A. Sturrock, *Phys. Rev.*, **141**, 186, (1966).

[21] S. Chandrasekhar, *Astrophys. J.*, **97**, 255, (1992).

[22] M. N. Rosenbluth, W. M. MacDonald, and D. L. Judd, *Phys. Rev.* **107**, 1 (1957).

[23] H. A. Kramers, *Physica* (Utrecht), **7**, 284 (1940).

[24] R. P. Feynman, R. B. Leighton, and M. Sands, *The Feynman Lectures on Physics*, vol. 1, Addison-Wesley, Reading, MA, (1966).

[25] T. Monnai, A. Sugita, and K. Nakamura, *Europhys. Lett.*, **84**, 20005, (2008).

[26] S. Sundaram and L. R. Collins, *J. Fluid Mech.*, **335**, 75-109, (1997).

[27] Y. Zhou, A. S. Wexler, and L.-P. Wang, *Phys. Fluids*, **10**, 1206-16, (1998).

[28] E. R. Henry, *Classification and Uses of Finger Prints*, Routledge, London, (1900).

[29] A. J. Szeri, *Phil. Trans. R. Soc. Lond.*, **A345**, 477-508, (1993).

[30] A. J. Szeri and L. G. Leal, *Chaos, Solitons & Fractals*, **4**, 913-27, (1994).

[31] H. Shin and M. R. Maxey, *Phys. Fluids*, **A3**, 1434, (1991).

[32] R. Mallier and M. R. Maxey, *Phys. Fluids*, **A3**, 1481, (1991).

[33] A. J. Szeri, S. Wiggins, and L. G. Leal, *J. Fluid Mech.*, **228**, 207, (1991).

[34] H. Shin and M. R. Maxey, *Phys. Rev. E*, **56**, 5431, (1997).

[35] G. K. Batchelor, *An Introduction to Fluid Dynamics*, Cambridge University Press, Cambridge, (1999).

[36] S. T. Thoroddson and J. M. Bauer, *Phys. Fluids*, **11**, 1702, (1999).

[37] P. A. Davidson, *Turbulence: an introduction for scientists and engineers*, Oxford University Press, Oxford, (2004).

[38] J. C. Vassilicos, *Intermittency in turbulent flows*, Cambridge University Press, Cambridge, (2000).

[39] Numerical Recipes in C, Second Edition, (1992), http://www.nr.com.

[40] A. Careta, F. Sagués, and J.M. Sancho, *Phys. Rev. E*, **48**, 2279, (1993).

[41] M. Holzer and E.D. Siggia, *Phys. Fluids*, **6**(5), 1820, (1994).

[42] G. G. Stokes, *Trans. Camb. Phil. Soc.*, **9**, 8, (1851).

[43] M. R. Maxey and J. Riley, *Phys. Fluids*, **26**, 883, (1983).

[44] P. S. Epstein, *Phys. Rev.*, **23**, 710, (1924).

[45] G. B. Jeffery, *Proc. R. Soc. London, Ser. A*, **102**, 161, (1922).

[46] F. P. Bretherton, *J. Fluid Mech.*, **14**, 284-304, (1962).

[47] N. G. van Kampen, *Stochastic processes in physics and chemistry*, 2nd ed., North-Holland, Amsterdam, (1981).

[48] R. Brown, *Phil. Mag.*, **4**, 161, (1828).

[49] A. Einstein, *Ann. d. Physik*, **17**, 549, (1905).

[50] L. Golubovic, S. Feng, and F.-A. Zeng, *Phys. Rev. Lett.*, **67**, 2115 (1991).

[51] M. N. Rosenbluth, *Phys. Rev. Lett.*, **69**, 1831, (1992).

[52] M. Abramowitz and I. A. Stegun, *Handbook of Mathematical Functions*, 9th ed. Dover, New York, (1972).

[53] P. Hänggi, P. Talkner, and M. Borkovec, *Rev. Mod. Phys.*, **62**, 251 (1990).

[54] P. Reimann, *Phys. Rep.*, **361**, 57 (2002).

[55] M. O. Magnasco, *Phys. Rev. Lett.*, **71**, 1477 (1993).

[56] H. Risken, *The Fokker-Planck Equation. Methods of Solutions and Applications*, Springer, New York, (1999).

[57] P. G. Saffman and J. S. Turner, *J. Fluid Mech.*, **1**, 16-30, (1956).

[58] J. Abrahamson, *Chem. Eng. Sci.*, **30**, 1371-9, (1975).

[59] M.V. Smoluchowski, *Z. Phys. Chem.*, **XCII**, 129 (1917).

[60] R. Mei and K. C. Hu, *J. Fluid. Mech.*, **391**, 67 (1999).

[61] B. Andersson, K. Gustavsson, B. Mehlig, and M. Wilkinson, *Europhysics Lett.*, **80**, 69001, (2007).

[62] K. Gustavsson, B. Mehlig, and M. Wilkinson, *New J. Phys.*, **10**, 075014, (2008).

[63] B. Mehlig, V. Uski, and M. Wilkinson, *Phys. Fluids.*, **19**, 098107, (2007).

[64] K. Gustavsson, B. Mehlig, M. Wilkinson, and V. Uski, *Phys. Rev. Lett.*, **101**, 174503, (2008).

[65] K. Duncan, B. Mehlig, S. Östlund, and M. Wilkinson, *Phys. Rev. Lett.*, **95**, 240602, (2005).

[66] M. Wilkinson and B. Mehlig, *Phys. Rev. E*, **68**, 040101, (2003).

[67] H. Sigurgeirsson, A.M. Stuart, and J. Wan *J. Comp. Phys.*, **172**, 766, (2001).

[68] P. G. de Gennes and J. Prost, *The Physics of Liquid Crystals*, Oxford: Clarendon Press, (1993).

[69] M. V. Berry and J. H. Hannay, *J. Phys. A*, **10**, 1809, (1977).

[70] P. Matisse and M. Gorman, *Phys. Fluids*, **27**, 759, (1984).

[71] Ö. Savaş, *J. Fluid Mech.*, **152**, 235, (1985).

[72] G. Gauthier, P. Gondoret, and M. Rabaud, *Phys. Fluids*, **10**, 2147-54, (1998).

[73] G. G. Lipscomb, M. M. Denn, D. U. Hur, and D. V. Boger, *J. Non-Newtonian Fluid Mech.*, **26**, 297-325, (1988).

[74] http://www.teachersource.com.